



TECHNISCHE
UNIVERSITÄT
WIEN

VIENNA
UNIVERSITY OF
TECHNOLOGY

DISSERTATION

Micro X-ray Fluorescence Analysis and Micro-Tomography of Human Bone and Tissue

Ausgeführt zum Zwecke der Erlangung des akademischen Grades eines
Doktors der technischen Wissenschaften unter der Leitung von

Ao. Univ. Prof. Dipl.-Ing. Dr. techn. Peter Wobrauschek
141

Atominstitut der Österreichischen Universitäten

Eingereicht and der Technischen Universität Wien
Fakultät für Physik

von

Norbört Zöger
9225639

Josef Bierenzgasse 8/49, 2700 Wiener Neustadt

Wien, am 20. Mai 2005

A handwritten signature in black ink, reading 'Norbört Zöger'. The signature is written in a cursive style with a long horizontal stroke at the end.

"...life is one big question
when you're starin' at the clock"

40 Oz. To Freedom
Bradley J. Novell
(1968-1996)

Abstract

The distribution of various chemical elements in human tissue (bone and brain) has been studied by synchrotron radiation induced micro X-ray fluorescence analysis (SR- μ XRF) in scanning and in tomographic mode. Experiments have been performed at three different synchrotron radiation facilities, HASYLAB, Hamburg, ANKA, Karlsruhe, ESRF, Grenoble where dedicated micro-focus beamlines, offering sufficient photon flux and adequate X-ray optics for the different analytical tasks, were used.

In case of bone the matching of elemental maps from spatially resolved μ -XRF measurements with backscattered electron images, providing information on the bone structure, allows to assign fluorescence intensities to the features of the calcified tissue and therefore the identification of zones of increased accumulation for the different elements. Especially for lead (Pb) –a toxic metal –, which resorbs into circulation when an increased amount of Ca is needed or in times of metabolic changes of the tissue due to bone diseases, the knowledge of the Pb storage sites in bones are of great medical importance.

Starting from conventional μ -XRF measurements on 4mm thick samples the spatial resolution and therefore the accuracy of the method has been steadily enhanced by reduction of the sample thickness to 200 μ m and finally employing μ -XRF in the confocal mode. From comparison of the determined elemental maps with backscattered electron images from the analyzed bone areas (prepared by a group from the Ludwig Boltzmann-Institut of Osteology, Vienna, Austria), it could be shown that the accumulation of Pb in bone is mostly restricted to the so called tidemark which divides noncalcified from calcified tissue and is considered as a metabolically active zone. Furthermore a strong correlation between Zn and Pb was found on this calcification front. Results from confocal μ -XRF on bones with duplicated tidemarks exhibit the eventuality of a time delay in the metabolism of Pb compared to Zn.

When applying combined X-ray absorption and fluorescence tomography, similar results were obtained showing also the restriction of highest Zn and Pb intensities to small zones of the analyzed bone.

Elemental mapping has been performed on various slices from different areas of human brain at ESRF, ID-22. Whereas the assignment of the maps to different structures of the brain is much more difficult than it is for bone tissue, an inhomogeneous distribution of Pb was found in all analyzed samples from frontal cortex, hippocampus and thalamus.

Part of the work presented in this thesis appears in the following publications and annual reports of the facilities where the experiments were performed.

1. N. Zoeger, P. Wobrauschek, C. Strel, G. Pepponi, P. Roschger, G. Falkenberg, W. Osterode
Distribution of Pb and Zn in slices of human bone by SR- μ XRF
X-ray spectrometry, 34,140-143 (2005)
2. N. Zoeger, C. Strel, P. Wobrauschek, C. Jokubonis, G. Pepponi, P. Roschger, S. Bohic, W. Osterode
Elemental mapping in slices of human brain by SR- μ XRF
Adv. In X-ray Anal., accepted
3. N. Zoeger, C. Strel, P. Wobrauschek, C. Jokubonis, G. Pepponi, P. Roschger, S. Bohic, W. Osterode
Elemental mapping in slices of human brain by SR- μ XRF
Powder Diffr. 20, 2 (2005)
4. P. Wobrauschek, C. Strel, G. Pepponi, S. Zamini, N. Zoeger, G. Falkenberg, W. Osterode
Micro-XRF investigation of human bone
Hasylab Annual Report 2001
5. P. Wobrauschek, N. Zoeger, G. Pepponi, C. Strel, G. Falkenberg, W. Osterode
Variations in Pb and Ca concentrations at bone transition zones determined by SR-XRF with a microbeam at BL L
Hasylab Annual Report 2002
6. P. Wobrauschek, N. Zoeger, C. Strel, G. Pepponi, C. Jokubonis, G. Falkenberg, P. Roschger, W. Osterode
Spatially resolved determination of Minor and Trace elements in 200 μ m thin slices of human bone by Micro SR-XRF at BL L
Hasylab Annual Report 2003
7. N. Zoeger, P. Wobrauschek, C. Strel, G. Falkenberg, P. Roschger,
Elemental Mapping of Human Bone by Confocal SR micro-XRF
Hasylab Annual Report 2004
8. N. Zoeger, C. Strel, P. Wobrauschek, D. Wegrzynek, E. Chinea-Cano, R. Simon, S. Staub
Combined fluorescence- absorption tomography on human bones
ANKA Annual Report 2004

The most recent work on confocal fluorescence imaging and on combined fluorescence- and absorption tomography is to be submitted

- N. Zoeger, P. Wobrauschek C. Strel, C. Jokubonis, P. Roschger, J.G. Hofstaetter, G. Pepponi, G. Falkenberg, W. Osterode, A. Berzlanovich, W. Osterode
Lead accumulation in the tidemark of articular cartilage
to be submitted to Nature med.
- N. Zoeger, C. Strel, P. Wobrauschek, D. Wegrzynek, E. Chinea-Cano, R. Simon, S. Staub
Simplified absorption correction for combined fluorescence and absorption tomography on human bone samples
to be submitted to Nucl. Instr. Meth.

The obtained results have been presented as seminar talks as well as oral and poster presentations at following conferences:

1. N. Zoeger
Determination of Calcium and Lead Distribution in Human Bone by Synchrotron – Micro - XRF
13th European Students Conference, Charite, Berlin, Germany, 2002
2. N. Zoeger, P. Wobrauschek, G. Pepponi, C. Strel, S. Zamini, G. Falkenberg, W. Osterode
Elemental Distribution of Pb and Ca in Human Bones Investigated by SR-XRF
Hamburg Workshop, Application of Synchrotron Radiation in Chemistry- Status and Future, Hamburg, Germany, 2002
3. P. Wobrauschek, N. Zoeger, G. Pepponi, C. Strel, , S. Zamini, G. Falkenberg, W. Osterode
SR-XRF of bone samples: Differences in Pb and other Trace element concentrations in Bone Transition Zones
Jahrestagung der ÖPG, Leoben, Austria, 2002
4. P. Wobrauschek, N. Zoeger, G. Pepponi, C. Strel, G. Falkenberg, W. Osterode
Variation of Pb and Ca Concentration in Compact and Spongy Bone Determined by μ -SRXRF at HASYLAB, Beamline L
52nd Annual Denver X-ray Conference, Denver, USA, 2003
5. C. Strel, N. Zoeger, P. Wobrauschek, G. Pepponi, G. Falkenberg, P. Roschger, W. Osterode
Determination of Trace Element Distribution at Transition Zones by Synchrotron μ -XRF on Human Bone Slices at HASYLAB
Satellite Meeting of TXRF Conference, Osaka, Japan, 2003

6. P. Wobrauschek, N. Zoeger, G. Pepponi, C. Strel, P. Roschger, W. Osterode, G. Falkenberg
Seminarvortrag: Spatially Resolved Analysis of Major, Minor and Trace Elements in Human Bone by EDXRS
Max Planck Institute for Colloids and Interfaces, Postdam, Germany, 2003
7. P. Wobrauschek, N. Zoeger, G. Pepponi, C. Strel, P. Roschger, W. Osterode, G. Falkenberg
Seminarvortrag: Spatially Resolved Analysis of Major, Minor and Trace Elements in Human Bone by EDXRS
Academy of Mining and Metallurgy, Krakow, Poland, 2003
8. N. Zoeger, P. Wobrauschek, C. Strel, G. Pepponi, G. Falkenberg, P. Roschger, W. Osterode
Synchrotron μ -XRF on Human Bone Slices- Determination of Trace Element Distribution
17th International Congress on X-ray Optics and Microanalysis, Chamonix, France, 2003
9. P. Wobrauschek, C. Strel, G. Pepponi, N. Zoeger, G. Falkenberg, W. Osterode
Major and Trace Element Distribution in 200 μ m thick Human Hip Bone Slices Analysed with Microbeam Equipment at HASYLAB Beamline L
HASYLAB User-meeting, Hamburg, Germany, 2003
10. N. Zoeger, P. Wobrauschek, C. Strel, G. Pepponi, G. Falkenberg, P. Roschger, W. Osterode
Determination of Trace Element Distribution in Human Bone Slices by Synchrotron- μ XRF
Jahrestagung der ÖPG, Salzburg, Austria, 2003
11. W. Osterode, N. Zoeger, G. Pepponi, C. Strel, S. Zamini, P. Wobrauschek, G. Falkenberg
Lead in Different Bone Compartments Determined by SR-XRF
ICOH, Iguassu, Brasil, 2003
12. N. Zoeger, P. Wobrauschek, C. Strel, E. Chinea-Cano, D. Wegrzynek, P. Roschger, R. Simon, S. Staub, G. Falkenberg
3D Elemental Imaging in Human Bone by SR- μ XRF
EXRS Conference, Alghero, Italy, 2004
13. P. Wobrauschek, N. Zoeger, C. Strel, C. Jokubonis, G. Pepponi, P. Roschger, G. Falkenberg, W. Osterode
Elemental Distribution in Human Articular Bone by SR- μ XRF
EXRS Conference, Alghero, Italy, 2004
14. N. Zoeger, C. Strel, P. Wobrauschek, C. Jokubonis, G. Pepponi, P. Roschger, S. Bohic, W. Osterode
Synchrotron Micro XRF on Human Brain Slices
EXRS Conference, Alghero, Italy, 2004

15. N. Zoeger, P. Wobrauschek, C. Strel, E. Chinea-Cano, D. Wegrzynek, P. Roschger, R. Simon, S. Staub, G. Falkenberg
3D Synchrotron Micro RFA an Menschlichen Knochen
54. Jahrestagung der ÖPG, Linz, Austria, 2004
16. N. Zoeger, P. Wobrauschek, C. Strel, C. Jokubonis, G. Pepponi, P. Roschger, G. Falkenberg, W. Osterode
Elementverteilung in Menschlichen Gelenksknochen
54. Jahrestagung der ÖPG, Linz, Austria, 2004
17. N. Zoeger, C. Strel, P. Wobrauschek, C. Jokubonis, G. Pepponi, P. Roschger, S. Bohic, W. Osterode
Verteilung von Haupt-Neben und Spurenelementen im menschlichen Gehirn
54. Jahrestagung der ÖPG, Linz, Austria, 2004
18. N. Zoeger, P. Wobrauschek, C. Strel, E. Chinea-Cano, D. Wegrzynek, P. Roschger, R. Simon, S. Staub, G. Falkenberg
3D SR- μ -XRF on Human Bone Samples: Fluorescence Tomography and Confocal μ -XRF
IX Seminario Latinoamericano de Analisis por tecnicas de rayos X, Villa Giardino, Cordoba, Argentina, 2004
19. N. Zoeger, P. Wobrauschek, C. Strel, C. Jokubonis, G. Pepponi, P. Roschger, S. Bohic, W. Osterode
SR- μ -XRF of Human Brain: Element Mapping of Pb and Other Trace Elements
IX Seminario Latinoamericano de Analisis por tecnicas de rayos X, Villa Giardino, Cordoba, Argentina, 2004
20. N. Zoeger, P. Wobrauschek, C. Strel, C. Jokubonis, G. Pepponi, P. Roschger, G. Falkenberg, W. Osterode
SR- μ -XRF of Various Areas of Human Articular Bones: Determination of the Elemental Distribution of Pb and Other Major and Trace Elements
IX Seminario Latinoamericano de Analisis por tecnicas de rayos X, Villa Giardino, Cordoba, Argentina, 2004
21. N. Zoeger, P. Wobrauschek, C. Strel
3D SR μ -XRF on Human Bone Samples
53rd Annual Denver X-ray Conference, Steamboat Springs, USA, 2004
22. N. Zoeger, P. Wobrauschek, C. Strel, C. Jokubonis, G. Pepponi, P. Roschger, G. Falkenberg, W. Osterode
Elemental Distribution In Various Areas of Human Articular Bones by SR μ -XRF
53rd Annual Denver X-ray Conference, Denver, Steamboat Springs, USA, 2004
23. N. Zoeger, C. Strel, P. Wobrauschek, C. Jokubonis, G. Pepponi, P. Roschger, S. Bohic, W. Osterode
Elemental Mapping of Human Brain by SR- μ XRF
53rd Annual Denver X-ray Conference, Denver, Steamboat Springs, USA, 2004

24. N. Zoeger, P. Wobrauschek, C. Strel, G. Falkenberg, P. Roschger
Elemental Mapping of Human Bone by Confocal SR micro-XRF
HASYLAB User-meeting, Hamburg, Germany 2005

The study on the elemental distribution in human brain was presented as poster at the 53rd Annual Denver X-Ray Conference 2004, Steamboat Springs, Colorado, USA, and was assigned a Best Poster Award

N. Zoeger, C. Strel, P. Wobrauschek, C. Jokubonis, G. Pepponi, P. Roschger, S. Bohic, W. Osterode, *Elemental Mapping of Human Brain by SR- μ XRF*, 53rd Annual Denver X-ray Conference, Denver, Steamboat Springs, USA, 2004

Kurzfassung

Im Rahmen dieser Dissertation wurde die Verteilung der chemischen Elemente in menschlichem Gewebe (Knochen und Gehirn) mittels Synchrotronstrahlungsinduzierter Mikro-Röntgenfluoreszenzanalyse (SR μ -RFA) untersucht. Diesbezüglich wurden Scan- und Tomographieexperimente an Mikrofokus beamlines von drei verschiedenen Synchrotronstrahlungseinrichtungen (HASYLAB, Hamburg, ANKA, Karlsruhe, ESRF, Grenoble), wo der Fragestellung angepasster Photonenfluss als auch geeignete Röntgenoptiken zur Verfügung standen, durchgeführt.

Im Fall von Knochen konnten durch Überlagern von Bildern, generiert aus der Messung rückgestreuter Elektronen (backscattered electron images (BEI)), die über die strukturellen Eigenschaften des Gewebes Auskunft geben, und Resultaten von orts aufgelösten μ -RFA Messungen Knochenzonen identifiziert werden, an denen sich die verschiedenen Elemente unterschiedlich anlagern. Bei allen Messungen wurde dabei spezielles Augenmerk auf das Schwermetall Blei (Pb) gelegt, das aufgrund seiner toxischen Wirkung auf den menschlichen Organismus von größtem medizinischen Interesse ist.

Beginnend mit Messungen an 4mm dicken Kochenschnitten wurde die örtliche Auflösung und somit die Genauigkeit der Analysemethode durch Verringern der Probendicke und letztendlich durch Verwenden einer sogenannten konfokalen Messgeometrie über die Projektdauer stetig verbessert. Aus dem Vergleich von Ergebnissen von zweidimensionalen orts aufgelösten μ -RFA mit BEI, konnte festgestellt werden, dass Pb vornehmlich an der sogenannten „tidemark“, eine Linie, die kalzifiziertes und nichtkalzifiziertes Gewebe trennt und als Zone mit hoher metabolischer Aktivität eingestuft wird, akkumuliert. Zusätzlich wurde eine Korrelation zwischen Pb und Zn an dieser Knochenzone gefunden. Bei der Untersuchung von Knochen mit doppelter tidemark wurde festgestellt, dass möglicherweise ein Zeitunterschied zwischen der Anlagerung von Pb und jener von Zn besteht.

Ähnliche Ergebnisse konnten aus kombinierten Absorptions- und Fluoreszenztomographie Experimenten abgeleitet werden, die ebenfalls die Akkumulation von Pb und Zn in mikroskopischen Strukturen des Knochens zeigten.

Weiters wurde die Elementverteilung im menschlichen Gehirn untersucht, um festzustellen, ob in diesem Gewebe Zonen erhöhter Pb Anlagerung vorliegen. Obwohl sich in Gehirnproben die Zuordnung der elementspezifischen Bilder aus μ -RFA Messungen ungleich

schwieriger gestaltet als im Knochen, konnte in allen untersuchten Proben von Frontal Cortex, Hippocampus und Thalamus eine inhomogene Bleiverteilung nachgewiesen werden.

Acknowledgments

This work would never have been possible without my girlfriend Nina, my parents Eveline and Norbert, and my grandmother Rosa, who have supported and encouraged me throughout the preparation of this thesis. Furthermore I would like to thank my friends Christian, Stefan, Klaus and Sebastian for our common project apart from work.

I would like to express my gratitude to my supervisor Peter Wobrauschek and Christina Strelj for the guidance and the scientific freedom they endowed me with since the beginning.

Many more are to be thanked for the help in executing the experiments and the fruitful discussions. They will be mentioned according to the geographical distance of their institution to the Atominstitut.

- my colleagues and friends Christoph Jokubonis and Giancarlo Peponi, who supported me during countless beamtimes and with data evaluation;
- Paul Roschger, Jochen Hofstaetter, Ludwig Boltzmann-Institute of Osteology, UKH Meidling, Vienna for sample preparation and discussion of the data.
- Wolf Osterode AKH Vienna, for initiating the project
- Dariusz Wegrzynek, Ernesto Chinea-Cano, IAEA Seibersdorf Laboratories, XRF Group, Instrumentation Unit, Seibersdorf, Austria, for sample preparation and help with the tomography measurements.
- Peter Fratzl, Max-Planck-Institut für Kolloid und Grenzflächenforschung, Golm, Germany
- Rolf Simon, Susanne Staub, ANKA, Karlsruhe, Germany
- Gerald Falkenberg, HASYLAB, beamline L, Hamburg, Germany
- Silvain Bohic, ESRF, ID-22, Grenoble, France

The experimental work for this thesis has been carried out under the frame of FWF (Austrian Science Fund) project “Determination of Pb concentration in human bone and tissue”, Project Number P 15740.

Contents

1	INTRODUCTION	3
1.1	HISTORICAL DEVELOPMENT	3
2	X-RAY FLUORESCENCE ANALYSIS	5
2.1	ENERGY DISPERSIVE X-RAY FLUORESCENCE ANALYSIS	5
2.2	ENERGY DISPERSIVE X-RAY DETECTORS	6
2.2.1	Semiconductor detectors	6
2.2.2	Drift detectors.....	7
2.3	INTENSITY OF THE CHARACTERISTIC RADIATION	8
2.4	SPECTRUM EVALUATION	11
3	X-RAY OPTICS	12
3.1	OPTICAL THEORY OF X-RAYS	12
3.1.1	Total reflection	16
3.2	REFLECTIVE X-RAY OPTICS	17
3.2.1	Multilayer optics	17
3.2.2	Mirror optics.....	18
3.3	CAPILLARY OPTICS.....	19
3.3.1	Monocapillary lenses.....	19
3.3.2	Polycapillary optics	22
3.4	REFRACTIVE X-RAY OPTICS	23
3.4.1	Compound refractive lenses.....	23
4	MICROSCOPIC X-RAY FLUORESCENCE ANALYSIS	26
4.1	INTRODUCTION.....	27
4.2	INSTRUMENTATION	28
4.3	DATA EVALUATION AND IMAGE PROCESSING	29
4.4	QUANTIFICATION	30
4.4.1	Information depth.....	32
4.4.2	Monte Carlo Simulations	34
4.5	CONFOCAL MICRO XRF.....	34
4.5.1	Energy dependence of the detection volume.....	36
5	MICRO TOMOGRAPHY	38
5.1	LINE INTEGRALS AND PROJECTIONS	38
5.2	RECONSTRUCTION ALGORITHM	41
5.2.1	Fourier Slice Theorem.....	41
5.2.2	Direct Backprojection	43
5.2.3	Filtered Backprojection.....	46
5.3	X-RAY ABSORPTION TOMOGRAPHY	49
5.4	X-RAY FLUORESCENCE TOMOGRAPHY.....	50
6	X-RAY SOURCES	53
6.1	X-RAY TUBES	53
6.2	SYNCHROTRON RADIATION.....	55
6.2.1	Origin of synchrotron radiation.....	55
6.2.2	Intensity and spectral distribution	56

6.2.3	Polarization.....	58
6.2.4	Insertion devices.....	60
7	ELEMENTAL DISTRIBUTION IN HUMAN BONES	65
7.1	MEDICAL INTRODUCTION	65
7.1.1	Effects of lead on the human organism.....	65
7.1.2	Function and structure of human bone.....	66
7.2	MICRO XRF ON 4MM BONE SLICES	68
7.2.1	Experimental setup.....	68
7.2.2	Samples / sample preparation.....	70
7.2.3	Results and discussion.....	71
7.2.4	Conclusions	74
7.3	MICRO XRF ON 200 μ M BONE SLICES	74
7.3.1	Experimental Setup	74
7.3.2	Samples / sample preparation.....	74
7.3.3	Backscattered electron Imaging	75
7.3.4	Results and discussion.....	76
7.3.5	Conclusions	83
7.4	CONFOCAL MICRO XRF ON BONE SLICES	84
7.4.1	Experimental setup.....	84
7.4.2	Results and discussion.....	87
7.4.3	Conclusions	95
7.5	ABSORPTION TOMOGRAPHY OF CORTICAL BONE	95
7.5.1	Experimental setup.....	95
7.5.2	Samples / sample preparation.....	97
7.5.3	Results	98
7.6	COMBINED FLUORESCENCE-ABSORPTION TOMOGRAPHY OF CORTICAL BONE	100
7.6.1	Experimental setup.....	100
7.6.2	Results	101
7.6.3	Conclusions	107
8	ELEMENTAL DISTRIBUTION IN HUMAN BRAIN.....	109
8.1	INTRODUCTION.....	109
8.2	EXPERIMENTAL SETUP.....	109
8.3	SAMPLES / SAMPLE PREPARATION	110
8.4	RESULTS.....	111
8.5	CONCLUSIONS	114
9	CONCLUDING REMARKS.....	115
	BIBLIOGRAPHY	118

1 Introduction

Microscopic X-ray fluorescence analysis (micro-XRF, μ -XRF) has nowadays, besides total reflection X-ray fluorescence analysis (TXRF), become one of the most important variants of energy dispersive X-ray fluorescence analysis (EDXRF). It is based on the local excitation and analysis of microscopically small area of a larger sample, providing information on the distribution of the chemical elements in the sample under investigation. Using synchrotron radiation, with its outstanding physical properties of natural collimation and polarization, as excitation sources elevates the performance of μ -XRF and extends its frontiers.

1.1 Historical development

The first μ -XRF spectrometers based on a micro-beam produced by conventional X-ray tubes and a set of suitable apertures and/or cross-slits have been employed in the 1960s [1,2]. Although, the use of photons as an excitation source has a number of advantages over charged particle excitation, these early systems did not receive much attention at the time, which was mainly due to the low count rates observed. In the late 1980s [3,4], when first attempts were made to use straight glass capillaries as waveguides to transport the X-rays from where they are generated towards the sample, μ -XRF was effectively re-discovered. With the development of parabolic and ellipsoidal capillaries [5,6], which concentrate X-rays instead of transporting them, the basis for modern μ -XRF spectrometers was created. The very recent development of monolithic polycapillary half lenses led to a further improvement of μ -XRF systems [7-10]. Since with those optics a rather large solid angle of the X-ray source is captured and the radiation is focused onto a point several millimeters or even centimeters out of the lens itself spatial resolved measurements of larger samples are relatively easy accomplished. Using polycapillary lenses together with low power tubes with a focal spot on the anode of some μm , nowadays high-intensity micro-beams of about 30-100 μm can be generated reaching detection limits in the pg range [7]. When monochromatic synchrotron radiation is employed instead of X-ray tubes, the detection limits can be reduced to the fg level [11] allowing for trace element analysis.

In general the development of μ -XRF as an analytical tool is strongly linked to the development of X-ray optics capable of concentrating photons to restricted volume of the

specimen. Therefore the recent increase in popularity of μ -XRF has to be attributed to the availability of relatively easy devices for X-ray beam concentration.

2 X-ray Fluorescence Analysis

X-ray fluorescence analysis (XRF) is a well established method for qualitative and quantitative multi element analysis of bulk samples. When a photon of sufficient energy is absorbed by an atom of the sample an electron is ejected from an inner shell (e.g.: K-shell), and the atom becomes ionized. If the vacancy in the shell of the atom is filled by an electron from an higher level (e.g.: L-shell) of the atom, the transition is accompanied by the emission of an X-ray photon ($K\alpha$ -line). In competition to this photon emission is the Auger process, resulting in the emission of an Auger electron. XRF as an analytical tool is based on the fact, that the energy of each of the emitted X-ray photons is characteristic for the chemical element from which it originates, and that the number of emitted photons is directly proportional to the amount of atoms present in the sample. Due to their working principle a distinction between wavelength dispersive and energy dispersive X-ray spectrometers (see next paragraph) can be made.

2.1 Energy dispersive X-ray fluorescence analysis

The typical setup of an energy dispersive X-ray spectrometer is shown in Figure 2.1. It consists of an X-ray source providing primary photons sufficient for excitation of fluorescent radiation in the sample, a sample stage for carrying the specimen and an energy dispersive X-ray detector with appendant electronics. In comparison to wavelength dispersive systems it is possible to collect the whole spectrum relevant for analysis at once leading to drastic reduction in measuring time. Together with the electronics for pulse processing (amplifier, analog to digital converter and multichannel analyzer) the energy dispersive detector can be denoted as the core of the system and will therefore be explained in the next paragraph.

As shown in Figure 2.1 angles between beam - specimen - detector are usually fixed to 45° each for standard XRF measurements. Since the differential cross section for inelastic scattering has a minimum at 90° , such geometries are advantageous in order to have a reduced background signal in the spectrum.

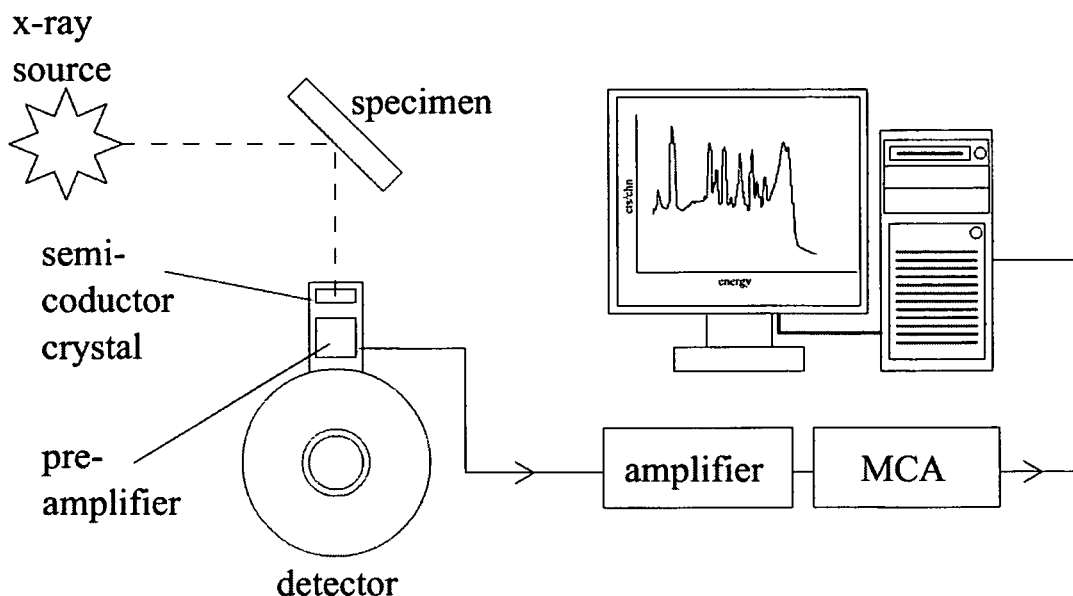


Figure 2.1: Scheme of a typical energy dispersive X-ray spectrometer

2.2 Energy dispersive X-ray detectors

The detection of X-rays is accomplished by transforming the energy of the photons into electrical pulses available for further processing. In case of energy dispersive (ED) detectors the generated pulse is proportional to the energy of the incoming (fluorescence) photon absorbed in the active volume of the detector. Generally a distinction between two types of ED detectors, namely semiconductor detectors and drift detectors, can be drawn.

2.2.1 Semiconductor detectors

The detector crystal (Figure 2.2) of these devices are semiconductor diodes having a P-I-N structure, where the intrinsic (I) region is sensitive to ionizing radiation, such as X-rays and γ -rays. Under reverse-biasing an electric field extends across the intrinsic region. A photon absorbed within this active volume will produce either photoelectrons, Compton -, or Auger electrons. When these electrons loose energy, electron-hole pairs are created, which are moved to the P and N electrodes by the applied electric field. The produced total charge is proportional to the energy deposited by the incoming photon and is converted into a voltage pulse by the charge sensitive preamplifier. To establish the contact between the semiconductor and the preamplifier a thin gold layer is evaporated on the surface of the detector crystal.

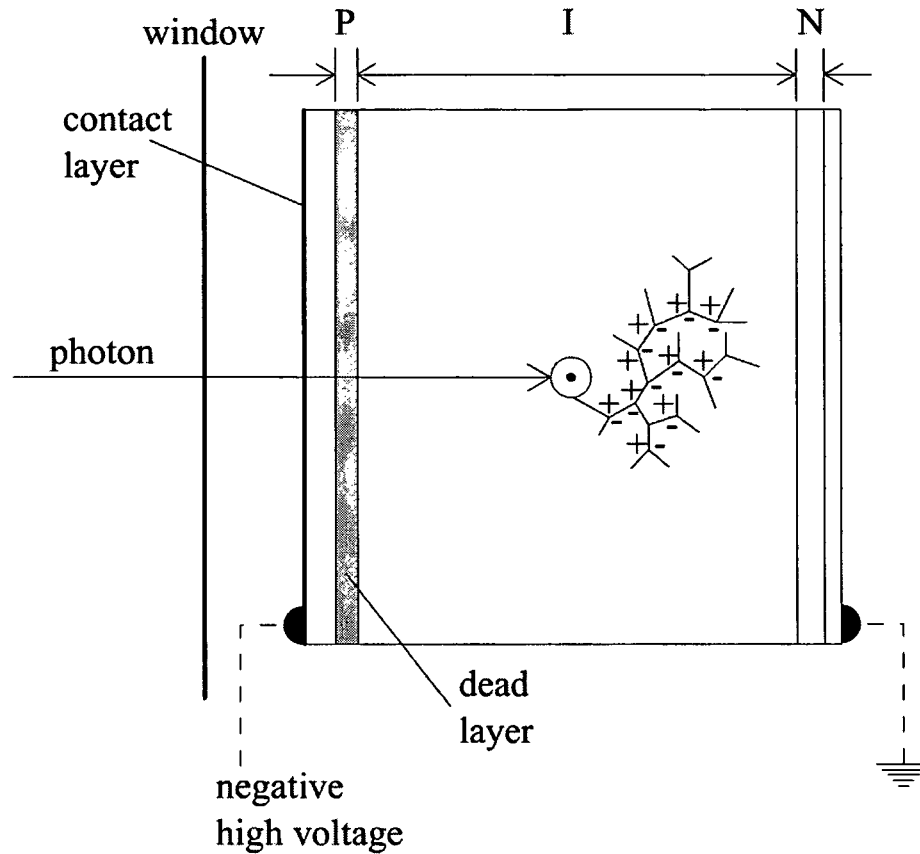


Figure 2.2: Schematic representation of a semi conductor detector crystal

The crystal is protected against moisture and other contaminants by a thin window of a low Z material (mostly Be) with a typical thickness of about 10-100 μm .

Because of the relatively low band gap of the semiconductor the detector must be cooled in order to prevent thermal generation of charge carriers, which is usually performed by a liquid nitrogen (LN₂) cooling.

2.2.2 Drift detectors

Silicon drift detectors (SDD) are based on the principle of sideward depletion [12] by adding an additional field parallel to the semiconductor surface which transports the electrons generated in the active volume (see previous paragraph) to the anode of the detector. The scheme of a SDD is shown in Figure 2.3. N-type silicon is covered on both sides with P contacts. While the back contact (entrance side for photons) is a full disc of a P-type semiconductor, the front contacts are arranged as concentric rings of the same material. By potential dividers implanted in the surface all P-type rings are kept at different potentials and therefore a voltage gradient between the inner and the outer ring is generated in a way that the

readout anode is the point of minimum potential energy for electrons. Therefore all electrons generated by interactions of the incoming photons with the active volume of the detector will be swept to the anode leading to a charge pulse directly proportional to the photon energy.

To minimize the electronic noise in semiconductor detectors the capacity of the readout anode has to be kept as low as possible. In contradiction to conventional detectors (e.g. Si-pin diodes) the capacity of the readout anode is independent from the size of the active volume of the detector, and is therefore not a limiting factor when constructing SDDs with a larger area.

Compared to Si(Li) detectors SDDs reach their optimal energy resolution at a temperature of about -15°C allowing to replace the LN2 cooling by a peltier cooler which makes the handling of the detector much easier. A further advantage of the SDD is the ability of handling high count rates up to 10^6 photons/s. As a disadvantage it might be denoted that due to the thickness of the used detector crystals ($300\mu\text{m}$) the detection of higher energy photons (above 20 keV) can not efficiently be accomplished.

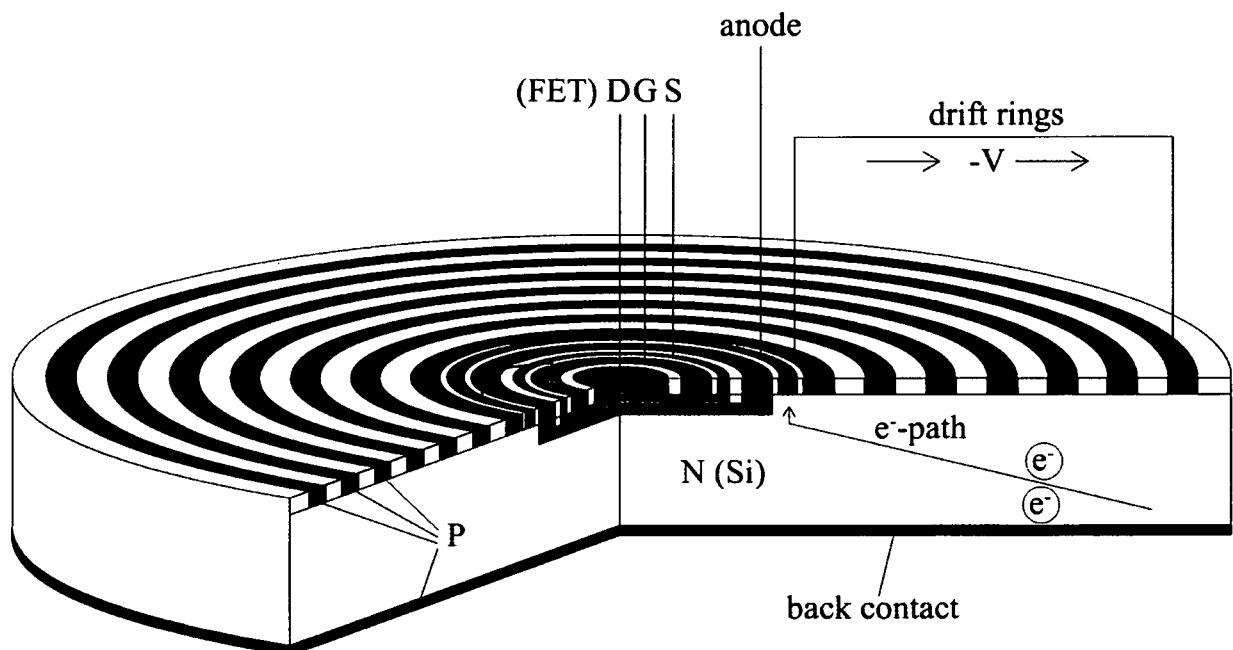


Figure 2.3: Schematic representation of the active volume of a Si drift detector

2.3 Intensity of the characteristic radiation

For simplicity of the discussion let us assume a point X-ray source and detector as well as monochromatic excitation. The number of X-ray photons per second emitted by the X-ray source in the energy interval E_0 to $E_0 + dE_0$, within the differential solid angle $d\Omega_0$ are defined as $I_0(E_0) dE_0 d\Omega_0$. These photons strike the surface of the specimen at an incident angle ϕ_i .

The number of characteristic photons produced in a layer of thickness dz located at a depth z under the surface is to be calculated (see Figure 2.4).

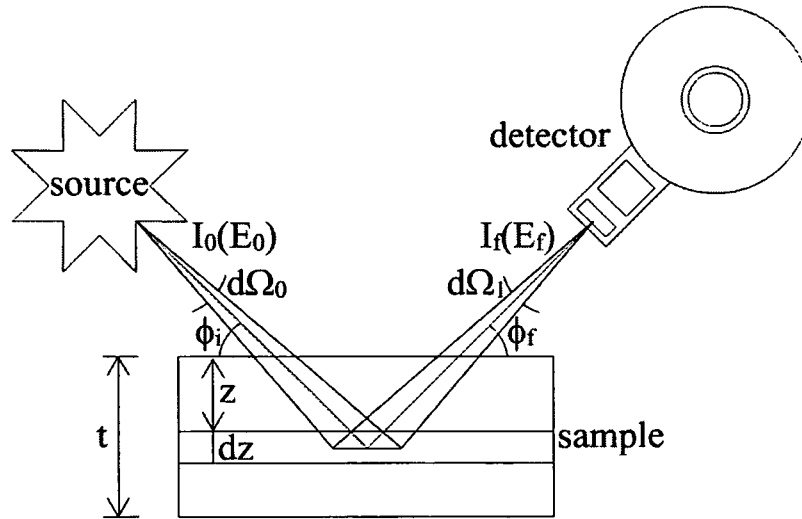


Figure 2.4: Derivation of the intensity of the characteristic radiation

Let us consider the X-ray line of a certain element ξ contained in a sample s , originated by the transition of an electron between the shells $j \rightarrow k$.

The processes which have to be taken into account are:

1. attenuation of the primary beam
2. photoelectric absorption of the primary beam by the atoms of the element ξ
3. repartition of the vacancies in the various shells
4. probability of a fluorescence emission (vs. emission of Auger electrons)
5. probability of the emission of the X-ray line (or group of lines) considered
6. attenuation of the fluorescence radiation
7. detector efficiency for the energy of the line considered

$$dI_{\xi k} \propto \underbrace{\exp\left[-\mu_{s,E_0} \frac{z}{\sin \phi_i}\right]}_1 \underbrace{W_{\xi} \left(\frac{\tau}{\rho}\right)}_2 \underbrace{\rho_s dz \frac{r_{\xi k} - 1}{r_{\xi k}}}_{3} \underbrace{\omega_{\xi k}}_4 \underbrace{p_{\xi k}}_5 \underbrace{\exp\left[-\mu_{s,E_{\xi k}} \frac{z}{\sin \phi_f}\right]}_6 \underbrace{\epsilon_{E_{\xi k}}}_{7} \quad (2.1)$$

μ_{s,E_0} linear absorption coefficient of the sample for the energy E_0

W_{ξ} weight fraction of the element ξ

$\left(\frac{\tau}{\rho}\right)_{E_{\xi_0}}$	photoelectric mass absorption cross section
ρ_s	density of the sample
$r_{\xi k}$	jump ratio of the absorption edge of the shell k
$\omega_{\xi k}$	fluorescence yield for the shell k
$p_{\xi j k}$	probability of the line with energy $E_{\xi j k}$
$\mu_{s, E_{\xi k}}$	linear absorption coefficient of the sample for the energy $E_{\xi k}$
$\varepsilon_{E_{\xi k}}$	detector efficiency for the energy $E_{\xi k}$

The concentration of the element, usually the unknown, appears as a weight fraction in factor 2. in equation 2.1. For the emission of photons of the characteristic energy $E_{\xi j k}$ only the photoelectric absorption due to the element ξ has to be taken into account. For a sample containing more than one element the total photoelectric mass absorption coefficient is given by

$$\left(\frac{\tau}{\rho}\right)_{sample} = \sum_{\xi} W_{\xi} \left(\frac{\tau}{\rho}\right)_{\xi} \quad (2.2)$$

Defining a sensitivity factor for the system for the element ξ as

$$S_{\xi k} = \left(\frac{\tau}{\rho}\right)_{\xi} \frac{r_{\xi k} - 1}{r_{\xi k}} \omega_{\xi k} p_{\xi j k} \varepsilon_{E_{\xi k}} \quad (2.3)$$

and grouping the geometrical factors influencing the measurement such as detector size and distance, source size and distance to a generic geometry factor G one gets

$$\begin{aligned} dI_{\xi j k} &= I_0 G \exp\left[-\mu_{s, E_0} \frac{z}{\sin \phi_i}\right] S_{\xi k} W_{\xi} \rho_s dz \exp\left[-\mu_{s, E_{\xi k}} \frac{z}{\sin \phi_f}\right] \\ &= I_0 G S_{\xi k} W_{\xi} \rho_s \exp\left[-\left(\frac{\mu_{s, E_0}}{\sin \phi_i} + \frac{\mu_{s, E_{\xi k}}}{\sin \phi_f}\right) z\right] dz \end{aligned} \quad (2.4)$$

In order to obtain the fluorescence intensity from the whole sample, the contribution $dI_{\xi jk}$ has to be integrated over the whole sample thickness (from 0 to t)

$$\begin{aligned}
 I_{\xi jk} &= I_0 G S_{\xi jk} W_{\xi} \rho_s \int_0^t \exp \left[- \left(\frac{\mu_{s,E_0}}{\sin \phi_i} + \frac{\mu_{s,E_{\xi jk}}}{\sin \phi_f} \right) z \right] dz \\
 &= I_0 G S_{\xi jk} W_{\xi} \rho_s \frac{1 - \exp \left[- \left(\frac{\mu_{s,E_0}}{\sin \phi_i} + \frac{\mu_{s,E_{\xi jk}}}{\sin \phi_f} \right) t \right]}{\left(\frac{\mu_{s,E_0}}{\sin \phi_i} + \frac{\mu_{s,E_{\xi jk}}}{\sin \phi_f} \right)} \quad (2.5)
 \end{aligned}$$

All the above mentioned holds for homogeneous samples, so called bulk samples and has to be modified for the case of micro analysis where the main objective is to determine the elemental distribution in the analyte. Concerning these considerations the readers attention might be drawn to chapter 4 of this thesis.

2.4 Spectrum evaluation

When performing X-ray fluorescence measurements using energy dispersive detectors spectra, counts versus energy are obtained. Characteristic X-ray lines appear as gaussian peaks superimposed over a background signal due to scattering effects or detector artifacts such as low energy tailing, and other possible phenomena. X-ray lines from different elements might be energetically very close to each other and not resolvable by the detector. In this case other lines from the same group (e.g. $K\alpha$ and $K\beta$) can be used to deconvolute overlapping peaks since the ratio between the lines is known. In the present work the software AXIL from the QXAS [13] package, developed by the International Atomic Agency (IAEA), has been used to deduce the fluorescence intensity of the elements and the background they are superimposed onto from the fluorescence spectra. In short, this software uses the method of non linear least squares fitting to fit the spectrum with an analytical function.

3 X-ray Optics

In general, there are many technical difficulties of optically controlling, forming and focusing an X-ray beam compared to an electron or proton beam. Despite the fact that the efficiency of optical systems working in the X-ray regime is still poor compared to optics for charged particles, nowadays great efforts are made developing X-ray lenses.

Due to their working principles X-ray optics can be divided in three groups namely reflective optics, refractive optics and capillary optics.

3.1 Optical theory of X-rays

The propagation of X-rays in a refractive medium is described using the same classical formalisms as for visible light. The basic concept of this optical theory is, that every medium can be described by a *refractive index* n , which is related to its dielectric properties. In case of X-rays n is a complex number. Let \mathbf{E} be an electromagnetic field and \mathbf{D} the displacement field which is generated when \mathbf{E} interacts with the atoms of the medium.

According to the Maxwell theory \mathbf{D} can be written as

$$D = \epsilon_r E = E + 4\pi P \quad (3.1)$$

accordingly

$$\epsilon_r = 1 + 4\pi \frac{P}{E} \quad (3.2)$$

According to the wave equation the refractive index n can be written as

$$n = \frac{c}{v} = \sqrt{\epsilon_r} \quad (3.3)$$

where v is the velocity of propagation of the wave front (phase velocity).

For most materials $\epsilon > 1$ so that n is greater than unity and therefore the velocity v is smaller than in vacuum. Such velocity is correlated with the phenomenon of refraction and is described by Snell's law (Figure 3.1)

$$\frac{\cos\theta_1}{\cos\theta_2} = \frac{v_1}{v_2} \quad (3.4)$$

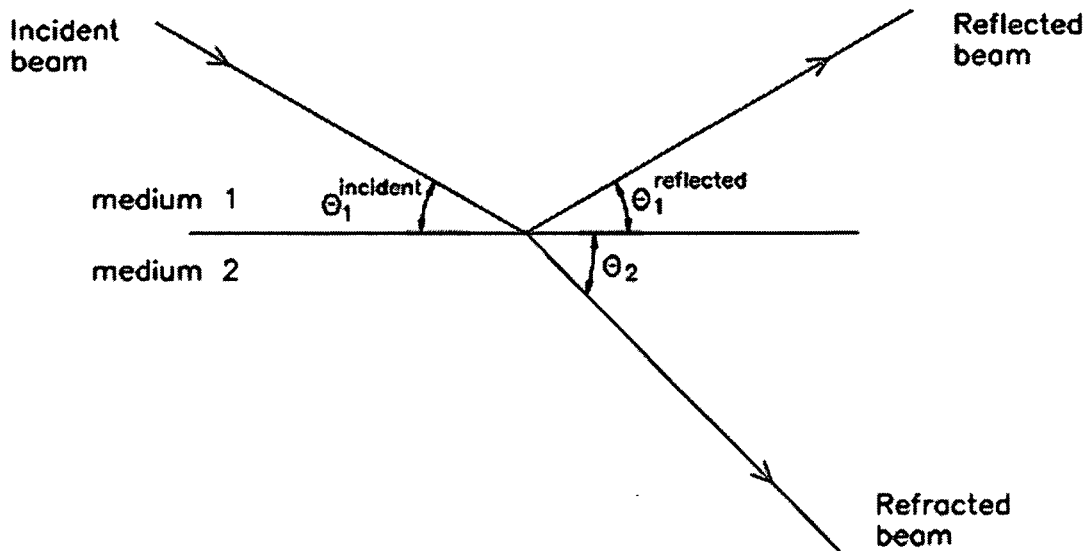


Figure 3.1: Schematic representation of Snell's law in the optical region [14]

The refractive index n as well as the velocity v depend on the wavelength λ of the electromagnetic wave.

In the X-ray regime the refractive index n is smaller than unity. This leads to a velocity $v > c$ and to a refracted beam which is closer to the surface than the reflected one. Moreover X-rays are absorbed in matter, due to scattering and photoelectric absorption, described by Beer Lambert's law

$$I(x) = I_0 \exp(-\mu x) \quad (3.5)$$

where μ is the *linear mass absorption coefficient*. To account for this phenomenon a complex refractive index \tilde{n} is introduced, which is preferably written as

$$\tilde{n} = 1 - \delta - i\beta \quad (3.6)$$

δ is related to the dispersive nature of the medium (and is therefore associated to the atomic structure), while β describes the absorption in the matter.

$$\delta = \frac{Ne^2 \lambda^2}{2\pi mc^2} \quad (3.7)$$

$$\beta = \frac{\lambda\mu}{4\pi} \quad (3.8)$$

where N is the number of dispersive electrons per unit volume of the material.

Let us consider a plane wave, propagating in a medium with refractive index $\tilde{n}_1 = 1 - \delta_1 - i\beta_1$, impinging on a smooth surface of another medium characterized by $\tilde{n}_2 = 1 - \delta_2 - i\beta_2$. If $\tilde{n}_1 \neq \tilde{n}_2$ a reflected and a transmitted wave is generated. Assuming continuity of the electric- and magnetic field components at the boundary the following expressions for the *reflectivity* R can be derived from the Fresnel formulas

$$r_p = \frac{A_{rp}}{A_{ip}} = \frac{\tan(\phi_i - \phi_t)}{\tan(\phi_i + \phi_t)} \quad (3.9)$$

$$R_p = r_p \cdot r_p^* \quad (3.10)$$

$$r_s = \frac{A_{rs}}{A_{is}} = \frac{\sin(\phi_i - \phi_t)}{\sin(\phi_i + \phi_t)} \quad (3.11)$$

$$R_s = r_s \cdot r_s^* \quad (3.12)$$

where the indices i , r and t represent the incident, reflected and transmitted amplitudes, p and s are associated with parallel and perpendicular components, and ϕ_i and ϕ_t are the angles of the incident and transmitted wave in the plane of incidence.

Using Snell's law, R can be expressed in terms of glancing incidence angle θ_i , and the two refractive indices of the media

$$r_p = \frac{(1 - \delta_2 - i\beta_2)^2 \sin \theta_i - (1 - \delta_1 - i\beta_1)^2 [(1 - \delta_2 - i\beta_2)^2 - (1 - \delta_1 - i\beta_1)^2 \cos^2 \theta_i]^{\frac{1}{2}}}{(1 - \delta_2 - i\beta_2)^2 \sin \theta_i + (1 - \delta_1 - i\beta_1)^2 [(1 - \delta_2 - i\beta_2)^2 - (1 - \delta_1 - i\beta_1)^2 \cos^2 \theta_i]^{\frac{1}{2}}} \quad (3.13)$$

$$r_s = \frac{(1 - \delta_1 - i\beta_1) \sin \theta_i - [(1 - \delta_2 - i\beta_2)^2 - (1 - \delta_1 - i\beta_1)^2 \cos^2 \theta_i]^{\frac{1}{2}}}{(1 - \delta_1 - i\beta_1) \sin \theta_i + [(1 - \delta_2 - i\beta_2)^2 - (1 - \delta_1 - i\beta_1)^2 \cos^2 \theta_i]^{\frac{1}{2}}} \quad (3.14)$$

For simplification let medium 1 be air or vacuum ($\tilde{n}_1 = 1 - \delta_1 - i\beta_1 = 1$) and substitute the remaining refractive index $\tilde{n}_1 = \tilde{n} = 1 - \delta - i\beta$. Under the assumption of a small glancing angle θ_i the parallel and perpendicular components become almost equal, and equations (3.13) and (3.14) can be rewritten as ($\sin \theta_i = \theta_i$; δ^2 neglected)

$$r_s = r_p = \frac{\theta_i - [\theta_i^2 - 2(\delta - i\beta)]^{\frac{1}{2}}}{\theta_i + [\theta_i^2 - 2(\delta - i\beta)]^{\frac{1}{2}}} \quad (3.15)$$

Using the substitution

$$[\theta_i^2 - 2(\delta - i\beta)]^{\frac{1}{2}} = a + ib \quad (3.16)$$

the reflectivity R can be written as

$$R(\theta, E) = |r|^2 = \frac{(\theta_i - a)^2 + b^2}{(\theta_i + a)^2 + b^2} \quad (3.17)$$

where

$$a^2 = \frac{1}{2} [(\theta_i^2 - 2\delta)^2 + 4\beta^2]^{\frac{1}{2}} + \theta_i^2 - 2\delta \quad (3.18)$$

$$b^2 = \frac{1}{2} [(\theta_i^2 - 2\delta)^2 + 4\beta^2]^{\frac{1}{2}} - \theta_i^2 - 2\delta \quad (3.19)$$

The *transmission coefficient* T can be simply obtained by

$$T = 1 - R \quad (3.20)$$

3.1.1 Total reflection

Let us consider a plane, monochromatic wave propagating in medium 1, impinging under the glancing angle θ_1^i on a polished surface of a homogeneous, isotropic medium 2 (Figure 3.2).

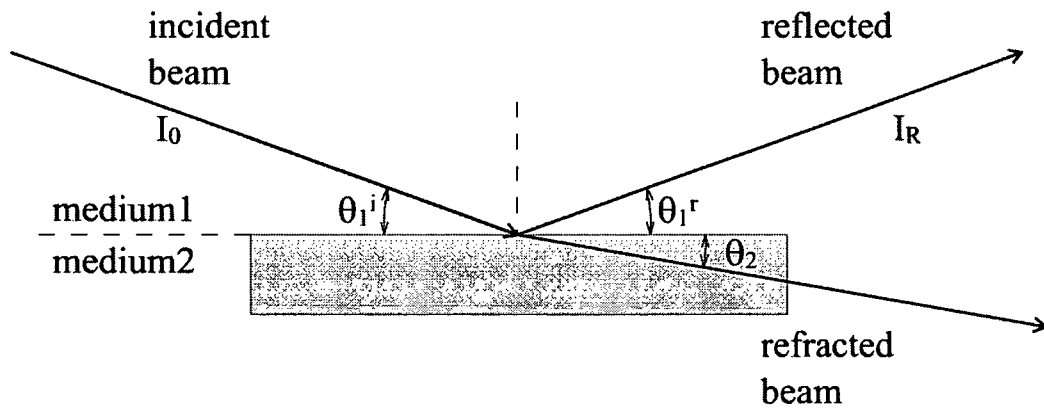


Figure 3.2: Schematic representation of Snell's law for the X-ray region

Assuming medium 1 to be vacuum and using the complex form of the refractive index described in equation (3.6) Snell's law writes as

$$\frac{\cos \theta_1}{\cos \theta_2} = 1 - \delta_2 - i\beta_2 \quad (3.21)$$

If the glancing angle of incidence θ_1^i is smaller than the *critical angle* θ_c – the angle for which $\theta_2 = 0$ – total reflection occurs.

For hard X-rays the imaginary part of the refractive index can be ignored (β is about 2 orders of magnitude smaller than δ) and the θ_c is described by

$$\cos \theta_c = 1 - \delta \quad (3.22)$$

The approximation for small angles leads to

$$\theta_c = \sqrt{2\delta} \propto \frac{1}{E} \quad (3.23)$$

where E is the photon energy. Assuming that there is only one free electron per atom, the critical angle can be expressed as a function of the *atomic number* Z

$$\theta_c = 28.8 \cdot \frac{1}{E} \sqrt{\frac{Z\rho}{A}} \quad (3.24)$$

where θ_c is in minutes of arc, ρ is the density of the material in $[\text{g}/\text{cm}^3]$ and A the atomic mass.

3.2 Reflective X-ray optics

In general a distinction can be drawn between two types of reflective optics for X-rays, total reflecting mirror optics and Bragg reflecting crystals. The main difference between both types of optics are their band-pass properties. Whereas total reflecting optics have a broad band-pass and are therefore able to focus over a large energy range, Bragg reflecting crystals only focus a small fraction of the radiation continuum. The disadvantage of grazing incident optics is the small acceptance angle due to the sharp drop in reflectivity at the critical angle. To compensate for this effect and to extend the reflectivity beyond the critical angle multilayer optics have been developed, which can be considered as hybrids between total reflecting optics and Bragg reflecting optics.

3.2.1 Multilayer optics

Multilayers consist of alternate thin layers of materials with periodically varying refractive index. When such optics are illuminated by a parallel beam of wavelength λ the reflectivity changes with the glancing angle of incidence θ and reaches a maximum at an angle given by Bragg's law

$$n\lambda = 2d \sin \theta \quad (3.25)$$

where d is the period of the multilayer (sum of the thickness of the two layers). Typically multilayers consist of about 100 layer pairs, where one is a strong scattering material and the other one is a low absorption spacer (e.g. Mo/Si, Rh/C, Ni/C). The d spacing is in the range of 15 Å to several hundred Å. The reflectivity of the multilayer depends on the roughness of the layer interfaces and becomes more critical if the d spacing is smaller.

Since these optics can be regarded as artificial crystals, they are widely used as monochromators at many synchrotron facilities. Compared to standard crystals, which have a rather high energy resolution, multilayers have a relatively large band-pass $\Delta E/E$ up to 10%. As such they allow to produce quasi-monochromatic beams from a continuous X-ray spectrum without dramatic losses in the number of photons, as caused by crystal monochromators.

By using specially bent or graded multilayers it is possible to produce monochromatic, focused X-ray beams with one optical system.

3.2.2 Mirror optics

First experiments on producing focused X-ray beams by total reflection from the surface of curved mirrors were performed by Kirkpatrick and Baez in the late 1940s [15]. In principle the easiest approach to get a small beam spot is to reflect the X-ray beam at the inside of an ellipsoidal surface. Placing a source at the one focal point of the ellipsoid a point to point focusing will occur, producing a reduced image of the source at the second focal point of the ellipsoid. Due to the fact that only radiation at grazing incidence is totally reflected, the surface has to be highly asymmetric to have a reasonable reflectivity. Since it is not easy to produce asymmetric optics with acceptable surface properties, compound systems such as the Kirkpatrick–Baez (K-B) geometry are used. It consists of two crossed spherical or cylindrical mirrors (Figure 3.3), which are more easy to fabricate. The inherent advantage of the K-B system is that aberrations introduced by the first mirror can, to some extent, be compensated by the second mirror.

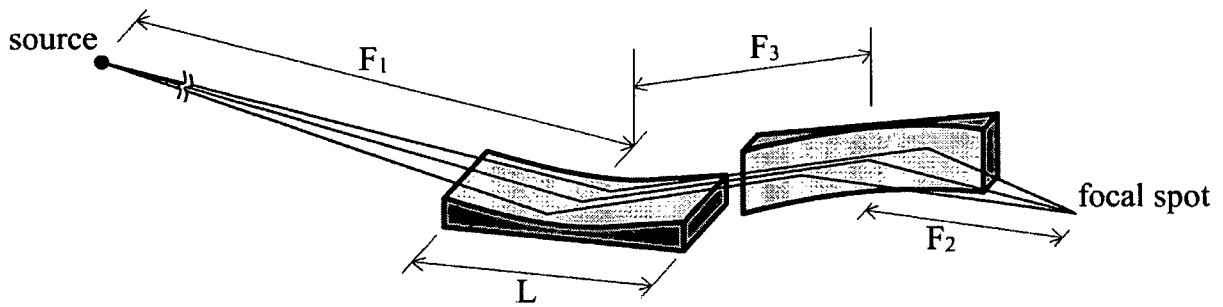


Figure 3.3: Scheme of a Kirkpatrick-Baez focusing system

3.3 Capillary optics

During the last decades capillary optics technology has become a powerful tool for optically controlling and focusing of X-rays [16-21]. Due to their relative simplicity in handling and their capacity of generating intense beams at the μm scale capillary optics are nowadays widely used in $\mu\text{-XRF}$ systems, working either with synchrotron radiation or laboratory sources. Although based on the same optical effect, capillary optics can be divided in two groups, namely monocapillary- and polycapillary optics.

3.3.1 Monocapillary lenses

When X-rays enter a glass capillary with a smooth inner surface under a very small glancing angle, total reflection at the walls occurs. Thus X-rays propagate inside the capillary with almost no loss in intensity. Comparing the intensity of X-rays exiting from a capillary with the intensity obtained after a non reflecting device (e.g. collimator) the intensity gain of the capillary can be determined. For a straight capillary the *intensity gain factor* I_g can be defined as (Figure 3.4)

$$I_g = \frac{\Delta\Omega_{\text{eff}}}{\Delta\Omega} \quad (3.26)$$

where $\Delta\Omega_{\text{eff}}$ is the effective solid angle seen by the X-ray source (corresponding to the critical angle θ_c) and $\Delta\Omega$ the solid angle when no reflection occurs (defined by the length of the capillary).

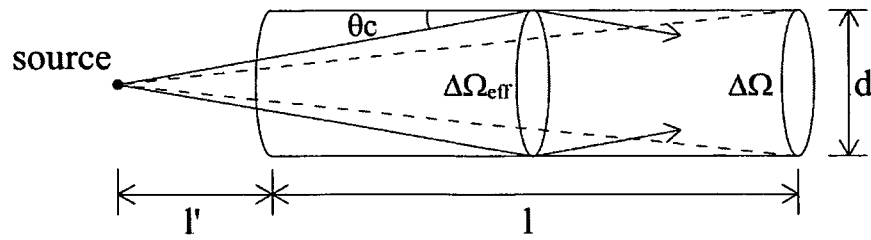


Figure 3.4: Definition of the capillary gain factor I_g

The gain factor shows the behavior of a low-pass filter where $\Delta\Omega_{\text{eff}}$ is proportional to $1/E^2$ as the critical angle increases for higher energies (Figure 3.5).

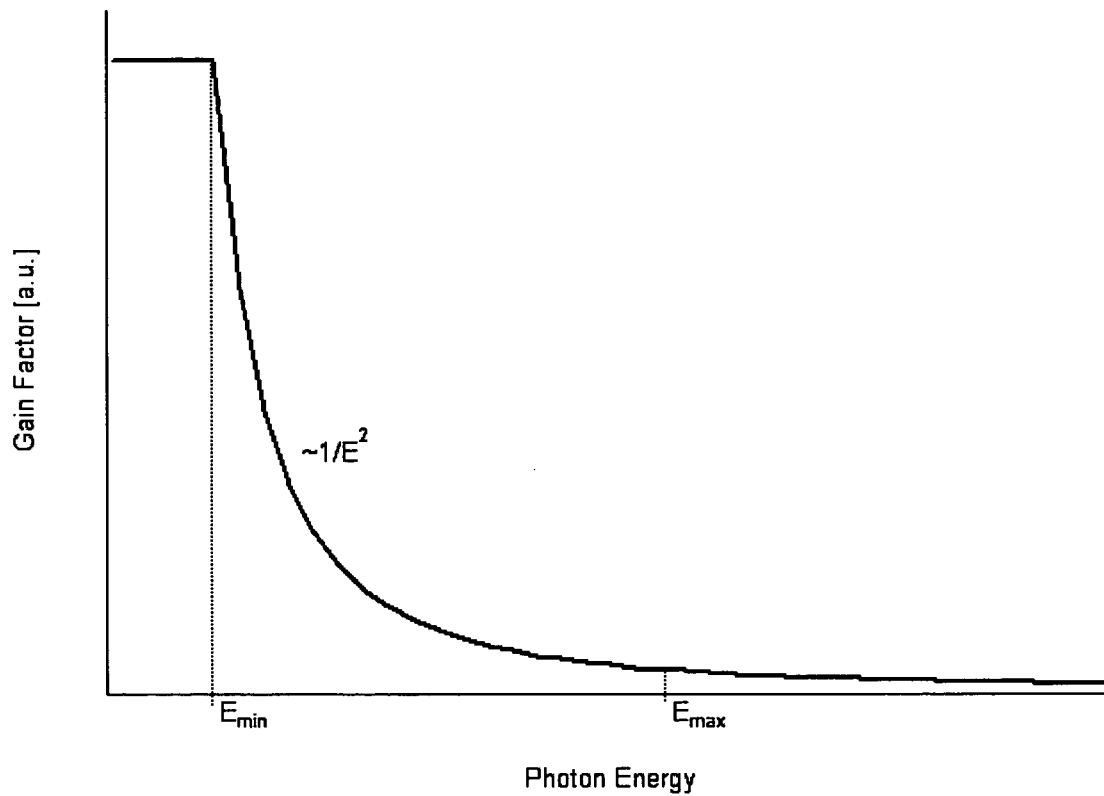


Figure 3.5: Gain factor for a straight capillary; absorption neglected

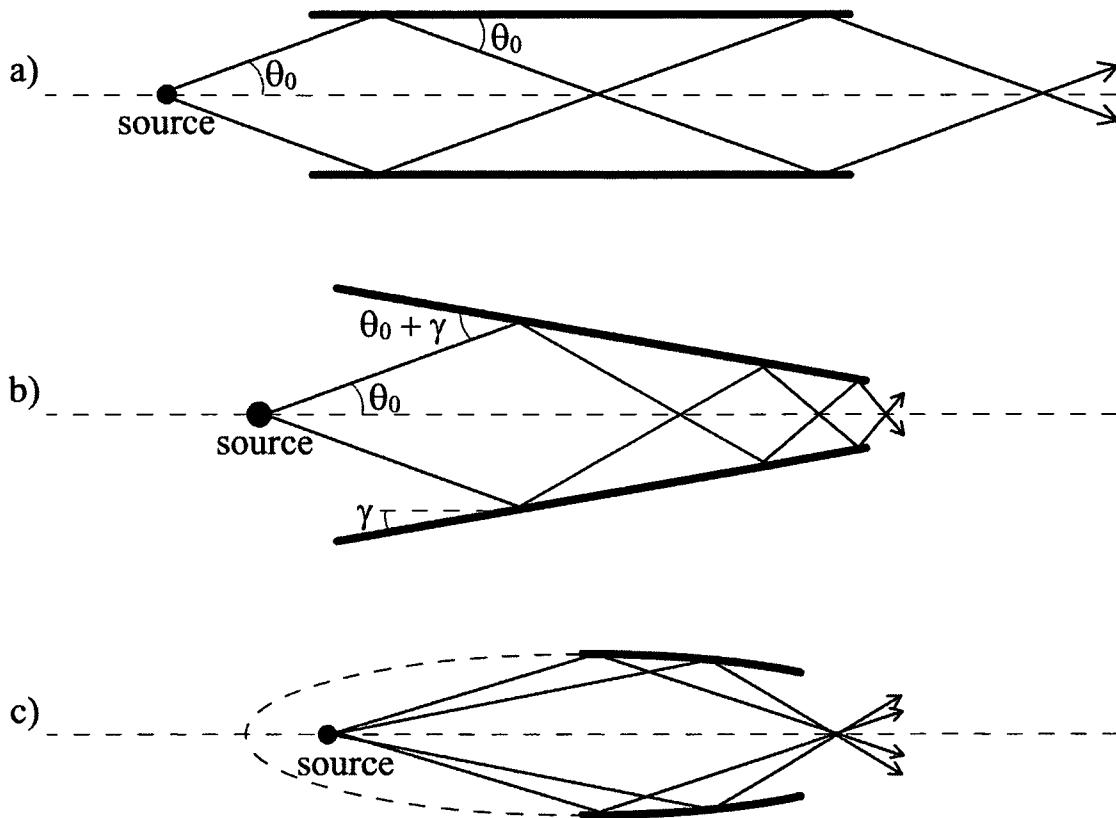


Figure 3.6: Principle of X-ray transport in straight (a), conical (b) and ellipsoidal capillaries

Three major designs of monocabillaries are shown in Figure 3.6.

Straight capillaries (Figure 3.6 (a)) have no focusing attributes, but can be regarded as waveguides working in the X-ray regime. If the angle of incidence is smaller than the critical angle, X-rays from a close source will be collected and transported towards the sample. Therefore the $1/r^2$ loss from isotropic point sources will be eliminated.

Conical capillaries (Figure 3.6 (b)) work similar to straight capillaries, but besides efficiently transporting, they also “squeeze” the X-rays to smaller spot sizes at the exit end. However, for each reflection the glancing angle increases with two times the cone angle γ and the reflectivity drops rapidly if the critical angle is exceeded. The output spectrum for conical capillaries has a more complicated band-pass structure compared to straight capillaries. After the focus of the capillary the beam divergence is in the order of the critical angle.

A reduction of the beam divergence is accomplished with ellipsoidal capillaries (Figure 3.6 (c)). Due to the imaging properties of an ellipsoid, any point source placed at the first focal point of the capillary will be focused to the second one. If the source is out of the optical axis the propagation of the X-rays is comparable to the one in conical capillaries.

3.3.2 Polycapillary optics

Polycapillary X-ray optics consist of an array of monocabillaries aiming at the same point. As such, these lenses are able to collect X-rays from a source within a large solid angle and redirect them to the focal plane by external total reflection. The efficiency of the device is strongly dependent on the number of capillaries used, the transmission properties and the wall thickness of the individual capillaries. Thus the use of a large number of thin walled capillaries leads to improved efficiencies.

Today a new generation of polycapillary optics, referred as monolithic polycapillary optics, exists. With this type of optics many capillaries are closely packed, fused together and brought to the desired shape by a heating process. The cross-section of the individual channels change over the length of the optics in such a way, that all channels point to a common spot—the focus of the optics, resulting in an improvement of the transmission efficiency.

Nowadays two types of optics, referred as point-to-point lenses (Figure 3.7, (a)) and parallel-to-point lenses (Figure 3.7, (b)), are available. While point-to-point lenses are mainly used for laboratory applications, to produce a small diameter X-ray beam from a divergent source at the sample surface, parallel-to-point lenses are widely installed at synchrotron facilities to focus the almost parallel beam.

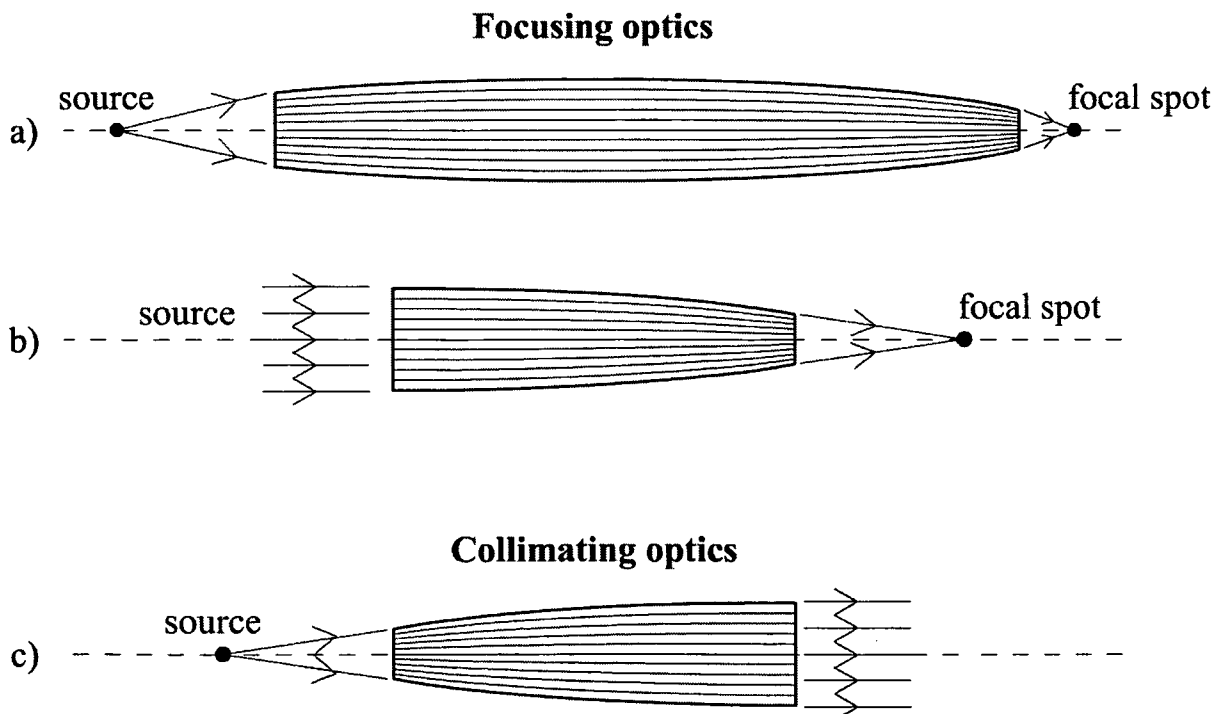


Figure 3.7: Polycapillary optics for focusing (a,b) and collimating (c) X-ray beams

By using the parallel-to-point lens in the other direction one can get a parallel beam from a divergent source (Figure 3.7 (c)).

For all focusing polycapillary devices the flux density is much better than for monocapillary optics, and collection angles up to 25° can be reached. Since the output focal distance has to be large ($\sim 1\text{cm}$) in order to minimize the bending of the capillaries, beam sizes below $30\text{-}40\mu\text{m}$ are difficult to achieve.

3.4 Refractive X-ray optics

X-ray refraction exploits the fact that the real part of the complex refractive index from equation (3.6)

$$\tilde{n} = 1 - \delta - i\beta \quad (3.27)$$

is less than unity in matter, while it equals 1 in vacuum or air. Since the refractive index is very small, X-ray focusing based on refraction has been considered not feasible in the past. Another argument against refractive X-ray optics is that the absorption (β in equation 3.27) is dominant in any material realistic for lens construction. Unlike focusing lenses for visible light X-ray refractive lenses have to have a concave shape, as the refractive index is less than unity.

3.4.1 Compound refractive lenses

Despite all difficulties mentioned above the first refractive lenses were fabricated in 1996 [22] by drilling a linear array of holes in a low-Z lens material such as Al (Figure 3.8 (b)). Another way of constructing compound refractive lenses is to stack half cylinders as shown in Figure 3.8 (a).

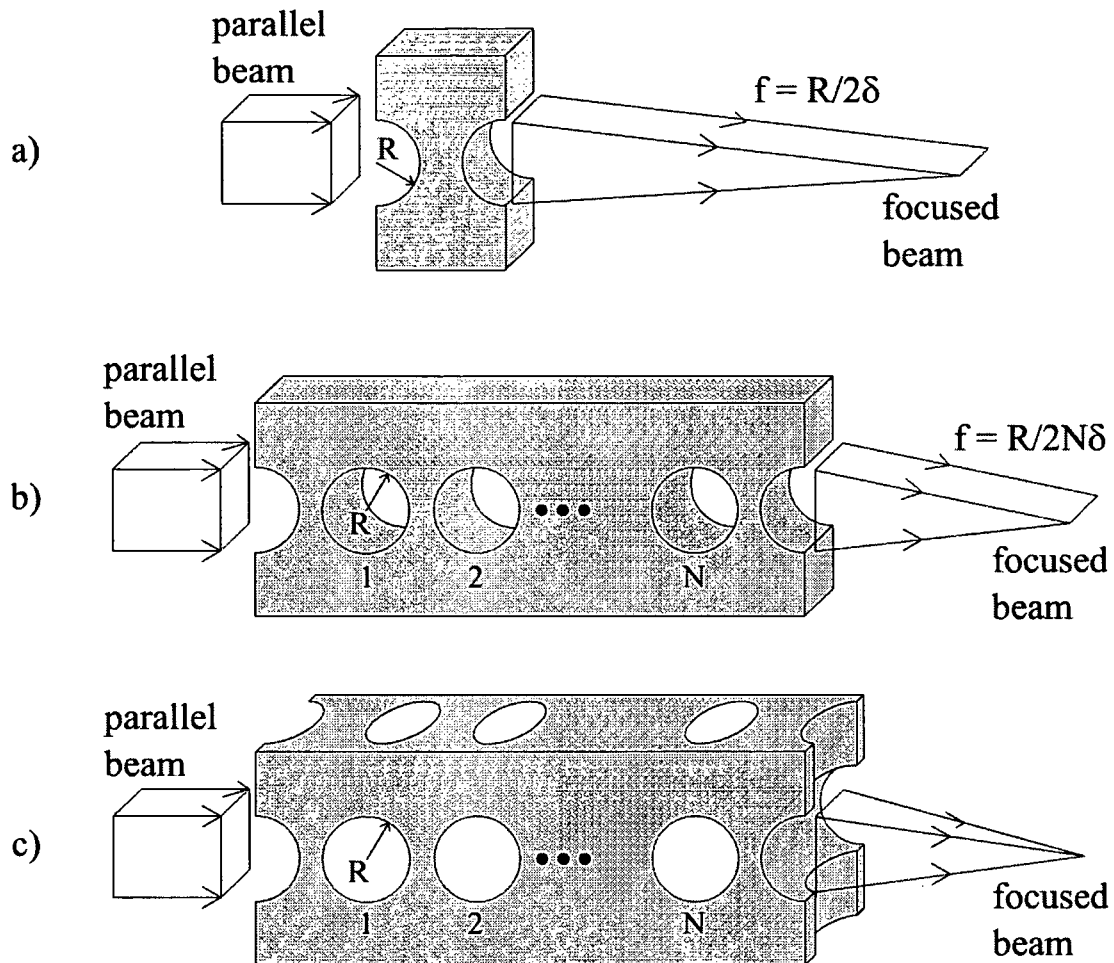


Figure 3.8: Sketches of compound refractive lens arrays for one-dimensional (a,b) and two-dimensional (c) focusing

A single lens element (Figure 3.8 (a)) will focus a parallel beam in a line (one dimensional focusing) at a focal distance f given by

$$f = \frac{R}{2\delta} \quad (3.28)$$

where R is the radius of the cylinder. The major disadvantage of such devices is the long focal distance in the range of meters. For example, a spherical hole of radius $300\mu\text{m}$ in Al ($\delta = 2.8 \times 10^{-6}$) will focus an X-ray beam with an energy of 14 keV at a distance of 54m.

By producing a compound lens with an array of N holes (Figure 3.8 (b)) the focal line will appear at a distance N times shorter than the focal distance for a single hole.

$$f = \frac{R}{2N\delta} \quad (3.29)$$

For the example above the focal distance will reduce to 1.8m when using a lens setup with $N = 30$ holes.

For many applications a two-dimensional focusing (focusing to a point instead of a line) is desired. To reach this demands devices with a crossed hole geometry can be used (Figure 3.8 (c)).

Compound refractive lenses from Al are easily fabricated, but suffer from high absorption and scattering in the lenses. To overcome the problem of absorption, lenses from different low-Z materials, such as beryllium [23-26], silicon [27-29] and organic compounds [23, 24, 30-35], have been tested experimentally. Improvements in lens fabrication leading to further reduction of X-ray absorption have recently been made by creating kinoform lenses in polymer materials by X-ray lithography [36].

4 Microscopic X-ray Fluorescence Analysis

Although X-ray fluorescence analysis (XRF) is a well established method for qualitative and quantitative multi element analysis of bulk samples [37], it has not been as widely used at the microscopic level as particle induced microprobe techniques in the past. However, even with poor optical efficiency, X-ray microbeams offer several advantages for analysis compared to other micro-analytical techniques (Table 4.1).

Technique	Exciting beam	Primary energy [keV]	Beam size [μm]	Penetration depth [μm]	MDL [ppm]	Destructive
EPXMA	e^-	5-50	< 0.1	1 – 10	1000	no
μ -PIXE	p^+	$2-3 \times 10^3$	0.3 – 5	5 – 100	1 – 100	yes/no
μ -SRXRF	X-ray	2-80	0.7 – 10	100 – 1000	0.1 – 100	no
SIMS	M^+, N^-	10-30	0.5 – 10	< 0.1	< 1	yes
LA-ICP-MS	photon		20	10	0.5 – 5	yes

Table 4.1: Comparison of analytical characteristics of some micro-analytical techniques. Electron probe X-ray micro-analysis (EPXMA), proton induced X-ray emission (μ -PIXE), synchrotron radiation induced X-ray fluorescence analysis (μ -SRXRF), secondary ion mass spectrometry (SIMS), laser ablation inductively coupled plasma mass spectrometry (LA-ICP-MS). adapted from [38]

Looking at their analytical characteristics, such as spatial resolution, detectable element range, minimum detection limits (MDL), information depth and consumptiveness, all the techniques listed in Table 4.1 have strong and weak points. Therefore the decision whether the one or the other is better is strongly dependent on the application and the expected results. Concerning μ -(SR)XRF the non destructive, and in principle quantitative character together with a sensitivity at the ppm level might be mentioned as the advantageous characteristics of the method. For some applications the moderately good resolution and the relatively large penetration depth may be seen as a limiting factor of the technique. However, the latter attribute can be exploited for three-dimensional analysis of the sample, which might be beneficial for some applications.

4.1 Introduction

Since microscopic X-ray fluorescence analysis (μ -XRF) is based on the same physical effects, it can be understood as a micro-analytical variant of bulk XRF with different measuring strategy. In comparison to bulk analysis, where an X-ray beam of rather large diameter (in the mm range) is used to analyze a homogeneous (or previously homogenized) sample, only a (microscopically) small area (in the μm range) of a larger sample is irradiated (Figure 4.1).

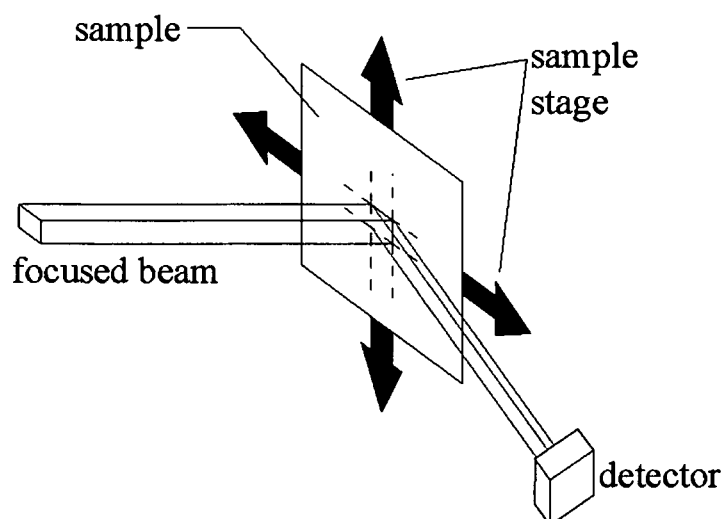


Figure 4.1: Typical measurement geometry for μ -XRF

By moving the specimen relatively to a focused incident beam and collecting the fluorescence photons from each irradiated spot information on the local composition of the sample can be obtained. By running measurements in different scanning modes either spot analyses (single spot measurements), line analyses (line-scans) or elemental imaging (area-scans) can be performed.

The difficulties in using μ -XRF as an analytical tool have to be seen in the production of focused X-ray beams of sufficient intensities to allow sensitive microanalysis. Therefore μ -XRF systems have only recently appeared and are strongly coupled to the development of sufficient X-ray focusing optics (see chapter 3).

4.2 Instrumentation

A typical μ -XRF instrument is illustrated in Figure 4.2. Basically it consists of an X-ray source, some kind of focusing device, a moveable sample holder (either manually or motor controlled), a detection system and an optical microscope with a CCD camera attached to it.

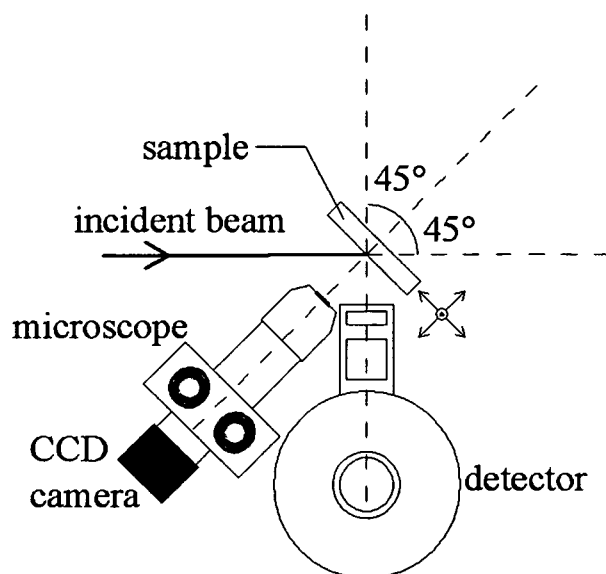


Figure 4.2: Schematic view of a typical μ -XRF setup

The first two components (X-ray sources and X-ray optics) define the spectral properties of the incident beam and are explained in detail in chapter 6 and 3 respectively. Although X-rays can be more or less efficiently focused into microbeams, they can not be deflected like charged particle beams and scanning has to be performed by movement of the sample. Therefore the sample stage should allow for accurate remote movement of the sample relatively to the incoming beam. Typically the sample stage consists of three linear stages driven by computer-controlled stepper motors to perform all necessary movements for adjustment and XRF scanning. The minimum step size of the motors should be well below the minimum lateral resolution of the system defined by the spot size of the micro beam.

The optical microscope with the CCD camera is utilized to monitor the sample position. In order to have the sample surface coincidence with the focal plane of the microscope the specimen has to be turned away (usually 45°) from the plane perpendicular to the incident beam. In place it should be mentioned, that with such geometries the measured fluorescence intensities represent the projection of the elemental distribution in the sample rather than the distribution itself, which might at least for relatively thick samples lead to problems in the interpretation of the recorded data.

4.3 Data evaluation and image processing

In principle one can distinguish between two different types of data storage and visualization of μ -XRF measurements. The simplest approach is to store the data from specific regions of interest (ROI) predefined from an XRF spectrum representative for the sample, for each pixel and display them versus the coordinates of the stepper motors using a sufficient color code. Although from the viewpoint of data processing and storage this method is very convenient, it might introduce additional uncertainties and errors for some applications. Especially when using polychromatic excitation or measuring samples with a strongly scattering matrix the radiation background in the spectrum can not be neglected and the sum of counts in the ROI is an uncertain number. With this measuring mode also the spectrum from each pixel is lost and can not be used for further evaluation.

The second possibility is to store for each pixel the whole fluorescence spectrum which is used for data evaluation after the measurements. This allows for the use of proper background correction and peak deconvolution procedures (see paragraph 2.4). Although in this case the data evaluation and image generation might become tedious and requires large data storage capacities it has to be preferred over the first approach.

Using either the one or the other approach elemental maps (in case of area scanning) are reconstructed for each element by displaying the fluorescence intensities for each pixels and storing these data as image files. For elements with high count rates (major components of the specimen) elemental maps can be produced with adequate statistics and inhomogeneities for those elements can be easily identified. For trace elements, however, the statistics is usually poor and inhomogeneities are difficult to identify. In such cases the correlation of the measured intensity maps with the optical micrograph can help a lot for the interpretation of the data.

A general problem when working with imaging techniques is the question for the sufficient color code. Figure 4.3 shows one of the first X-ray radiographs made by W.C. Roentgen in three different color codes. The data has been converted to 8-bit integers and is displayed as a grayscale image (a), in the “fire” code (b) and in the “spectrum” code (c).

Comparing the three images from Figure 4.3 it can be seen, that different color codes might yield different information, which is mainly due to the sensitivity of the human eye.

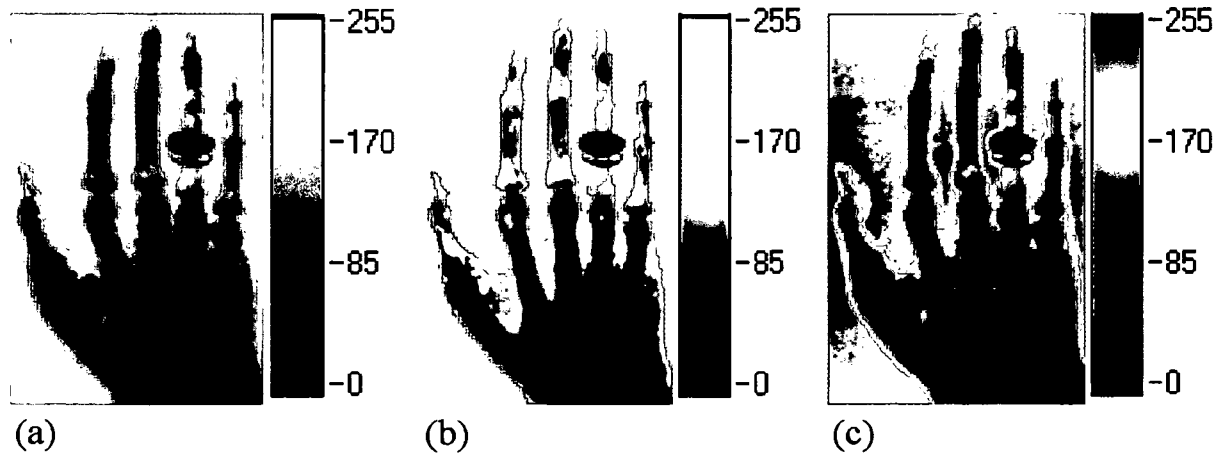


Figure 4.3: X-ray radiography in three different color codes. The data has been converted to 8-bit integers and is displayed in grayscale (a), fire code (b) and in the spectrum code (c)

Comparing the area between the thumb and the forefinger, or the forefinger itself, one can see differences in the intensities which can be seen either in the one or in the other illustration. In general the grayscale image seems to be the smoothest of the three color codes used, but for some purposes it might also be helpful to use the colored images.

4.4 Quantification

X-Ray fluorescence analysis is known for its ability to yield reliable quantitative results and has therefore become a well established method for routine analysis in many cases. When performing quantitative XRF the main task is to convert measured line intensities to the concentration of the analyte. As derived in paragraph 2.3 for a homogeneous specimen with a flat surface and monochromatic parallel excitation this can be done by solving

$$\begin{aligned}
 I_{\xi k} &= I_0 G S_{\xi k} W_{\xi} \rho_s \int_0^t \exp \left[- \left(\frac{\mu_{s,E_0}}{\sin \phi_i} + \frac{\mu_{s,E_{\xi k}}}{\sin \phi_f} \right) z \right] dz \\
 &= I_0 G S_{\xi k} W_{\xi} \rho_s \frac{1 - \exp \left[- \left(\frac{\mu_{s,E_0}}{\sin \phi_i} + \frac{\mu_{s,E_{\xi k}}}{\sin \phi_f} \right) t \right]}{\left(\frac{\mu_{s,E_0}}{\sin \phi_i} + \frac{\mu_{s,E_{\xi k}}}{\sin \phi_f} \right)} \quad (4.1)
 \end{aligned}$$

$I_{\xi k}$ line intensity for the element ξ originated by the transmission of an electron between the shells $j \rightarrow k$.

μ_{s,E_0}	linear absorption coefficient of the sample for the energy E_0
W_ξ	weight fraction of the element ξ
$S_{\xi k}$	sensitivity factor of the system for the element ξ (see equation 2.3)
ρ_s	density of the sample
G	generic geometry factor including detector size and distance, source size and distance
ϕ_i	incident angle of the primary photons
ϕ_f	detection angle of the fluorescence photons
$\mu_{s,E_{\xi k}}$	linear absorption coefficient of the sample for the energy $E_{\xi k}$
t	sample thickness

for the weight fraction W_ξ of the Element ξ . If the sample is a mixture of several chemical elements the mass attenuation coefficient has to be evaluated from the coefficients μ_ξ for the constituents and the weight fraction W_ξ by

$$\mu_{sample} = \sum_{\xi} W_{\xi} \mu_{\xi} \quad (4.2)$$

Since this value (and therefore also the weight fraction) appears in the index of the exponential function in equation (4.1) the solving for W_ξ has to be done iteratively.

After the publication of the basic relationship for quantification in XRF [39] in 1955 the method was further developed by implementing secondary and higher order effects [40-42], still assuming homogeneous specimen.

In the last few years many efforts have been made to account for irregular sample shapes and particle size effects [43], which is on the one hand very important for micro XRF, but on the other hand still the most difficult part to treat in fundamental parameter method because of the enormous variability of particles in the sample.

Besides the mentioned effects some further problems especially linked to micro XRF have to be considered and are discussed in the next paragraphs.

4.4.1 Information depth

As seen from table 4.1 the penetration depth for X-rays in most materials is much larger than it is for charged particles. While for charged electrons and protons the penetration depth is defined by primary projectiles this is not the case for X-rays. In XRF the fluorescence radiation is usually more strongly absorbed than the primary radiation, which results in an energy dependence of the information depth. Therefore the information depth is different for each element and is not determined by the primary- but by the characteristic radiation of the elements and the matrix composition of the sample.

The information depth d_i for an element i (with characteristic radiation energy E_i) is defined as the distance measured perpendicular to the sample surface at which the intensity of the emitted fluorescence line is reduced by a factor of e . It can therefore be derived from Beer-Lambert's law to be

$$d_i(E_i) = \frac{1}{\mu(E_i)\rho} \quad (4.3)$$

where $\mu(E_i)$ is the mass attenuation coefficient for the energy E_i and ρ the density of the sample.

The consequences of the energy dependence of the information depth especially if the sample is a composite of low Z and high Z materials are illustrated in Figure 4.4.

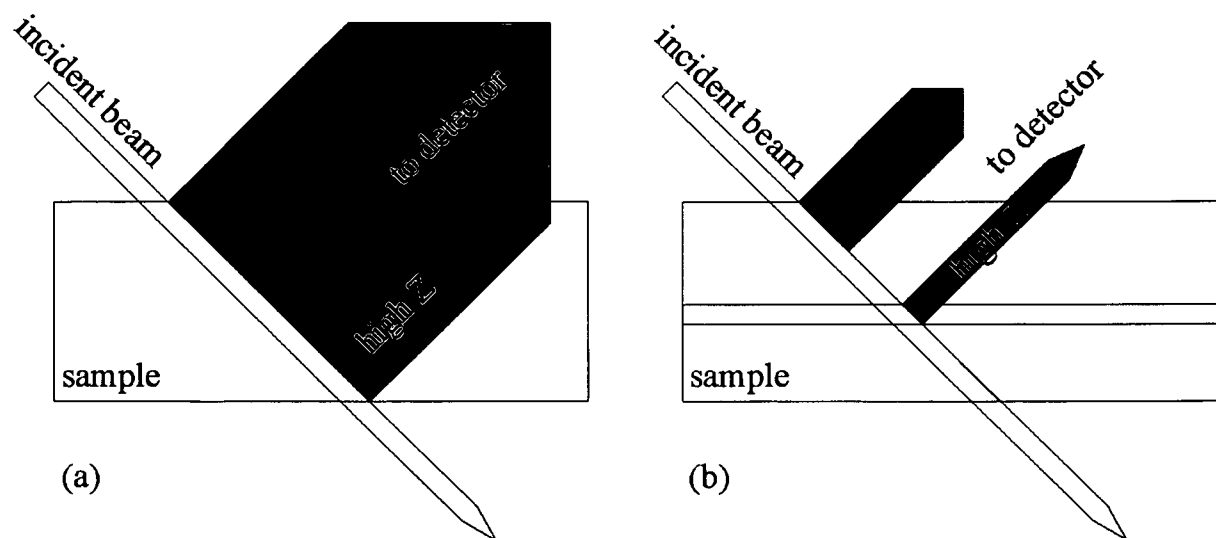


Figure 4.4: Different information depth for low Z and high Z elements in case of a homogeneous (a) and an inhomogeneous sample (b)

For the illustration (in scale) an incident micro beam of $20\mu\text{m}$ diameter was chosen, while the sample thickness was set to $200\mu\text{m}$. Assuming that the optical microscope used for controlling the sample position is focused on the point of the sample surface where the X-ray beam impinges, in both cases (homogeneous (a) and inhomogeneous sample (b)) the relatively large sample thickness results in a degraded lateral resolution and in a distortion between the intensity maps of the low Z and the high Z element. While the fluorescence radiation from the low Z element will escape only from the first few μm , the characteristic lines of the high Z element produced over the whole sample thickness will be detected. Therefore, when comparing the optical micrograph of the analyzed area of the specimen with the elemental map of the low Z material the images will fit better than compared with the map of the high Z element from the sample.

Besides the loss in lateral resolution, also the quantification in such cases becomes very complicated. In the case of homogeneous samples (Figure 4.4 (a)) the concepts of the fundamental parameter method (equation 4.1) can be directly applied and deliver reasonable results. Even for samples with relatively simple heterogeneity, such as layered structures, the fundamental parameter method with some modification is applicable. Since in this case the total attenuation along the path of the impinging and exciting X-rays has to be calculated as the line integral of the linear absorption coefficient, the expressions used to describe the detected fluorescence intensities become fairly complex. In the general case, when analyzing samples with three-dimensional heterogeneity a relation between the measured fluorescence intensity of element I and the sample structure has to be established. To obtain the magnitude in the exponential function in equation 4.1 a numerical integration of the sample concentration and absorption characteristics over the interaction volume of the primary and fluorescent photons has to be performed. The result of these calculations is strongly dependent on the path of the X-rays through the various phases of the sample, and small variations lead to large fluctuations in the integrated absorption coefficient. In other words, to correct the fluorescence intensities (especially in the case of strong self absorption) for samples with general heterogeneities the matrix composition and the distribution of various elements has to be known with high accuracy, which is very hard to be accomplished in particular for natural samples, such as bone.

4.4.2 Monte Carlo Simulations

As an alternative to the fundamental parameter method Monte Carlo (MC) simulations might be used for quantification in micro XRF. Generally the radiation (primary and fluorescence) is described by trajectories and probability density functions. The interaction of the X-rays with the atoms are considered as stochastic processes simulated by computer-generated random numbers, following the probability density functions. As the random numbers represent all relevant photon-matter interactions during the measurement, a series of trajectory histories describe the photon detection after all physical processes inside the sample. With the MC method it is possible to describe the full spectral response [44, 45] for the used XRF spectrometer taking the photoelectric effect, Rayleigh- and Compton scattering [46] as well as polarization [47] into account.

The advantage of using MC simulation rather than more conventional approaches for quantification is that it is relatively easy to extend the code to further physical processes. For example, the contribution of scattered radiation [48, 49] can be implemented in the code and an extension to heterogeneous samples is possible [50-53]. Nevertheless a general calculation remains difficult also with MC methods. Also for a sample with a general heterogeneity it is not possible to derive the composition of the specimen from a set of μ -XRF measurements. With a MC program it is only possible to verify whether a hypothesis about the structure and composition of a particular sample is consistent with the experimental data that are obtained for it.

4.5 Confocal micro XRF

In the last few years the confocal setup has been suggested by several authors [54-56] as a variant of μ -XRF, and has been used in tabletop systems [57] as well as for synchrotron applications [58-61]. The principle of a typical confocal setup is shown in Figure 4.5.

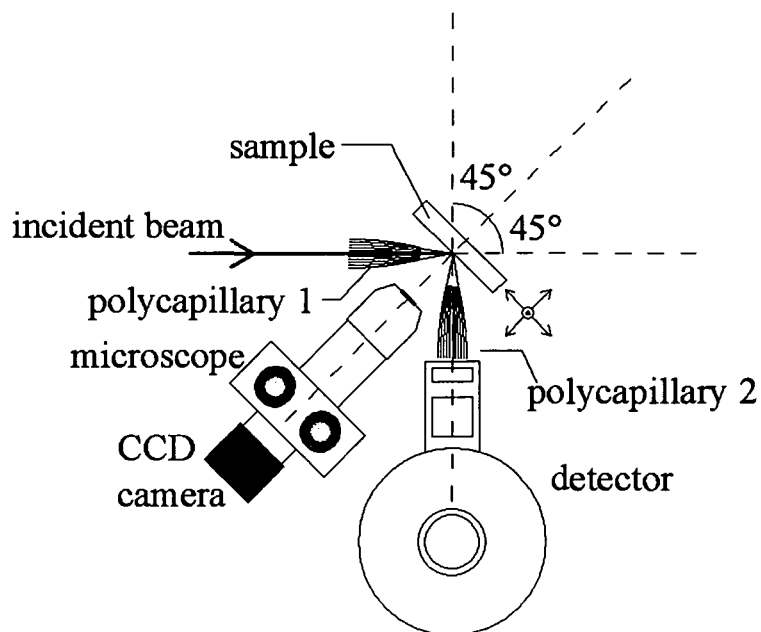


Figure 4.5: Scheme of a typical setup for confocal μ -XRF imaging

One X-ray optics, which could be a polycapillary lens or any other focusing device is used in the excitation channel to concentrate the primary radiation from an X-ray source onto the sample surface. A second optical device, typically a half lens is positioned between the sample and an energy dispersive detector. By overlapping the two focal spots of polycapillary 1 and polycapillary 2 a well defined micro-volume in the μm^3 can be achieved from which the fluorescence radiation is detected (Figure 4.6).

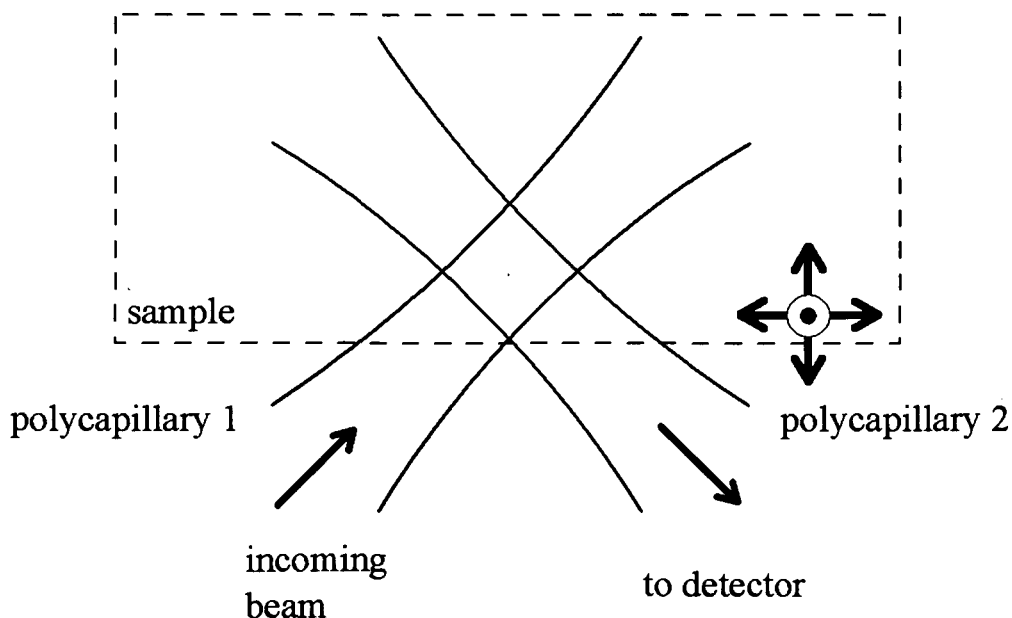


Figure 4.6: Micro-volume defined by the overlap of the focal spots of two X-ray optics

By moving the sample laterally and along the direction normal to its surface the detection-volume can be placed in almost any region of the sample. Thus it is possible to obtain the lateral distribution of the elements either in a given depth or in depth of the sample nondestructively. Furthermore, by performing a three-axis movement a full 3D image of the elemental distribution can be reconstructed which makes confocal μ -XRF an alternative to fluorescence tomography. Besides the capability of three-dimensional elemental imaging the confocal setup allows to eliminate the contribution of underlying inhomogeneities for thick samples as described in paragraph 4.4.1. Therefore in such cases the use of the second lens in front of the detector improves the resolution of the system and the uncertainties due to geometric effects are minimized.

4.5.1 Energy dependence of the detection volume

As described in detail in chapter 3 the focusing of X-rays inside of a polycapillary lens is based on the effect of total external reflection of the photons at the capillary walls. Therefore, due to the energy dependence of the critical angle (equation (3.24)) photons of higher energy are more efficiently (to a smaller spot-size) focused than ones with lower energy [62]. The same holds for the acceptance of the second polycapillary in front of the detector, where the angle of the opening cone is inversely proportional to the characteristic energy of the detected element. Therefore, the size of the detection volume is dependent on the energy of the incident (monochromatic) radiation E_0 and the energy of the fluorescence photons E_i and can be expressed as

$$FWHM_{vol}^2(E_0, E_i) = FWHM_1^2(E_0) + FWHM_2^2(E_i) \quad (4.4)$$

where $FWHM_1$ and $FWHM_2$ are the full width at half maximum of the gaussian curves obtained when wire scanning the focal spots of the capillaries (see Figure 4.7).

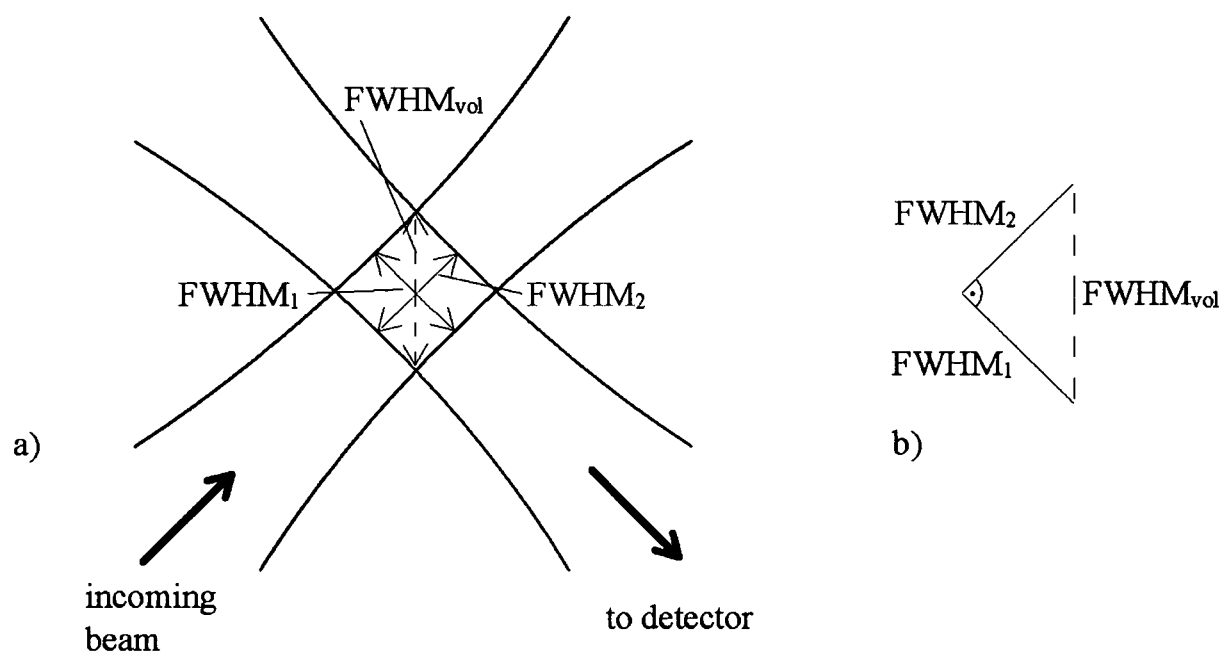


Figure 4.7: Scheme of the intersection of the beam cones from two polycapillary lenses

As an example experimental data on the energy dependence of the detection volume for $E_0=21\text{keV}$ is presented in Table 4.2 (data adopted from [63]).

Element	Char. energy [keV]	FWHM_{vol} [μm]
Ti	4.5	39
Cr	5.4	37
Mn	5.9	35
Fe	6.4	32
Ni	7.5	30
Zn	8.6	26
Zr	15.8	20

Table 4.2: Energy dependence of the sampling volume for a confocal setup at HASYLAB, beamline L obtain by scanning of thin foils at incident energy $E_0=21\text{keV}$. Data adopted from [63]

5 Micro Tomography

X-ray tomography is based on the idea of recording photons after interaction of a primary beam with the sample (transmitted-, scattered- or fluorescence photons) under various angles and subsequent (computer-assisted) decomposition of the information overlay.

In this work the concepts of absorption- and emission tomography, as well as a combination of both methods were used. Since the basic mathematical algorithms are the same for both modes of tomography, the following paragraphs on the fundamentals of image reconstruction will only describe the absorption case. The chapter has been written following the book of Kak & Slaney [64] and the script of N. Gurker [65].

5.1 Line Integrals and Projections

Let $f(x,y)$ be the two-dimensional object function (e.g. the distribution of the linear X-ray absorption coefficient) of the object of interest, $S(x,y)$ the coordinate system where the object rests and $S'(s,u)$ the system rotated with the direction of projection θ (Figure 5.1). The coordinate transformation between the two systems S, S' is given by

$$\begin{aligned} \vec{e}_s &= (\cos \theta, \sin \theta) & s &= x \cos \theta + y \sin \theta & x &= s \cos \theta - u \sin \theta \\ \vec{e}_u &= (-\sin \theta, \cos \theta) & u &= -x \sin \theta + y \cos \theta & y &= s \sin \theta + u \cos \theta \end{aligned} \quad (5.1)$$

and the line integral L_g of $f(x,y)$ along g can be written in parameterized form as

$$L_g(s, \theta) = \int_{-\infty}^{\infty} f(x, y) du = \int_{-\infty}^{\infty} f(s\vec{e}_s + u\vec{e}_u) du = \int_{-\infty}^{\infty} f(s \cos \theta - u \sin \theta, s \sin \theta + u \cos \theta) du \quad (5.2)$$

By performing the above integration the line information on the function $f(x,y)$ in the space domain is transformed to a point information in the so called Radon space (Figure 5.1 b). Calculating the line integrals for a given set of points for a fixed projection angle θ the so called *projection* $P_\theta(s)$ is obtained (one-dimensional function $L_g(s, \theta)$).

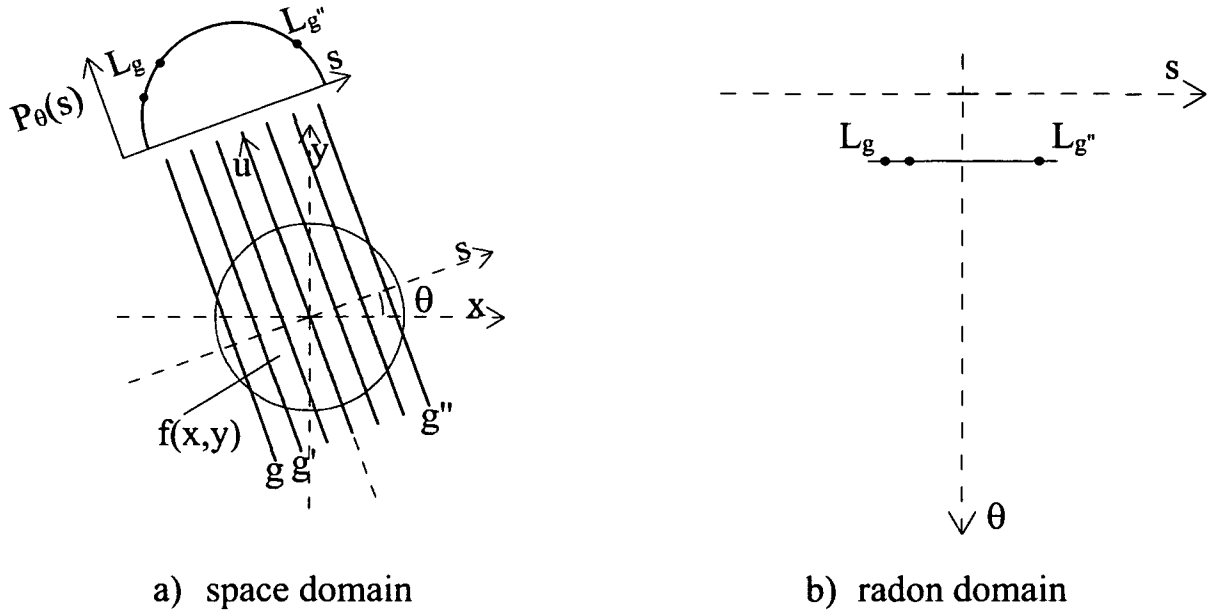


Figure 5.1: Transformation between the space (a) and the radon (b) domain. The Projection $P_\theta(s)$ for a fixed angle θ appears as a straight line in the Radon space

Introducing the *projection operator* R (Radon operator) one can describe the projection process in a more formal way

$$Rf(x, y) = P_\theta(s) \quad (5.3)$$

and the reconstruction problem can be written as

$$R^{-1}P(\theta, s) = R^{-1}Rf(x, y) = f(x, y) \quad (5.4)$$

where R^{-1} is the inverse Radon operator.

As an example the transformation of a simplified object function $f(x, y) = f_0 \delta(x-x_0)\delta(y-y_0)$ i.e. one point $P_0 = (x_0, y_0)$ is calculated. From the geometry displayed in Figure 5.2 one can see:

$$\begin{aligned} Rf_0 \delta(x-x_0) \delta(y-y_0) &= P(\theta, s) = f_0 \delta(s - r_0 \cos(\phi - \theta)) = \\ &= f_0 \delta(s - \sqrt{x_0^2 + y_0^2} \cos(a \tan(\frac{y_0}{x_0}) - \theta)) \end{aligned} \quad (5.5)$$

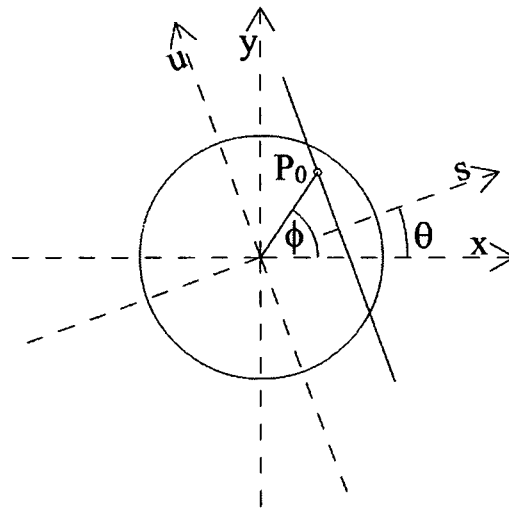


Figure 5.2: Basic geometry for the transformation of an object function $f(x,y)$ to the Radon space

The transformation from equation 5.5 is plotted for two points (P_1 , P_2) of the object in Figure 5.3. Each single point in the space domain viewed at different angles $0 \leq \theta \leq \pi$ is represented by a sinusoidal curve in the radon domain (sinogram).

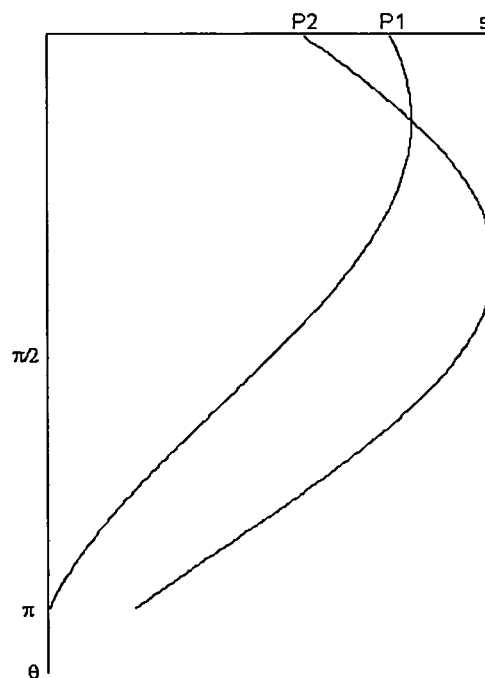


Figure 5.3: Example for the transformation of a simplified object function (2 object points). Each point is represented by an individual sinusoidal curve in the radon domain (basic sinogram)

5.2 Reconstruction Algorithm

In this paragraph the mathematical basis of tomography will be discussed. The Fourier Slice Theorem, which can be seen as the key to tomographic imaging as well as the concept of (filtered) backprojection will be developed. Since in this work only data from parallel beam projection was used, the algorithms for other beam geometries are left out.

5.2.1 Fourier Slice Theorem

Let $F(s_x, s_y)$ be the two-dimensional Fourier transform of the object function $f(x, y)$ defined by

$$F(s_x, s_y) = \int_{-\infty}^{\infty} \int_{-\infty}^{\infty} f(x, y) \exp[-i2\pi(s_x x + s_y y)] dx dy \quad (5.6)$$

According to equation (5.2) a projection in the (s, u) coordinate system along lines of constant s is written as

$$P_{\theta}(s) = \int_{-\infty}^{\infty} f(s, u) du \quad (5.7)$$

and its Fourier Transform is given by

$$S_{\theta}(w) = \int_{-\infty}^{\infty} P_{\theta}(s) \exp[-i2\pi w s] ds \quad (5.8)$$

Substituting the definition of a projection (equation 5.7) into the above equation one finds

$$S_{\theta}(w) = \int_{-\infty}^{\infty} \int_{-\infty}^{\infty} [f(s, u) du] \exp[-i2\pi w s] ds \quad (5.9)$$

This result can be transformed into the (x, y) coordinate system using the relations from equation (5.1), the result being

$$S_{\theta}(w) = \int_{-\infty}^{\infty} \int_{-\infty}^{\infty} f(x, y) \exp[-i2\pi w(x \cos \theta + y \sin \theta)] dx dy \quad (5.10)$$

The right hand side of this equation represents the two-dimensional Fourier transform at a spatial frequency of ($s_x = w \cos\theta$, $s_y = w \sin\theta$) or

$$S_\theta(w) = F(w, \theta) = F(w \cos \theta, w \sin \theta) \quad (5.11)$$

The above equation is called *Fourier Slice Theorem* and is the essence of straight ray tomography. It is stated as:

The Fourier transform of a parallel projection of an image $f(x,y)$ taken at an angle θ gives a slice of the two-dimensional transform, $F(s_x, s_y)$, subtending an angle θ with the s_x -axis.

In other words, the Fourier transform of $P_\theta(s)$ gives the values of $F(s_x, s_y)$ along the straight line in Figure 5.4 (b).

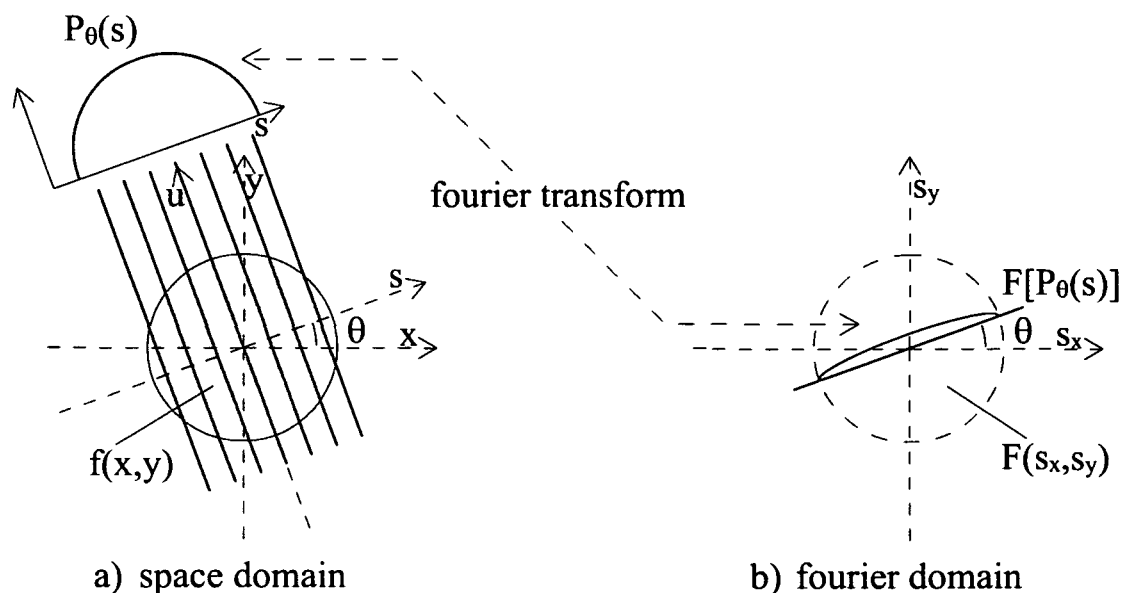


Figure 5.4: Graphical interpretation of the Fourier Slice Theorem

The Fourier Slice Theorem indicates that taking the projections of an object at different angles θ_k and Fourier transforming each of these, the values of $F(s_x, s_y)$ on radial lines as in Figure 5.4 can be determined. If an infinite number of projections are recorded, $F(s_x, s_y)$ will be known at all points of the (s_x, s_y) plane and the object function $f(x,y)$ can be recovered by the inverse Fourier transform.

$$f(x, y) = \int_{-\infty}^{\infty} \int_{-\infty}^{\infty} F(s_x, s_y) \exp[i2\pi(s_x x + s_y y)] ds_x ds_y \quad (5.12)$$

In practice only a finite number of projections of an object can be taken and $F(s_x, s_y)$ is only known along a finite number of lines as in Figure 5.5. To determine the values on a square grid from the data represented in Figure 5.5 some interpolation algorithms are commonly used. Since the density of the radial points becomes sparser for higher frequencies (farther away from the center) the error is greater as for the low frequency components of the image, leading to image degradations.

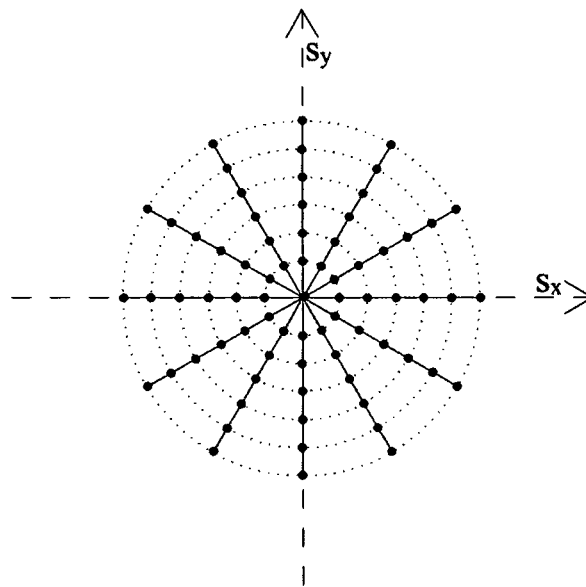


Figure 5.5: Finite number of projections in the Fourier space. Data points are more dense at the origin than for higher frequencies, which leads to image degradations

5.2.2 Direct Backprojection

While the Fourier Slice Theorem provides a simple conceptual model of tomography, practical implementations require a different approach.

Starting from a projection $P_\theta(s)$ at a given angle θ and introducing a *backprojection operator* B one can write the function f_θ^B obtained by the backprojection as

$$f_\theta^B = B_\theta P_\theta(s) \quad (5.13)$$

Superimposing the information of the projections at all angles $0 \leq \theta < \pi$ leads to

$$f^B(x, y) = \int_0^\pi P_\theta(x \cos \theta + y \sin \theta) d\theta = \int_0^\pi p(x \cos \theta + y \sin \theta, \theta) d\theta = BP(s, \theta) \quad (5.14)$$

Using polar coordinates(Figure 5.6) above equation writes as

$$f^B(r, \phi) = \int_0^\pi P(r \cos(\phi - \theta), \theta) d\theta \quad (5.15)$$

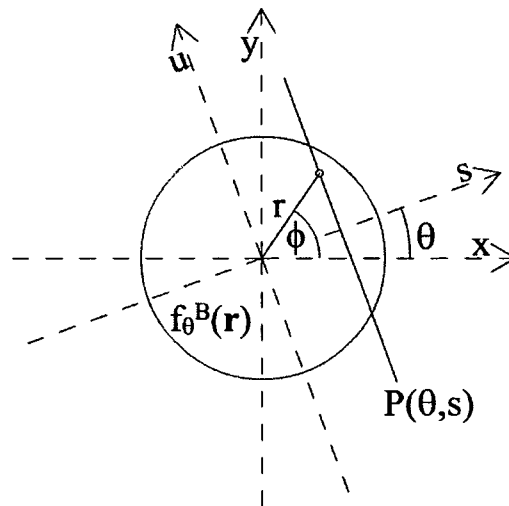


Figure 5.6: Geometry for transforming Cartesian coordinates to polar coordinates for backprojection

As an example an idealized object point in the origin of the coordinate system is assumed . The corresponding object function of $f(\mathbf{r}) = \delta(\mathbf{r})$ leads to projections $P_\theta(s) = \delta(s) \forall \theta$ and their backprojection writes as

$$f_\delta^B(\vec{r}) = f_\delta^B(x, y) = f_\delta^B(r, \phi) = \int_0^\pi \delta(s) d\theta = \int_0^\pi \delta(r \cos(\phi - \theta)) d\theta \quad (5.16)$$

Noting the rules for the Dirac delta function

$$\delta[g(\xi)] = \frac{1}{|dg(\xi)/d\xi|_{\xi=\xi_0}} \delta(\xi - \xi_0) \quad , \quad g(\xi_0) = 0 \quad (5.17)$$

and

$$g(\xi) = g(\theta) = r \cdot \cos(\phi - \theta) = 0 \quad \text{with} \quad \begin{aligned} \theta_0 &= \phi + \frac{\pi}{2} & \forall \bar{r} \in [0, \frac{\pi}{2}] \vee [\pi, \frac{3\pi}{2}] \\ \theta_0 &= \phi - \frac{\pi}{2} & \forall \bar{r} \in [\frac{\pi}{2}, \pi] \vee [\frac{3\pi}{2}, 0] \end{aligned} \quad (5.18)$$

equation (5.16) can be written as

$$f_{\delta}^B(r, \phi) = \frac{1}{\left| r \cdot \sin\left(\phi - \phi \pm \frac{\pi}{2}\right) \right|_0^{\pi}} \int_0^{\pi} \delta(\theta - \theta_0) d\theta = \frac{1}{r} \quad (5.19)$$

Therefore

$$f^B(\bar{r}) = f(\bar{r}) \otimes \frac{1}{r} = \iint f(\bar{r}') \frac{1}{|\bar{r} - \bar{r}'|} d^2 r' \quad (5.20)$$

where \otimes indicates a convolution in the space domain. According to the Convolution Theorem a convolution of two functions in the space domain is equivalent to a multiplication of their Fourier transforms and equation (5.20) writes as

$$F^B(\vec{s}) = F(\vec{s}) \cdot \frac{1}{s} \quad (5.21)$$

As the function $1/s$ represents a low-pass filter, equation (5.21) shows that the use of a direct backprojection algorithm would lead to strong distortions in the reconstructed image. On the base of equation (5.21) one could make a first approach for an exact reconstruction of the object function $f(x,y)$. The steps for the algorithm would be as follows

$$\begin{aligned} BP &= f^B \\ F^B &= FT_{(2)} f^B \end{aligned}$$

$$\begin{aligned}
 F &= F^B \cdot s \\
 f &= FT_{(2)}^{-1} F
 \end{aligned}
 \tag{5.22}$$

where $FT_{(2)}$ and $FT_{(2)}^{-1}$ denote the two-dimensional Fourier transform and inverse Fourier transform respectively. Though in principle possible, the implementation of equations (5.22) in a reconstruction algorithm would lead to long calculation times because of the repeatedly determination of the two-dimensional Fourier transform.

5.2.3 Filtered Backprojection

In the present paragraph the concept of filtered backprojection, an algorithm currently used in almost all applications of straight X-ray tomography, will be developed. It has been shown to be extremely accurate and much faster than the algorithm described above.

The general inverse Fourier transform

$$f(\vec{r}) = \iint F(\vec{s}) \exp[i2\pi(\vec{s} \cdot \vec{r})] d^2s \tag{5.23}$$

writes in Cartesian coordinates $\vec{s} = (s_x, s_y)$ as

$$f(x, y) = \int_{-\infty}^{\infty} \int_{-\infty}^{\infty} F(s_x, s_y) \exp[i2\pi(xs_x + ys_y)] ds_x ds_y \tag{5.24}$$

Introducing Polar coordinates $\vec{s} = (s_s, \theta)$ (analog to Figure 5.6) and noting that

$$\int_{-\infty}^{\infty} ds_x \int_{-\infty}^{\infty} ds_y [\dots] \rightarrow \int_0^{2\pi} d\theta \int_0^{\infty} s_s ds_s [\dots] \rightarrow \int_0^{\pi} d\theta \int_{-\infty}^{\infty} |s_s| ds_s [\dots] \tag{5.25}$$

the inverse Fourier transform can be written as

$$f(\vec{r}) = \int_0^{\pi} \int_{-\infty}^{\infty} |\vec{s}| F(\vec{s}) \exp[i2\pi\vec{s} \cdot \vec{r} \cos(\phi - \theta)] ds ds_s = \int_0^{\pi} \int_{-\infty}^{\infty} |s_s| F(s_s, \theta) \exp[i2\pi s_s r \cos(\phi - \theta)] ds_s d\theta \tag{5.26}$$

respectively, using the coordinate transformation from equation (5.1)

$$f(x, y) = \int_0^{\pi} \int_{-\infty}^{\infty} |s_s| F(s_s, \theta) \exp[i2\pi s_s (x \cos \theta + y \sin \theta)] d\theta ds_s \quad (5.27)$$

Taking the Fourier Slice Theorem into account equation (5.27) can be interpreted as follows:

High-pass filtering in the frequency domain

$$F^*(s_s, \theta) = |s_s| \cdot F(s_s, \theta) = |s_s| [FT_{(1)} P_{\theta}(s)](s_s) \quad (5.27a)$$

Inverse Fourier Transform

$$P_{\theta}^*(x \cos \theta + y \sin \theta) = P_{\theta}^*(\xi) = \int_{-\infty}^{\infty} F^*(s_s, \theta) \exp[i2\pi s_s \xi] ds_s \quad (5.27b)$$

Backprojection operator B

$$f(\vec{r}) = \int_0^{\pi} P_{\theta}^*(x \cos \theta + y \sin \theta) d\theta \quad (5.27c)$$

The above equations represent the basic steps of the filtered backprojection algorithm. Instead of projections P_{θ} filtered projections P_{θ}^* are used to compensate for the smoothing characteristics of the backprojection (equation 5.21). Due to the fact, that the Fourier transform has to be calculated only once this algorithm is much faster than the one presented in the previous paragraph.

According to the Convolution Theorem the multiplication of the filter function in the Fourier domain is equivalent to a one-dimensional convolution of the projection with the inverse Fourier transform of the filter function (convolution kernel) in the space domain.

A filter function most popular in tomography, namely the band limiting filter (equation 5.28) for a bandwidth of $s_0 = 0.5$ is displayed in Figure 5.7.

$$k_{B,s_0}(s) = s_0^2 \left(2 \cdot \frac{\sin(2s_0 s)}{2s_0 s} - \left[\frac{\sin(s_0 s)}{s_0 s} \right]^2 \right) \quad (5.28)$$

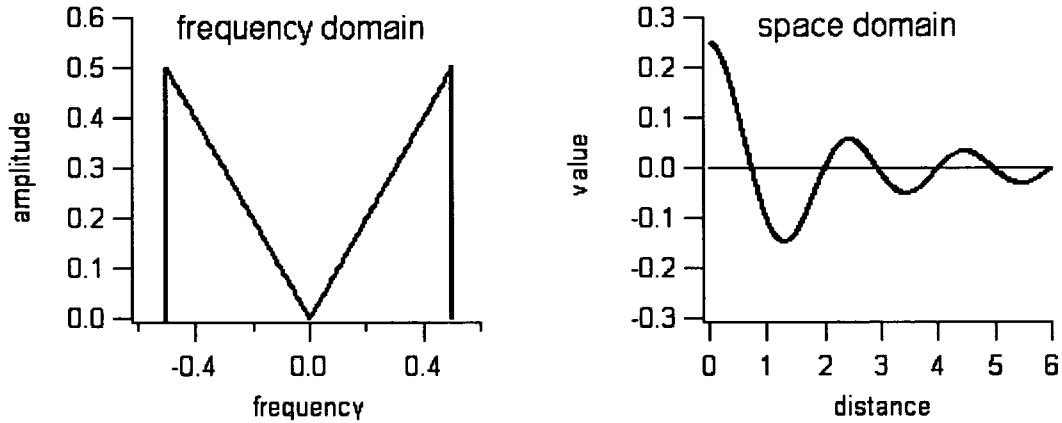


Figure 5.7: representation of the band limiting filter in the frequency and in the space domain.

As mentioned above, in practice projection data is only available on a discrete grid of points ($\theta_n = n\Delta\theta$, $s_m = m$). In this case the projection algorithm (equation 5.27 a-c) in the space domain is written as

Convolution of the projection $P_n(m)$ with the convolution kernel $k_x(m)$

$$P_n^*(m) = \sum_m^M P_n(m') k_x(|m - m'|) \quad (5.29 \text{ a})$$

Backprojection of the filtered projections $P_n^(m)$*

$$f_{ij} = \sum_{n=0}^N P_n^*(x_j \cos \theta + y_i \sin \theta) \Delta\theta \quad (5.29 \text{ b})$$

where M is the number of measured points per projection (number of rays), N the number of projections (number of angles) and (i, j) denote the pixels of the reconstructed object function. In the discrete case the convolution kernel of the band limiting filter for $s_0 = 0.5$ is given by

$$\begin{aligned} k_B(m=0) &= \frac{1}{4} \\ k_B(m=2,4,6\dots) &= 0 \\ k_B(m=3,5,7\dots) &= -\frac{1}{4} \left[\frac{\sin(m/2)}{(m/2)} \right]^2 = -\frac{1}{m^2 \pi^2} \end{aligned} \quad (5.30)$$

5.3 X-ray Absorption Tomography

In this paragraph the mathematical concepts derived above will be linked to the physical properties of the attenuation of X-rays in matter and the type of information provided by this type of analysis will be discussed.

When X-rays pass through a homogeneous absorber they suffer attenuation and lose intensity, which is described by Beer-Lambert law

$$I = I_0 \exp[-\mu\Delta y] \quad (5.31)$$

where I_0 is the primary intensity, I the intensity after attenuation, μ the linear attenuation coefficient and Δy the thickness of the absorber.

If the matter is inhomogeneous and therefore $\mu = \mu(x,y)$ equation 5.31 has to be written as

$$I = I_0 \exp\left[-\int_0^D \mu(x,y) dy\right] \quad (5.32)$$

and the measured intensity I is proportional to the line integral of the linear absorption coefficient along the beam-path in the sample. Comparing equation 5.32 with the definition of line integrals (equation 5.2) one can see, that the projections necessary for reconstruction are defined by

$$\ln \frac{I_0}{I(x,y)} = \int_0^D \mu(x,y) dy \quad (5.33)$$

in the coordinate system where the object rests (see Figure 5.1) and by

$$P_\theta(s) = \ln \frac{I_0}{I(s,u)} = \int_{-\infty}^{\infty} \mu(s,u) du \quad (5.34)$$

in the system rotated with the direction θ of the projection. Together with the mathematical concepts discussed in the previous paragraphs equation 5.34 is the base for X-ray absorption tomography, which allows to determine the two-dimensional spatial (in depth of the object) distribution of the linear attenuation coefficient in the sample.

Since the measurement of projection data represents a periodic problem only a sample rotation by 180° is necessary to obtain the full information from absorption tomography.

5.4 X-ray fluorescence tomography

While within conventional X-ray absorption tomography the transmitted beam is measured to determine the spatial distribution of the absorption coefficient inside a sample, X-ray fluorescence tomography is based on the detection of fluorescence photons emitted from the sample. From such measurements the internal elemental composition of the sample can be obtained. However, the reconstruction problem for this technique is much more difficult than that of transmission tomography, mainly due to self absorption effects in the sample.

While in this paragraph the basics of fluorescence tomography will be introduced, the concepts of implementing the data from absorption measurements in the reconstruction algorithm for this problem will be discussed in chapter 6.5.

Figure 5.8 shows a scheme of a typical setup for combined absorption/fluorescence tomography.

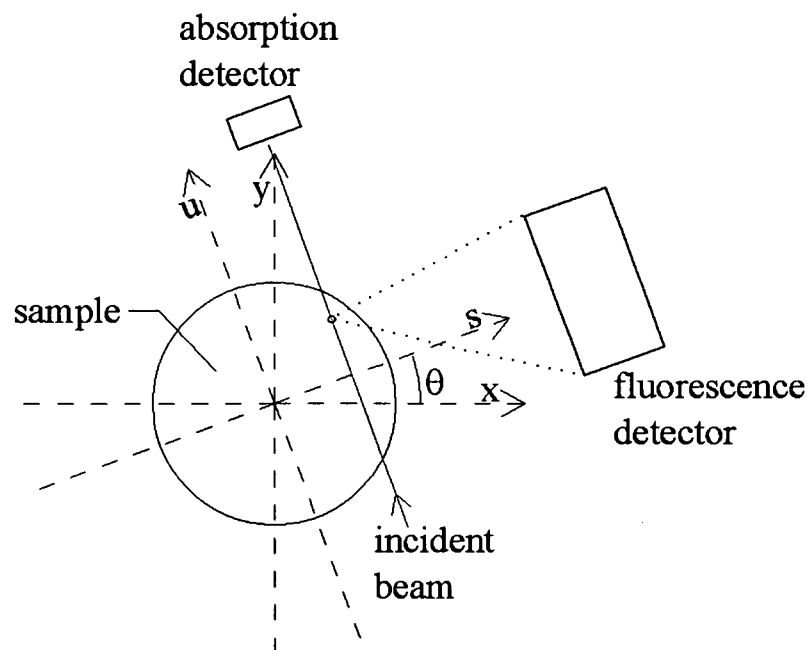


Figure 5.8: Scheme of an experimental setup for combined fluorescence- and absorption tomography

An absorption detector is placed in the forward direction of the strongly collimated parallel X-ray beam for measuring the photons transmitted through the sample. A second (energy dispersive) detector is placed perpendicular to the incident beam and measures the fluorescence photons emitted from the sample. For performing translation and rotation scans the sample is placed on a micrometer driven stage which allows to scan along the direction perpendicular (s -direction) to the X-ray beam and to rotate the sample around an axis perpendicular to the incident plane of the beam. For better understanding a rotating source-detector system is shown in Figure 5.8, while usually these components are fixed and the sample moves relatively to the X-ray beam.

The contribution of a small path du along the beam to the detected fluorescence signal of the element i is given by

$$dI_i = I_0 \varepsilon_{E_i} f(s, u) p_i(s, u) g_i(s, u) du \quad (5.35)$$

I_0	intensity of the incident beam
ε_{E_i}	detector efficiency for the energy E_i of the fluorescence photon
$f(s, u)$	probability that a photon from the source reaches the point (s, u)
$p_i(s, u)$	probability of fluorescent emission per unit path length per unit solid angle
$g_i(s, u)$	probability that a photon emitted by the element i at the point (s, u) reaches the detector

Defining an attenuation correction K_i at the point (s, u) by

$$K_i(s, u) = f(s, u) g_i(s, u) \quad (5.36)$$

and performing integration, the detected intensity I_i normalized by I_0 and ε_{E_i} is given by

$$I_i(s, \theta) = \int_{-\infty}^{\infty} K_i(s, u) p_i(s, u) du \quad (5.37)$$

with

$$p_i(s, u) = \frac{1}{4\pi} \frac{N_A \rho_i}{A_i} \sigma_i(E_0) \quad (5.38)$$

where N_A is Avogadro's number, ρ_i and A_i are the density and the atomic weight of the i th element and $\sigma_i(E_0)$ the cross section of the fluorescent line i at incident energy E_0 .

While $f(s, u)$ in the attenuation correction K_i is related to the absorption coefficient $\mu(s, u)$ via

$$f(s, u) = \exp\left[-\int_{-\infty}^{\infty} \mu(s, u', E_0) du'\right] \quad (5.39)$$

the correction term for the detection path has to be written as

$$g_i(s, u) = \int_{\Omega_D} d\Omega \exp\left[-\int_{(s, u)}^{Det} \mu(l, E_i) dl\right] \quad (5.40)$$

where Ω_D is the solid angle the interaction point to the detector surface and $\mu(l, E_i)$ is the absorption coefficient at the characteristic energy of the fluorescence photon. The integral along l in the exponential function is calculated from the point (s, u) to the detector surface element enclosed by the solid angle $d\Omega$.

While $\mu(s, u, E_0)$ can be calculated directly from the absorption tomography, $\mu(s, u, E_i)$ is much more difficult to evaluate and has to be implemented in the reconstruction algorithm [66]. The approach for this problem used in this work will be discussed in detail in chapter 7.6.

6 X-ray Sources

Nowadays three different types of X-ray sources, namely radioactive materials, X-ray tubes and synchrotrons, are commonly used in the field of X-ray spectroscopy. From the analysts point of view the main distinctive features between the three sources are the spectral distribution of the emitted radiation as well as the number of photons emitted (or to be more precise, the brilliance of the source). The features and properties of X-ray tubes and synchrotrons – the two sources used during this work - will be discussed in the following paragraphs.

6.1 X-ray tubes

A typical assembly of an X-ray tube is shown in Figure 6.1. Electrons, produced at a candent filament by thermoionic emission, focused by a (concave) tube kept at high negative potential, are accelerated towards a target (anode) material kept at ground potential. The pure target material is embedded in a hollow anode block (mostly copper) cooled by running water for heat dissipation. The electrons hitting the target at the so called *focal spot* interact with the atoms of the anode material in two different ways. Either the electrons are stepwise decelerated and give rise to the continuum spectrum, or vacancies in the inner shells of the atoms are created. If the holes are subsequently filled with electrons from higher shells, photons with an energy characteristic for the anode material are emitted. Therefore the spectrum from an X-ray tube will always contain both, bremsstrahlung and characteristic X-rays. Due to the given geometries (Figure 6.1) only a fraction of the emitted radiation (defined by the aperture in the shielding and the *take-off* angle) will leave the tube. Since high voltages (~10-60 kV) have to be applied the whole system is operated in a sealed evacuated glass tube. The opening for X-ray emission is covered with a thin beryllium window in order to maintain the vacuum inside the cavity. Although of X-ray tubes are rather inefficient (~99% of the power is converted to heat) they are widely used for laboratory applications.

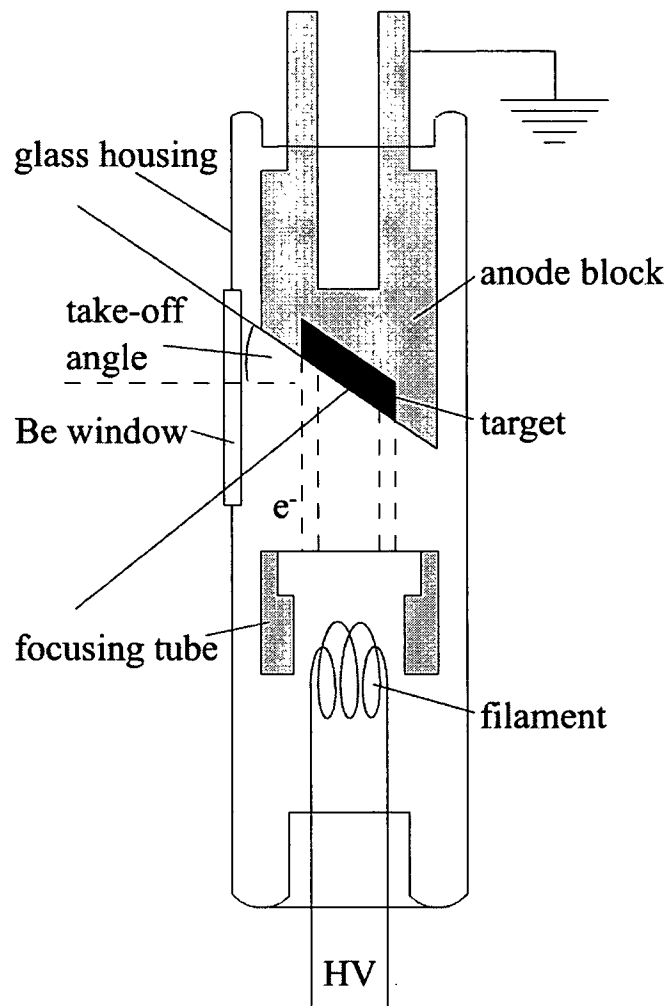


Figure 6.1: X-ray tube, schematically

6.2 Synchrotron Radiation

Synchrotron Radiation is the ideal source for most X-ray experiments. Compared to laboratory instruments, using X-ray tubes, it has unique properties like high photon flux, natural collimation, polarization and tunability of the energy of the primary photons. Making optimal use of these properties by specially designed experimental set-ups allows investigations on a micro scale not accessible with laboratory instruments. In this chapter a short introduction on the origin and characteristics of synchrotron radiation will be given. A more detailed discussion on this topic can be found in [67].

6.2.1 Origin of synchrotron radiation

When charged particles are accelerated electromagnetic radiation is emitted. A charged particle moving through an uniform magnet magnetic field is accelerated perpendicularly to its moving direction and performs a circular motion. The radiation power emitted within this process is given by

$$\frac{dP(\theta)}{d\Omega} \propto \sin^2 \theta \quad (6.1)$$

where θ is the angle between the directions of the acceleration and the transmission of the electromagnetic wave.

Let us consider two coordinate systems $S(\mathbf{r},t)$ and $S'(\mathbf{r}',t')$. Let $S(\mathbf{r},t)$ be the system where the observer rests while $S'(\mathbf{r}',t')$ is the frame where the accelerated particle is in rest. Since the relative velocity v between $S(\mathbf{r},t)$ and $S'(\mathbf{r}',t')$ in case of synchrotron storage rings is almost the speed of light, the Lorentz transformation for velocities is linking the two systems. The radiation emitted at an angle θ' from the z' axis of $S'(\mathbf{r}',t')$ is observed in the frame $S(\mathbf{r},t)$ at an angle θ from the z axis. The expression for the angle θ , derived from the Lorentz transformation is

$$\tan(\theta) = \frac{1}{\gamma} \cdot \frac{\sin(\theta')}{\cos(\theta') + \beta} \quad (6.2)$$

where $\beta = v/c$, and $\gamma = 1/\sqrt{1 - \beta^2}$.

The resulting radiation patterns in $S'(r',t')$ and $S(r,t)$ are shown in Figure 6.2 a) and b) respectively.

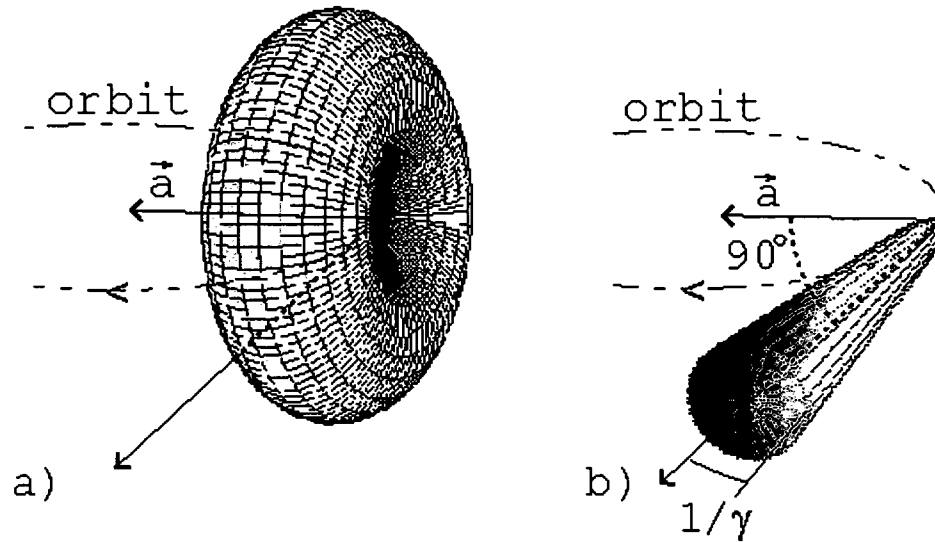


Figure 6.2: Radiation pattern of an accelerated particle. In the frame of reference moving with the relativistic particle (a) and the frame of reference of the observer (b) [14]

It can be shown, that the root mean square of the radiation emission angle ϕ , which corresponds to the half of the cone angle is inversely proportional to γ .

$$\langle \phi^2 \rangle^{1/2} \approx \frac{1}{\gamma} \quad (6.3)$$

For an electron with an energy of 1GeV $\gamma = 1957$, which leads to a natural beam collimation of 0.5 mrad. Since such emissions exist in every point of the orbit, the consideration holds for the vertical spread, whereas the horizontal spread can be much higher.

6.2.2 Intensity and spectral distribution

Schwinger [68, 69] provided the expression for the power emitted instantaneously by an electron traveling on a circular path or radius r at relativistic velocities. The radiation power

(C.G.S. units) per electron $\frac{d^2W}{d\psi d\lambda}$ [erg/(sec rad cm e)] is given by

$$\frac{d^2W}{d\psi d\lambda} = \frac{27}{32\pi^3} \frac{e^2 c}{r^3} \left(\frac{\lambda_c}{\lambda}\right)^4 \gamma^8 [1 + (\gamma\psi)^2]^2 \left[\underbrace{K_{2/3}^2(\xi)}_P + \frac{(\gamma\psi)^2}{1 + (\gamma\psi)^2} \underbrace{K_{1/3}^2}_N \right] \quad (6.4)$$

where

$$\xi = \frac{1}{2} \frac{\lambda_c}{\lambda} [1 + (\gamma\psi)^2]^{3/2}$$

$$\lambda_c = \frac{2\pi c}{\omega_c} \quad \text{critical wavelength}$$

$$\omega_c = \frac{3}{2} \gamma^3 \omega_0 \quad \text{critical frequency}$$

$$\omega_0 = \frac{c}{r}$$

ψ is the vertical angle between the orbital plane and the observer. $K_{p/q}$ are modified Bessel functions of fractional order.

By dividing the equation for the radiation power (6.4) by the single photon energy hc/λ the number of emitted photons per second per electron is obtained

$$\frac{d^3N}{dt d\psi d\lambda} = \frac{9}{8\pi^2} \frac{e^2}{hr^2} \left(\frac{\lambda_c}{\lambda}\right)^3 \gamma^5 [1 + (\gamma\psi)^2]^2 \left[K_{2/3}^2(\xi) + \frac{(\gamma\psi)^2}{1 + (\gamma\psi)^2} K_{1/3}^2 \right] \quad (6.5)$$

Assuming a length L of the storage ring and the speed of the electrons to be c , the number of electrons n can be calculated from the current J

$$n = \frac{L}{ec} J \quad (6.6)$$

A parameter used to describe the synchrotron beam is the *brightness* $\frac{d^3N}{dt d\Omega d\lambda / \lambda}$. It is defined as the number of photons per unit time, steradian, milliampere and 0.1% wavelength bandwidth [photons/(sec mrad² 0.1%b.w. mA)]. Another parameter used to describe the

intensity of synchrotron radiation is called *brilliance*. It includes the size of the radiation

source and is defined as $\frac{d^4N}{dt d\Omega dS d\lambda / \lambda}$ [photons/(sec mrad² mm² 0.1%b.w. mA)].

Integrating equation 4.4 over all vertical angles ψ the spectral distribution of the radiation is obtained. In Figure 6.3 the spectral distribution of the whole beam as well as of the radiation emitted in the orbital plane ($\psi=0$) is shown.

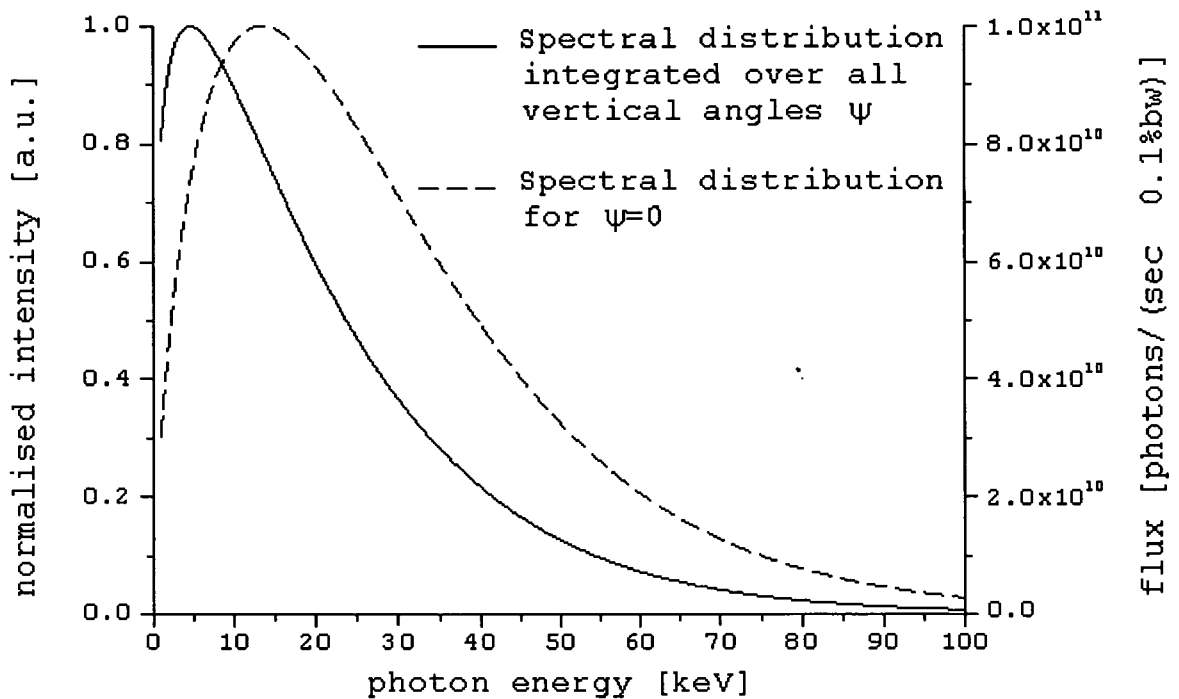


Figure 6.3: Normalized spectral distribution calculated for bending magnets at HASYLAB. Integrated spectral distribution is shown in full, Spectral distribution in the orbital plane is shown in dashed. The flux scale refers to the integrated distribution. [14]

6.2.3 Polarization

The two terms in the equation (4.4) labeled with P and N indicate the intensities in the two directions of the polarization I_N and I_P , having the electric vector normal and parallel to the orbital plane respectively.

Defining a degree of linear polarization P_1 of the radiation as

$$P_l = \frac{I_P - I_N}{I_P + I_N} = \frac{K_{2/3}^2(\xi) - \frac{(\gamma\psi)^2}{1 + (\gamma\psi)^2} K_{1/3}^2}{K_{2/3}^2(\xi) + \frac{(\gamma\psi)^2}{1 + (\gamma\psi)^2} K_{1/3}^2} \quad (6.7)$$

one can see that this term is strongly depending on the angle ψ . Figure 6.4 shows the values for I_N and I_P as well as the degree of linear polarization for 4 different energies for the bending magnet beamline L at HASYLAB, Hamburg.

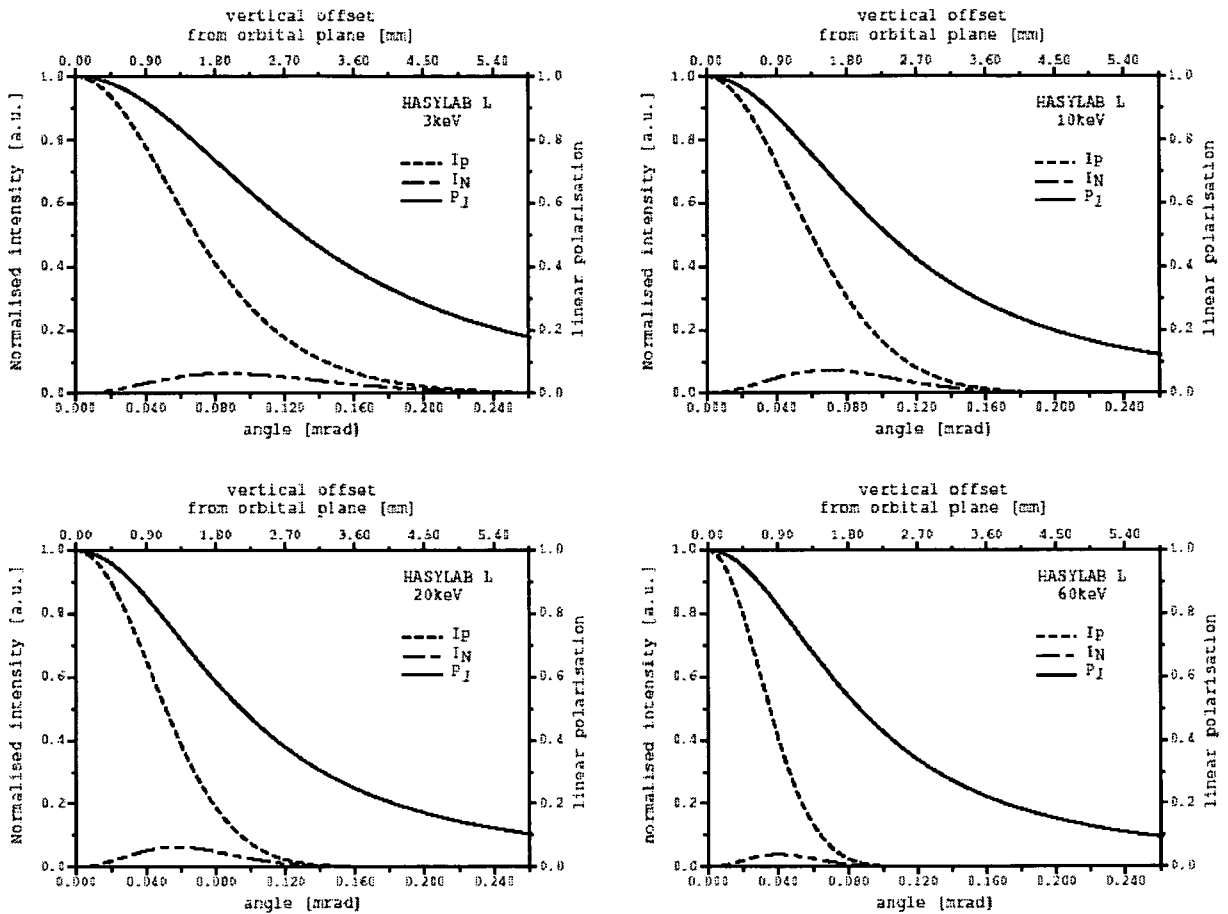


Figure 6.4: Angular distribution of normalized intensities with electric vector parallel (P) and normal (N) to the orbital plane and degrees of linear polarization P_l for the bending magnet beamline L, HASYLAB for the energies 3, 10, 20 and 60 keV. A distance of 22.5 meters between source and experiment has been assumed. [14]

It can be clearly seen, that the parallel component I_N reaches its maximum at $\psi = 0$ while I_P is zero at $\psi = 0$ and has small peaks above and below the plane. The degree of linear polarization $P_l = 1$ (100% polarization) at $\psi = 0$ and decreases, as ψ increases.

6.2.4 Insertion devices

A synchrotron storage ring in principle consists of three different sections. Magnetic dipoles – so called bending magnets – providing a homogeneous magnetic field are used to keep the charged particles on a circular trajectory. In addition to the bending magnets there are straight sectors, where quadrupole- and sextupole magnets focus and stabilize the beam. To compensate for the loss in energy of the particles, due to emission of electromagnetic radiation, during every cycle there are RF accelerating cavities installed.

In second and third generation synchrotrons additional sections have been designed to insert special devices allowing to force the charged particles to various trajectories. Due to this, so called insertion devices it is possible to have more intense sources than produced by bending magnets, to change or extend the shape of the spectral distribution, to change the polarization features or to have an X-ray beam with smaller divergence.

Since the properties of the electromagnetic radiation emitted by bending magnets has been described in the previous paragraphs, here only the features of the insertion devices will be discussed.

6.2.4.1 Wavelength shifters

A wavelength shifter consists of three magnetic dipoles arranged as a linear array, where the central one has a higher B field compared to the two on the side (Figure 6.5).

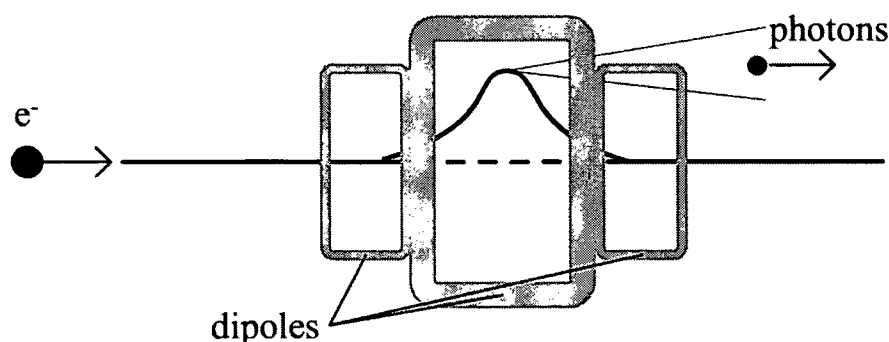


Figure 6.5: schematic view of a 3-pole wavelength shifter

By the first pole the charged particles are deflected horizontally and constrained to trajectory with a narrow radius by the second one. Finally the charged particles are forced back to the original orbit by the third magnetic dipole. The energy of the emitted photons is strongly dependent on the radius of the trajectory and therefore on the local magnetic field.

Wavelength shifters are used to extend the emitted spectrum to higher photon energies. In combination with superconducting technology they allow the production of hard X-rays by electrons with moderate electron energy.

6.2.4.2 Wigglers

An increased photon flux can be achieved by a sequence of magnetic dipoles with altering field direction (Figure 6.6). As an electron beam passes through such arrays it is forced to an almost sinusoidal trajectory.

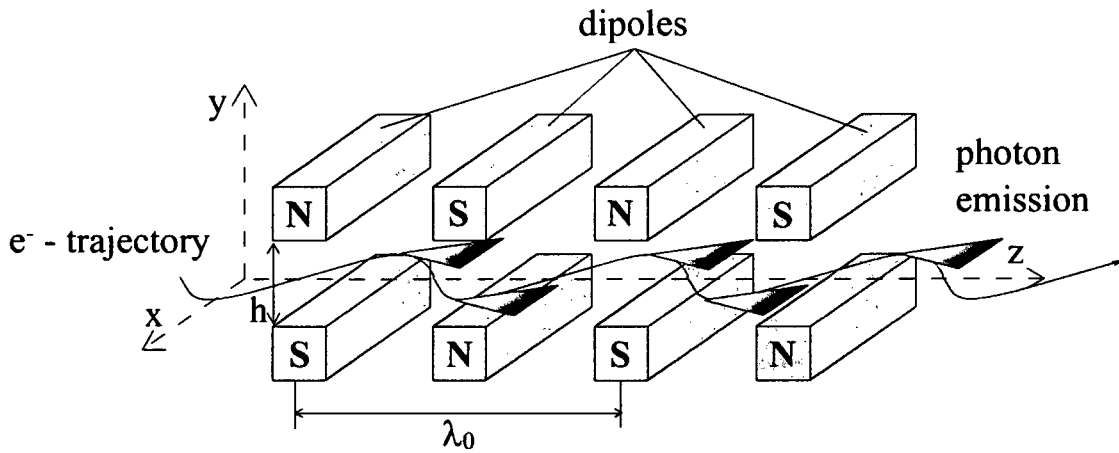


Figure 6.6: Scheme of a multipole wiggler

Each time the electron changes its direction, synchrotron radiation of critical energy ϵ_c is emitted. The radiation emitted at each dipole occurs as a sequence of short pulses and is incoherently superimposed. To distinguish between multipole wigglers and undulators, which are similarly constructed, the so called *deflection parameter* K is defined as

$$K = \frac{eB_0\lambda_0}{2\pi mc^2} \quad (6.8)$$

where λ_0 is the magnet period length and B_0 the peak magnetic field. For a multipole wiggler typically $K \gg 1$, which is accomplished by high magnetic fields and long magnet period lengths λ_0 .

The maximum deflection angle δ of the electron beam relatively to the z -axis is given by

$$\delta = \frac{K}{\gamma} \quad (6.9)$$

leading to a horizontal opening angle of $2\delta = 2K/\gamma$.

If N is the number of wiggler periods, the central brightness of a wiggler is $2N$ times higher compared to the one of a bending magnet.

6.2.4.3 Undulators

Undulators are similarly built as multipole wigglers (Figure 6.6), but with deflection parameters $K < 1$. This is realized by a larger number of dipoles and weaker magnetic fields. The traverse displacement in an undulator is reduced compared to a wiggler and the deflection angle is comparable to the emission cone. The radiation emitted at each turning points of the electron beam is coherently superimposed and strong interference effects influence the spectral and spatial distribution. In the emission spectrum sharp peaks with discrete wavelengths λ , given by

$$\lambda = \frac{\lambda_0}{2i\gamma^2} \left(1 + \frac{1}{2}K^2 + \gamma^2\theta^2 \right), i = 1, 2, 3, \dots \quad (6.10)$$

appear. Where θ is the angle between the z -axis and the direction of observation.

The spectral intensity of the radiation is proportional N^2 , where N is the number of dipoles and the width of the spectral line is proportional to $\frac{1}{iN}$.

Figure 6.7 compares the brilliance of bending magnets with various insertion devices from different synchrotron sources (HASYLAB, BESSY, ESRF) [70].

Figure 6.8 shows the different properties of synchrotron radiation due to insertion devices, compared to bending magnets.

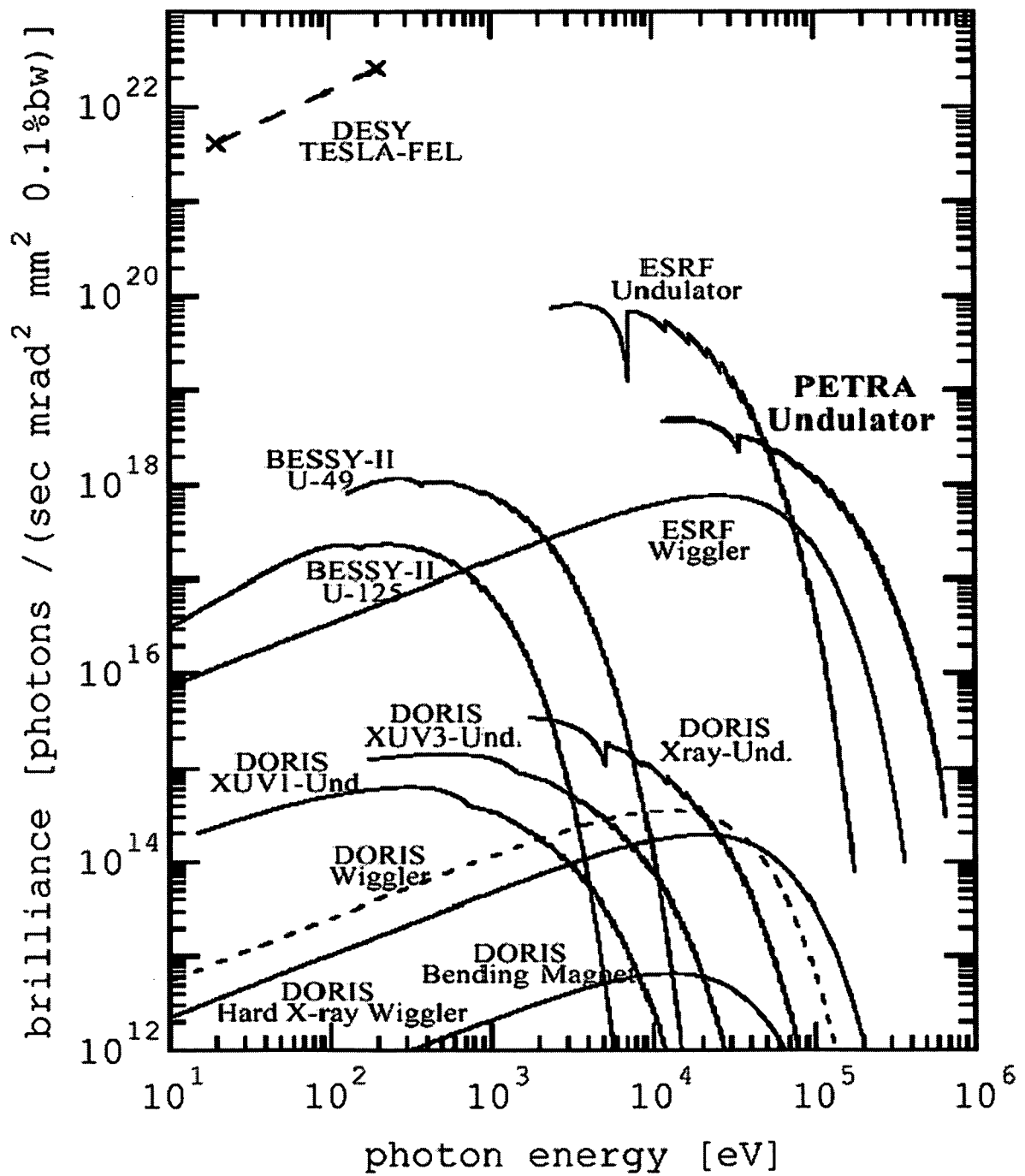


Figure 6.7: Brilliance of bending magnets and different insertion devices.

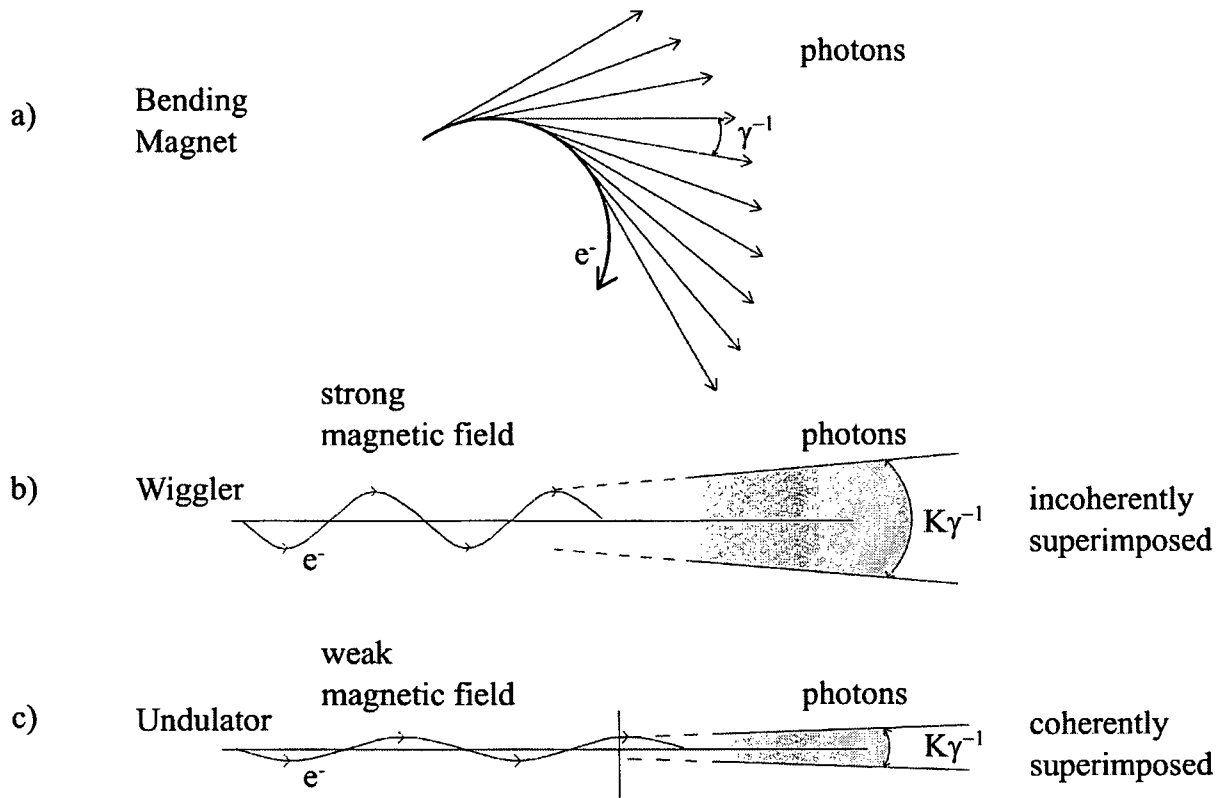


Figure 6.8: Comparison of emitted synchrotron radiation from a) bending magnets, b) wigglers and c) undulators

7 Elemental distribution in human bones

Bone acts as a sink for various chemical elements. Besides the obvious, such as Ca also different essential (e.g. Zn) and nonessential (e.g. Pb) metals are accumulated in bone tissue. Since only little is known about the distribution of those elements in human bones, synchrotron radiation induced micro X-ray fluorescence analysis (SR μ -XRF) measurements have been carried out to gain better knowledge on this topic.

7.1 Medical introduction

7.1.1 Effects of lead on the human organism

The toxicity of Pb has been recognized for centuries. In the past years many clinical studies have been carried out, to investigate the health effects associated with exposure to Pb and internal Pb doses in humans. The adverse effects of Pb on the different body systems, such as cardiovascular-, gastrointestinal-, hematological-, renal-, and neurological system, linked to the duration of Pb exposure are summarized in the Toxicological Profile for Lead [71]. The presented studies are mainly based on the determination of blood lead levels as an indicator of the absorbed Pb dose, which requires, due to the uptake, metabolism and storage of Pb in the human organism a precise knowledge of the past history of exposure to Pb.

Pb is primarily absorbed through the gastrointestinal and respiratory tracts, and the absorption efficiency is influenced by the route of exposure, chemical speciation and the age and the physiological state of the exposed individual. Immediately after absorption, Pb is distributed to blood plasma and soft tissues, before it redistributes and accumulates in bone. Bone lead accounts for about 73% of the total body burden in children, increasing to 90-95% in adults due to the changes in bone turnover rates with age. Furthermore the bonding of Pb to bone seems to be much stronger than it is to blood, resulting in a biological half-life of Pb in bone of about 6-12 years [72, 73] compared to 1 month in blood. Due to this bone is seen as a cumulative “dosimeter” for Pb exposure and has therefore been extensively investigated by in vivo XRF measurements using either K-shell or L-shell excitation [74]. The large pool of Pb in bones together with the long biological half life can serve to maintain blood lead levels long after exposure has ended, and can also serve as a source to Pb transfer to the fetus when maternal skeleton is catabolized for the production of fetal skeleton [75]. Furthermore

increased Pb excretion is observed with increased bone metabolism such as hyperthyroidism. Recently it was shown that Pb correlates with excreted mature bone collagen as determined by desoxypyridinoline cross-links [76, 77]. To fully understand fully these mobilization processes, the knowledge of the storage sites and the distribution of Pb in bones is of medical importance.

7.1.2 Function and structure of human bone

Bone is a specialized connective tissue forming, together with cartilage the skeletal system. In principle it serves three functions: (1) mechanical, as support and site of muscle attachment for locomotion; (2) protective, for vital organs and bone marrow; and (3) metabolic, as a reserve of ions for homeostasis. Unlike in other connective tissues, the extracellular matrix in bone has the ability to become calcified.

On a macroscopic level one can distinguish between flat bones (e.g. skull bone) and long bones, such as tibia, femur and humerus. As shown in Figure 7.1 a long bone can be divided into the epiphyses at the ends and in the diaphysis (midshaft) in the middle. The external part of the bone is formed by a thick layer of calcified tissue, the compact bone, which, in the diaphysis encloses the medullary cavity (housing for hematopoietic bone marrow). Towards the epiphyses the compact bone becomes thinner and the internal space is filled with a network of calcified trabeculae (trabecular bone). The bone surfaces at the epiphyses (taking part in the joint) are covered with a layer of articular cartilage (noncalcified).

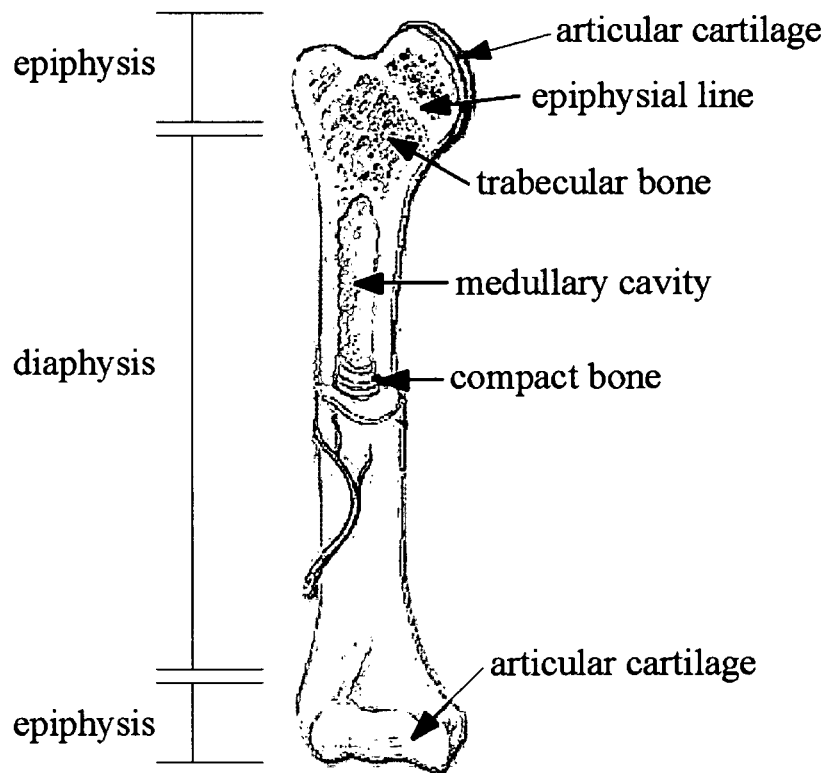


Figure 7.1: Macroscopic structure of a long bone, adopted from [78]

Taking a detailed view on the epiphysial zone (Figure 7.2) a substructure in the compartment of compact bone is exhibited. As seen from the high magnification backscattered electron image (Figure 7.2 (b), see paragraph 7.33) as well as from the histological image (Figure 7.2 (c)) one can distinguish between subchondral bone (IV) and calcified cartilage(III). Also the so called tidemark (II) is seen, which divides the articular (noncalcified) cartilage (I) from the calcified cartilage, and is thought to be a metabolically active calcification front advancing in the direction of noncalcified cartilage. Individual bone packets of different age, and therefore appearing in different gray levels in Figure 7.2 (b), are separated by cement lines (V) [79].

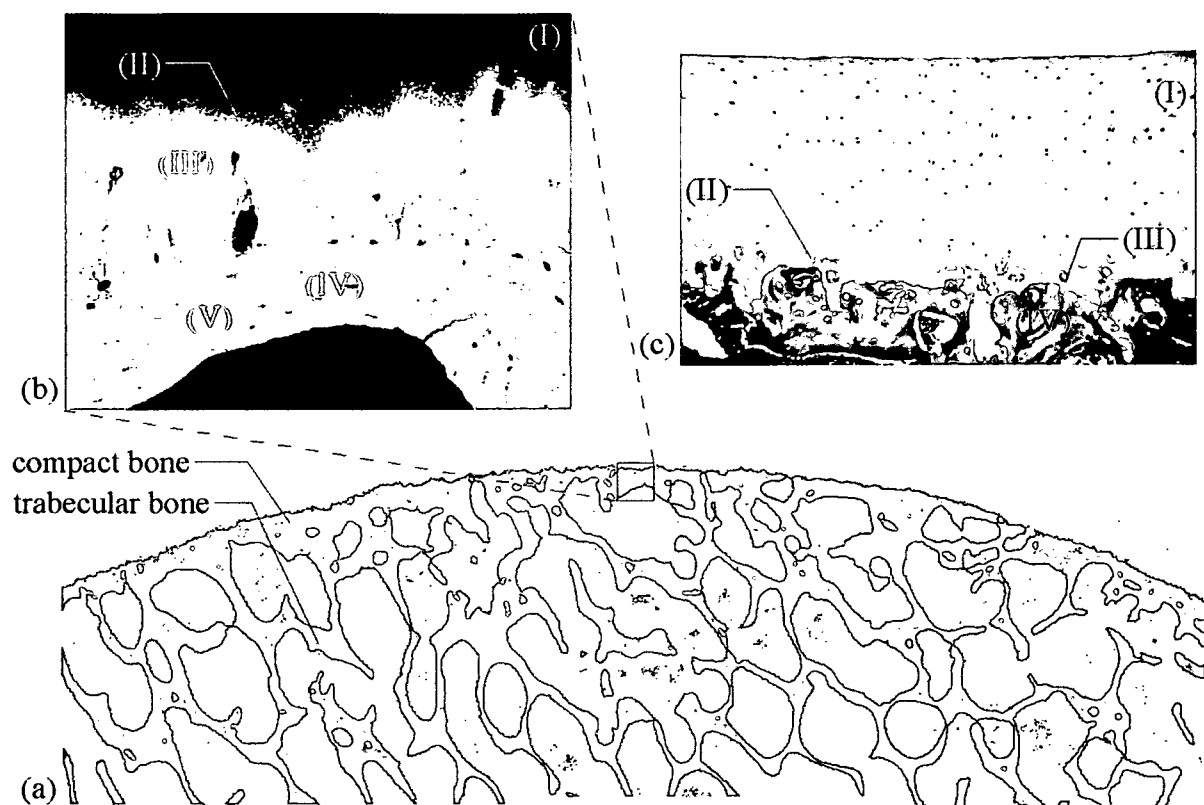


Figure 7.2: detailed view of the epiphysis. Low magnification backscattered electron imaging (a) shows the difference between trabecular and compact bone. A substructure of the tissues is exhibited by high magnification backscattered electron imaging (b) and histological staining(c) [80]. Articular (noncalcified) cartilage (I), tidemark (II), calcified cartilage (III), subchondral bone (IV), and cement lines can be seen

7.2 Micro XRF on 4mm bone slices

7.2.1 Experimental setup

Measurements have been carried out at the micro focus end station at HASYLAB beamline L (Figure 7.3). Whereas a detailed description of the installed X-ray optics has been given by G. Falkenberg et al. [81], here only the parts necessary for μ -XRF are described.

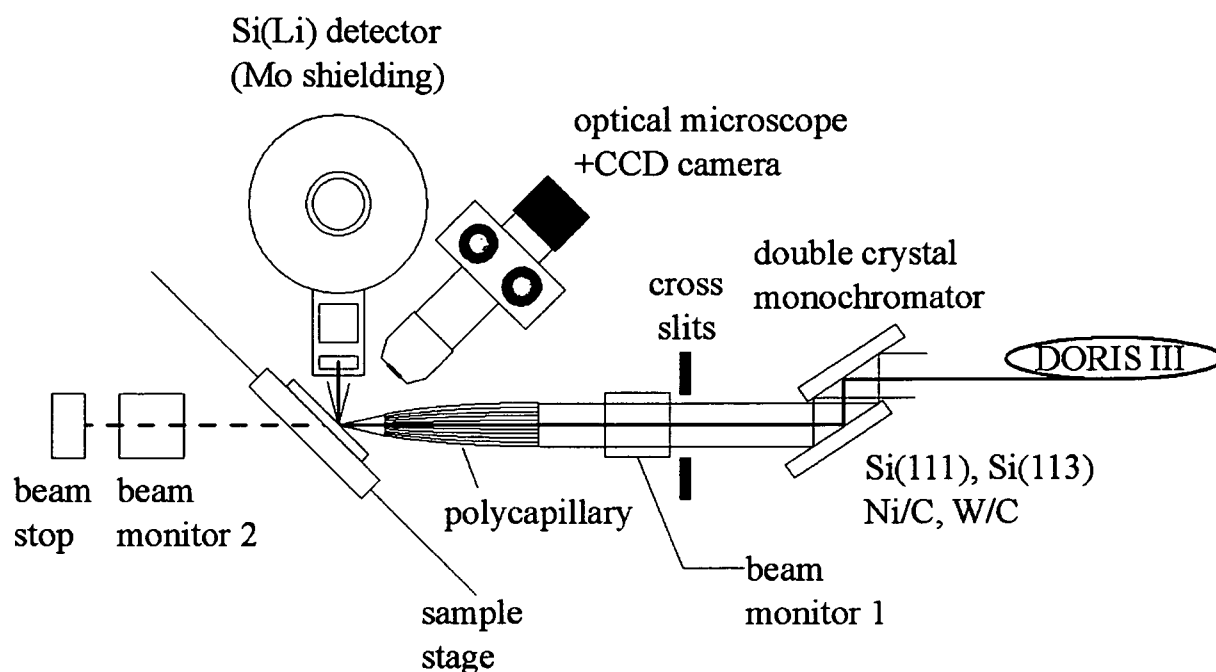


Figure 7.3: Schematic μ -XRF layout at HASYLAB, beamline L

The beamline is equipped with two (Si(111), Si(113)) fixed exit double crystal monochromators for high energy resolution and two multilayer pairs (Ni/C, W/C) for high flux applications. Focusing of the monochromatic X-rays is accomplished by a polycapillary half lens (XOS, X-Ray Optical Systems, Albany, New York), capable of concentrating the beam to a spot size of 10-20 μ m FWHM, depending on the energy. The focal distance of the capillary is about 5mm. The sample is mounted on a motor driven XYZ-sample stage with a maximum scanning range of 30mm in each direction. The fluorescence photons are detected by a Si(Li) semiconductor detector with an active area of 80mm², 4mm crystal thickness and a 12 μ m Be window (Gresham Sirius 80). In order to make optimal use of the linear polarization of the incoming beam (reduction of the scattered radiation) the detector is mounted in the orbital plane of the storage ring and the angle between beam and detector is fixed to 90°. The angle between beam and sample and sample and detector is fixed to 45° each. With this setup, minimum detection limits of about 10 ng/g can be achieved in biological materials [82]. To monitor the intensity of incoming and the focused beam, ionization chambers are installed in front of the capillary and behind the sample. For visually controlling the micro-beam position an optical microscope coupled with a high resolution CCD camera is used. The microscope is mounted to look perpendicular on the sample surface.

For the experiment the Si(111) crystal monochromator was chosen to produce a monochromatic incident beam with 17.5keV photon energy. Therefore the Pb-L lines were

sufficiently excited and an adequate peak to background ratio in the region between 10 and 13keV could be reached. For this energy a micro-beam spot size of 15 μ m FWHM was achieved. In order to obtain reasonable blank spectra, the standard Pb detector shielding was replaced by a Mo-cap and a Mo collimator was placed on the capillary exit.

7.2.2 Samples / sample preparation

Five femoral heads, two proximal tibiae and three bones from distal femur were prepared for analysis. The samples were extracted from surgically removed bones by bone saw cutting through the articular surface. All prepared slices were about 4 mm thick (Figure 7.4). The structure of the analyzed bones can be seen in Figure 7.5. Regions of noncalcified cartilage (I), cortical bone (II) and trabecular bone (III) can be clearly distinguished. The estimated extension of the cortical bone was about 500 μ m for all bone slices. For these samples it was not possible to distinct between calcified cartilage and subchondral bone in the area of cortical bone.

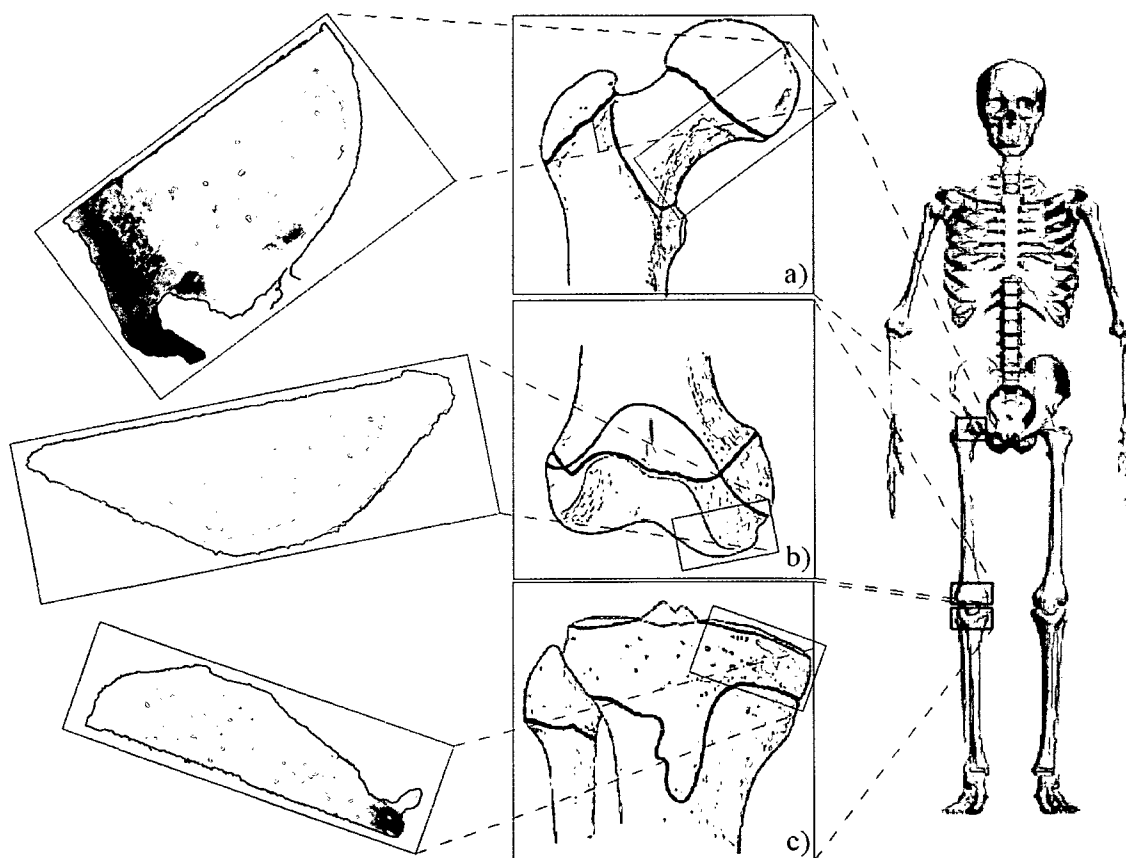


Figure 7.4: Bone slices from different areas of the human skeleton. 4mm slices have been prepared from the articular surfaces of femoral head (a), distal femur (b) and proximal tibia

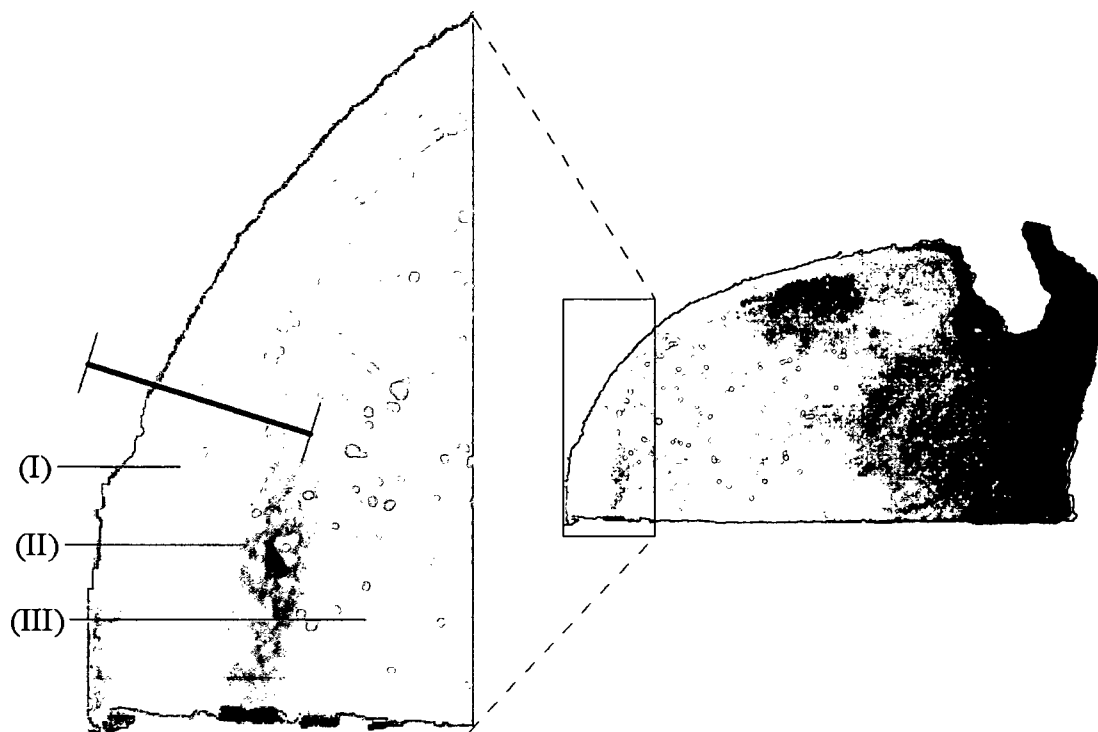


Figure 7.5: Structure of an analyzed femoral head, noncalcified cartilage (I), cortical bone (II), trabecular bone (III). The position of the performed μ -XRF scan is marked with a bar

7.2.3 Results and discussion

Ten samples were scanned and showed similar elemental distributions across the scan region. Results obtained from line scan on femoral head, starting in noncalcified cartilage and running across cortical and trabecular bone (see Figure 7.5), are shown in Figure 7.6 as a representative example.

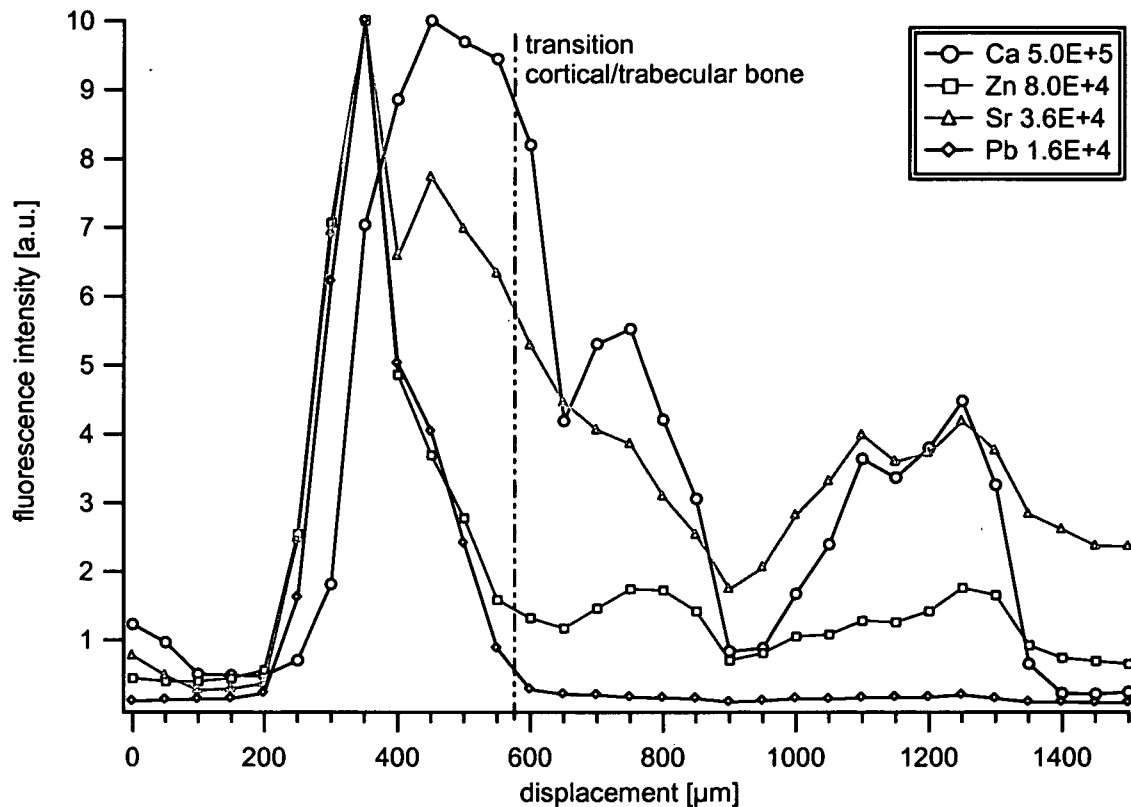


Figure 7.6: Results from a μ -XRF line scan in femoral head. The scan started in non calcified cartilage and ended in trabecular bone. The transition between cortical and trabecular bone (as determined by optical investigation with the microscope is marked). For displaying the individual intensity maxima for each element are normalized to 10. Absolute values for the maximum peak counts are given in the legend. All data has been normalized to 100mA ring current and 100 s measuring time per point. Step size during scan $d = 50\mu\text{m}$

All detected elements (Ca, Zn, Sr, Pb) showed significant differences in intensities across the analyzed region. As expected, Ca reaches its maximum intensities in cortical bone, where it stays almost constant. When reaching trabecular bone strong fluctuations in the fluorescence signal are observed, which are explained by the structure of this compartment (see Figure 7.5) hitting either spongy bone or holes in between. A similar distribution would have been expected for Sr which could only be partly proofed by these measurements. Pb, the main element of interest, was found to be mostly deposited in the cortical bone within a region of the outer $300\mu\text{m}$. While Zn showed additional rises in intensities around the transition to trabecular bone (coordinate $\sim 800\mu\text{m}$) and in trabecular bone (coordinate ~ 1300) a strong correlation of maximum intensities of Pb and Zn was detected in cortical bone, which is in agreement with the results obtained by other groups with particle induced X-ray emission spectroscopy [83, 84] and synchrotron radiation induced X-ray Spectroscopy [85]. Compared to the Ca signal, the intensity maxima of Zn, Sr and Pb are shifted about $100\mu\text{m}$ towards the

cartilage at the cartilage-bone interface (coordinate $\sim 200\text{-}300\mu\text{m}$). This shift is due to geometric effects, partly due to the 45° incidence angle of the primary beam and fluorescence take-off with respect to the sample surface. Another reason for the shift are the structural inhomogeneities of the bone along the beam path. While only the sample surface could be seen with the optical beamline microscope, no information was available about the underlying inhomogeneous bone structures. They contribute to the fluorescence spectrum depending on the investigated chemical element (see paragraph 4.4.1). Calculating the different information depth of the fluorescence signal in bone matrix (according to ICRU Report 4416 [86]), which vary from about $50\ \mu\text{m}$ for Ca to $700\ \mu\text{m}$ for Sr and is about $300\ \mu\text{m}$ for Pb, shows that these structural inhomogeneities are not negligible and lead to difficulties in the interpretation of the results. Therefore, although the beam size was $15\ \mu\text{m}$, the distribution of the elements could not be determined with the same lateral resolution.

A comparison of the obtained fluorescence spectra at scan position $350\mu\text{m}$ (maximum of Pb) and $1200\mu\text{m}$ (in trabecular bone) are shown in Figure 7.7. One can see that the measured differences in the elemental distribution are not due to counting statistics.

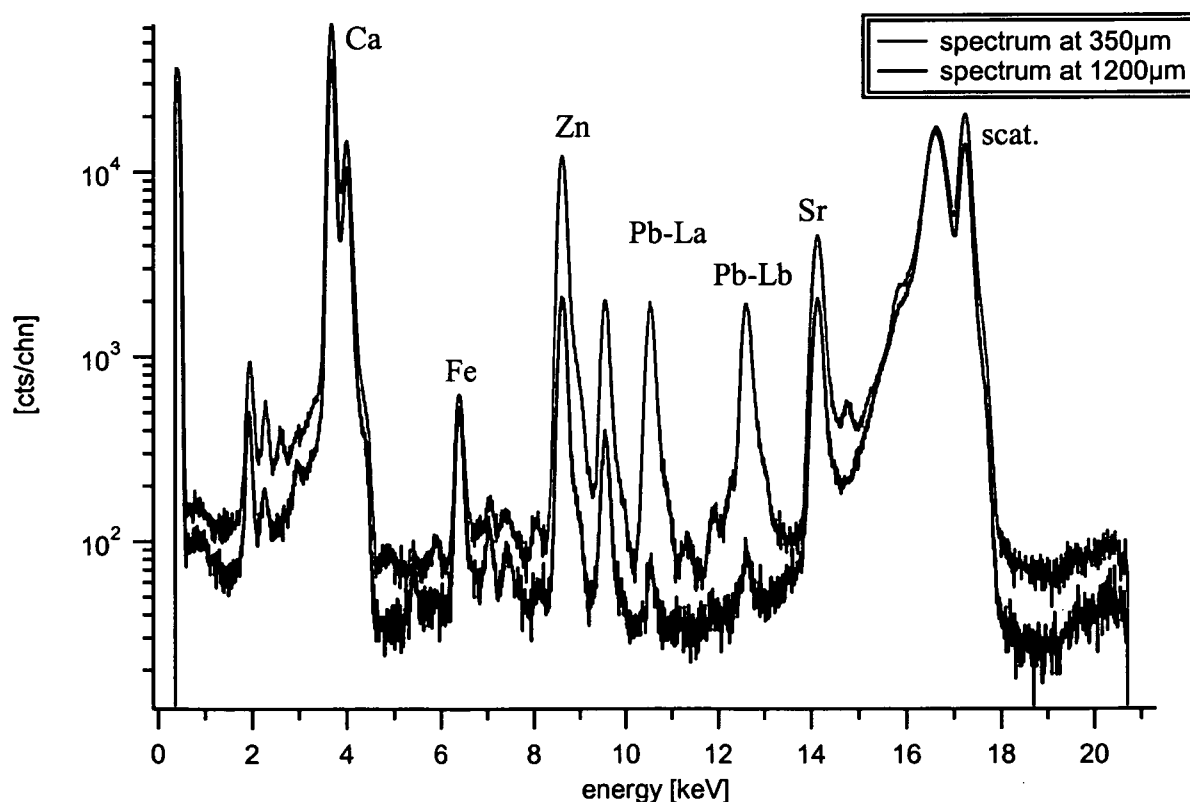


Figure 7.7: Comparison of fluorescence spectra at a scan position with high (red) and low (black) Pb intensities. Data was obtained in 500s measuring time and is normalized to 100mA ring current

7.2.4 Conclusions

In this first experiments it could be shown that SR- μ XRF is suitable for investigating the distribution of Pb and other (trace) elements in human bone. The new microbeam setup at HASYLAB, beamline L, is perfectly suited to perform these experiments, allowing line and surface scans in a reasonable measuring time. It was found that Pb is mostly accumulated in the cortical bone. It was observed that Pb and Zn are partly correlated for the analyzed bones, in the sense that in bone areas with higher Pb intensities increased intensities of Zn were detected. Using this type of samples (4mm thick) it was impossible to conclude whether the maximum in Pb intensities in the cortical bone was due to the described geometric and structural effects or due to Pb enrichment in this area.

7.3 Micro XRF on 200 μ m bone slices

7.3.1 Experimental Setup

In principle the same experimental setup described in paragraph 7.2.2 was used. To compensate for the sample thickness and therefore for the loss in sample mass the Ni/C multilayer pair was used for monochromatizing the synchrotron beam which leads to a gain in intensity by a factor of 80 compared to the Si(111) crystal [82]. The energy was again chosen to be 18keV and the reached beam size was determined to be 15 μ m.

7.3.2 Samples / sample preparation

For comparison with results obtained from measurements on the 4mm slices, one sample (femoral head) has been chosen for further analysis. Additionally human autopsy samples from five different subjects were obtained. The samples consisted in two cases of femoral head as well as patella tissue (paired autopsies), in two cases of femoral head tissue alone and in one case of only patella tissue. The age of the subjects covered a range from 48 to 63 years. The gender of the subjects distributed to three females and two males. The cause of death was in four cases heart attack and one case suicide by drugs. The samples were taken only from subjects with normal histomorphology of autopsies and no evidence of metabolic bone disease in the medical records. No post-mortem alterations were observed in any of the tissues as evidenced by backscattered electron imaging (BEI). The study was approved by the Institutional Ethical Review Board of the Institute of Forensic Medicine of the University of Vienna.

The tissue samples containing articular cartilage, subchondral and trabecular bone tissue were fixed in 70% ethanol and dehydrated in a graded series of ethanol before embedding in polymethylmethacrylate (PMMA). 200 μ m thick sections of tissue samples were prepared from the sample blocks by cutting, using a low speed diamond saw (Isomet, Buehler, Lack Bluff, IL, USA), followed by grinding and polishing using a precision polishing device (PM5 Logitech, Glasgow, Scotland). One side of the tissue sections was coated with a thin carbon layer (thickness \sim 4 nm) by vacuum evaporation for the examinations in the scanning electron microscope (SEM). Sample preparation and backscattered electron imaging has been performed by P. Roschger, Ludwig Boltzmann-Institute of Osteology Hanusch-Krankenhaus der WGKK und Unfallkrankenhaus Meidling der AUVA.

7.3.3 Backscattered electron Imaging

To visualize the mineralized phase of the cartilage and the bone tissue the material contrast of backscattered electron imaging was employed. This method is based on the phenomenon, that the backscattering coefficient of high energetic electrons is direct proportional to the average atomic number of the target material hit by the primary electron beam of a scanning electron microscope (SEM). In the case of mineralized tissue, which is mainly composed by an organic matrix (average atomic number $Z \sim 6$) and by mineral particles (carbonated hydroxyapatite) rich in calcium ions ($Z = 20$), the BEI-image contrast is therefore dominated by the calcium content of the tissue. Thus the technique allows to visualize and quantify very sensitively the local distribution of the mineral [79] with a resolution below 1 μ m. The escape depth from the specimen surface of the backscattered electrons is thereby about 1 micron at a primary electron energy of 20 keV. For bone areas, chosen for μ -XRF analysis BEI images at a series of magnifications 12x to 500x were acquired, where each area included noncalcified cartilage, tidemark, calcified cartilage, subchondral bone, trabecular bone and bone cavities [87, 88] (Figure 7.8).

Gray levels are directly correlated to the mineral content. (bright gray levels means high, and dark gray levels means low mineral content).

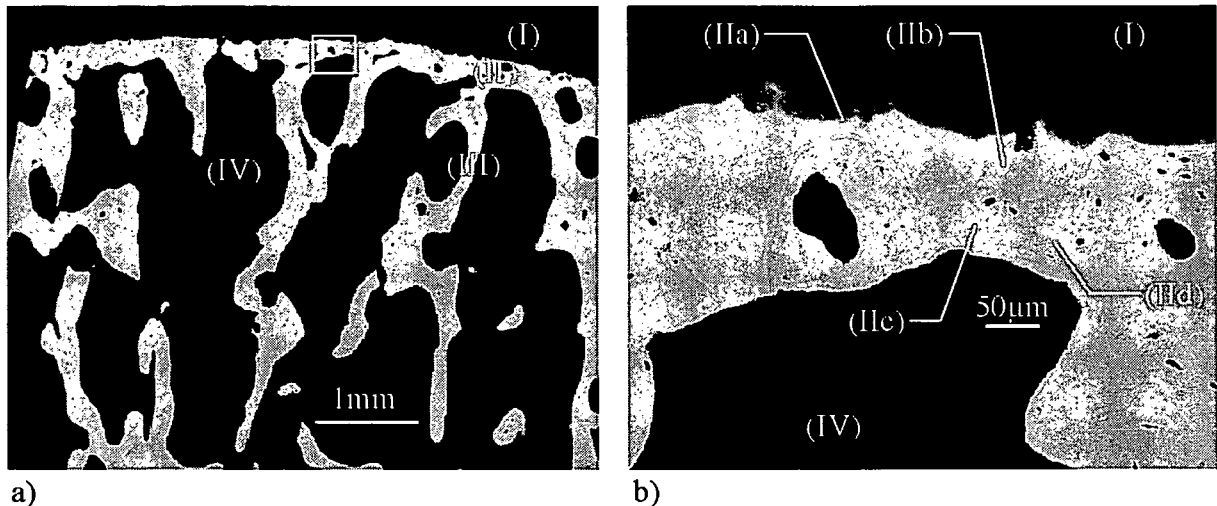


Figure 7.8: Backscattered electron images of a human bone slice at magnification 12x (a) and 500x (b). In (a) one can see noncalcified cartilage (I), cortical bone (II), trabecular bone (III) and bone cavities (IV). At high magnification (b) the tidemark (IIa), calcified cartilage (IIb), subchondral bone (IIc), and cement lines (IId) can be seen.

Backscattered electron imaging was performed using a digital scanning electron microscope (DSM 9662, Zeiss, Oberkochen, Germany) equipped with a four quadrant semiconductor BE-detector. The SEM was operated at an acceleration voltage of 20 kV, the working distance kept at 15 mm, and the probe current was maintained at 110 pA.

7.3.4 Results and discussion

Comparison with 4mm samples

A 200 µm thick slice was prepared from the previously analyzed femoral head (thickness about 4 mm). The already investigated region of the hip bone was chosen for preparation. The combination of BEI (Figure 7.9) and images from the beamline microscope of the thin bone slice facilitated the control of the actual position of measurement. The additional use of either transmitted or incident light allowed the identification of underlying bone structures with the microscope and therefore a more precise interpretation of the results was possible. Fluorescence intensities from a line scan over the region of cortical bone are presented in Figure 7.10. Although not extended to the region of trabecular bone, the analyzed region is comparable to that measured for the 4 mm thick sample. Analyzing fluorescence intensities with respect to BEI and microscope images, the cortical bone can be clearly identified, correlating with the steep increase and decrease in Ca intensities in bone structures. In contrast to Figure 7.6, Figure 7.10 exhibits a nearly constant fluorescence signal of Ca

throughout the investigated cortical bone (position 500-1200 μm) showing that geometric effects caused by the sample thickness are significantly reduced. Furthermore, the distance between the individual maxima of Pb and Ca was reduced. These results from the 200 μm slice confirm that Pb is not homogeneously distributed in cortical bone showing distinct maximum intensities in a border zone of about 100 μm around the interface to cartilage (around position 500 μm). The coincidence of Zn and Pb, already seen from measurements in the 4 mm samples could be verified. Furthermore it could be shown, that the maxima of Pb and Zn intensities are restricted to the outer border of the cortical bone. An additional peaking of Zn intensities could be seen within the cortical bone, which could not be detected for Pb.

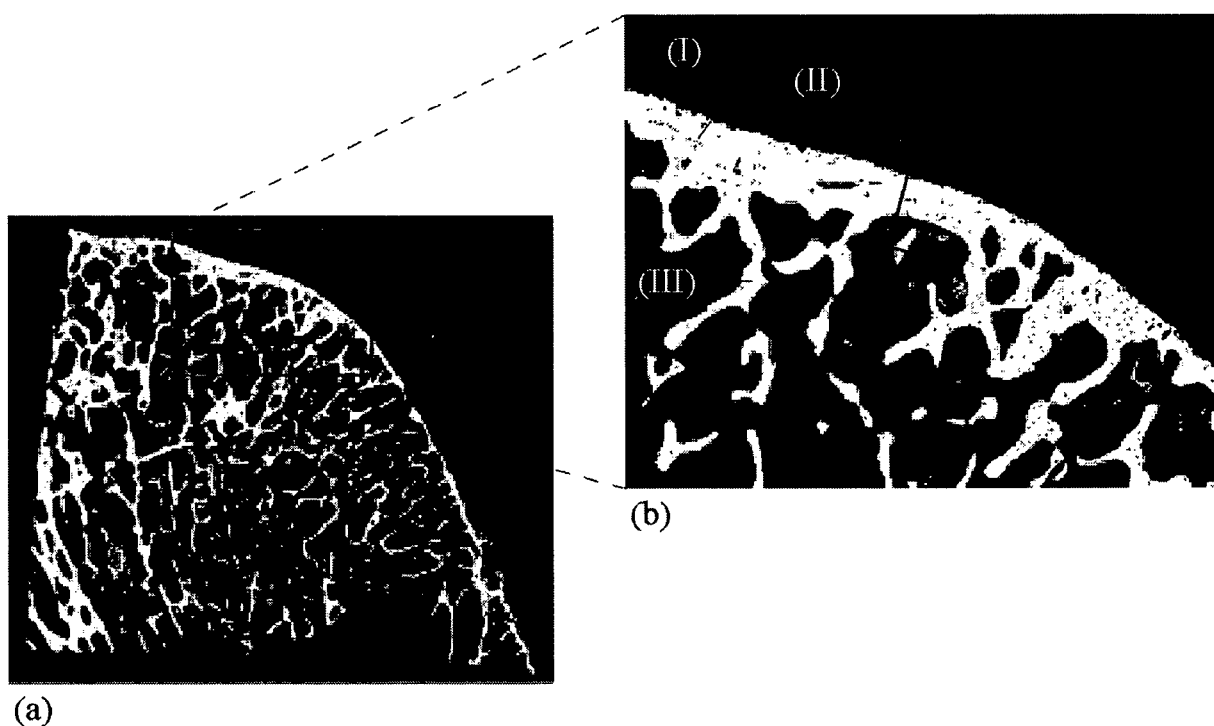


Figure 7.9: BEI of the prepared bone slice from femoral head at magnification 12 x (a). (b) shows a magnification of the inset in (a). Non calcified cartilage (I) can be clearly distinguished from cortical bone (II) and trabecular bone (III). The position of the $\mu\text{-XRF}$ scan is marked with a bar

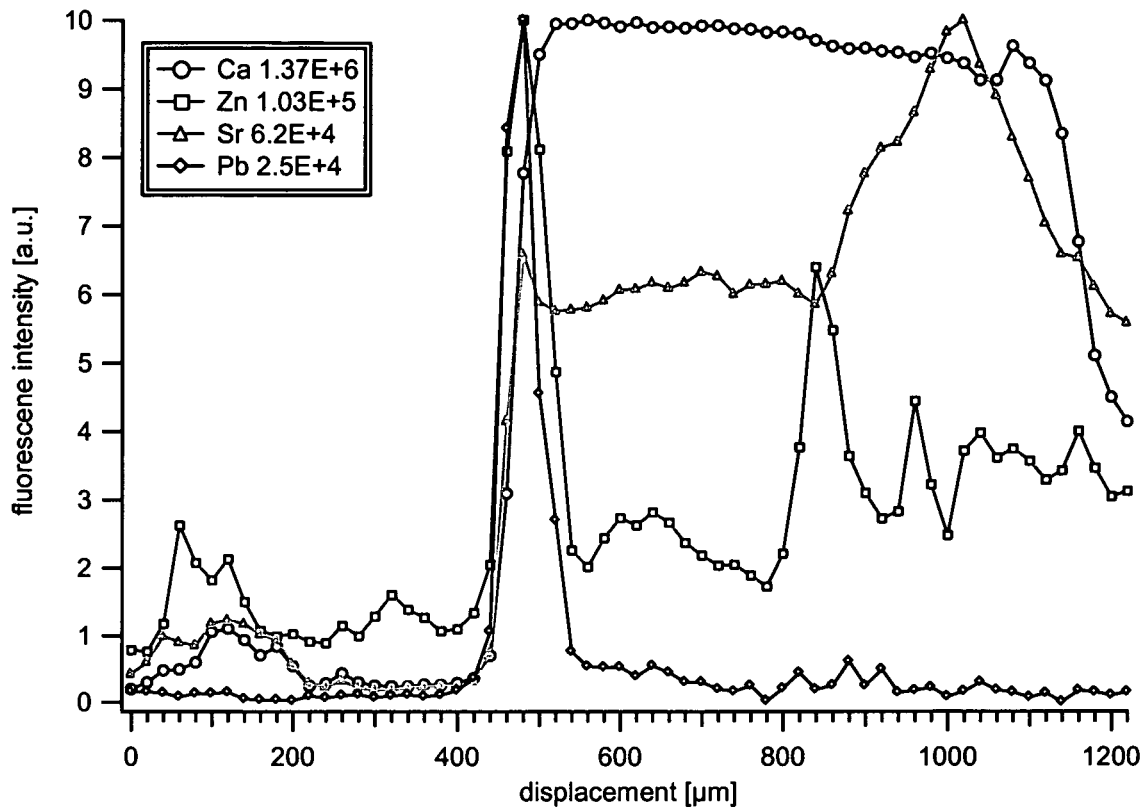


Figure 7.10: μ -XRF scan across cortical bone of a 200 μ m slice from femoral head. Data normalized to 100mA ring current and 100 s measuring time. For displaying the individual intensity maxima for each element are normalized to 10. Absolute values for the maximum peak counts are given in the legend

Fluorescence spectra at two points of the μ -XRF scan are shown in Figure 7.11. As one can see, using the multilayer monochromator instead of the Si(111) crystal provides enough photon flux to collect spectra with excellent peak to background ratio even at low elemental concentrations in the 200 μ m bone slices in reasonable time (10–100 s per measuring point).

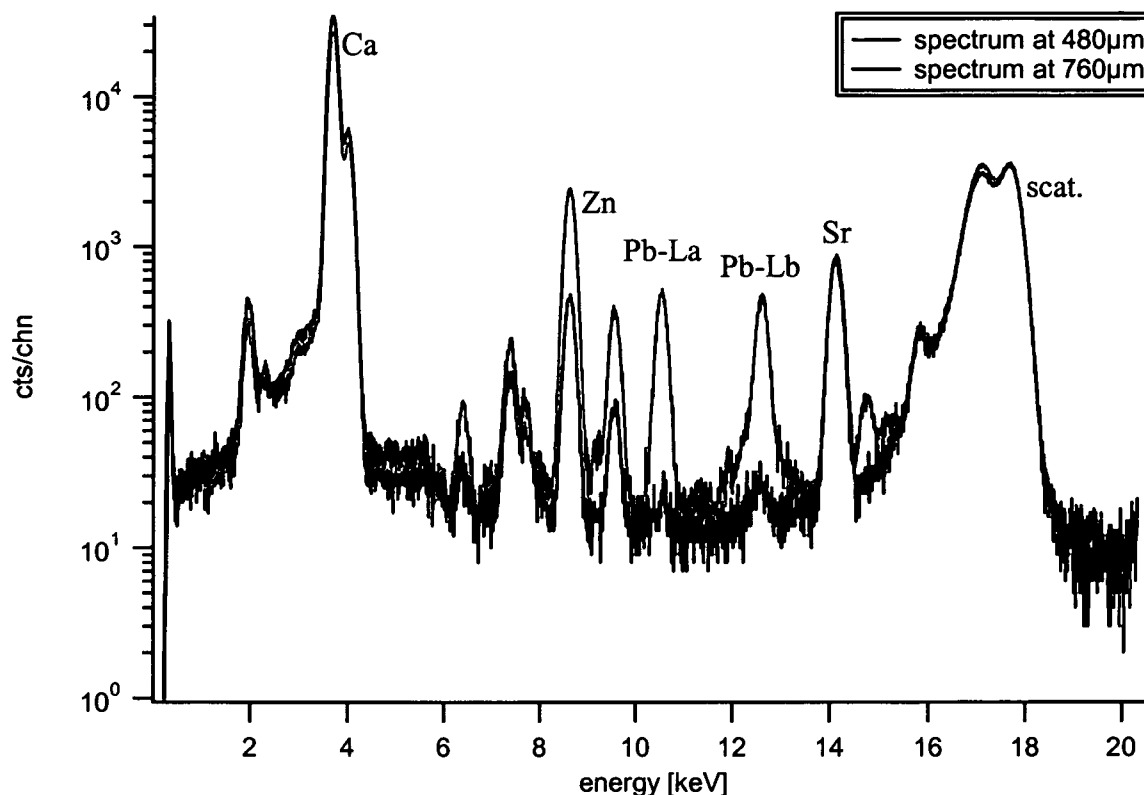


Figure 7.11: Spectrum comparison for a point of high (red) and low (black) Pb intensities. Spectra were measured using the multilayer monochromator instead of the Si(111) crystal. Data normalized to 100mA ring current and 100s measuring time

Human autopsy samples

Eleven μ -XRF line scans across cortical bone have been performed on 7 slices from femoral head and patella. For a measurement on a slice of femoral head the position of the scan as well as the obtained elemental distributions can be seen in Figure 7.12 and 7.13 respectively. The performed scan started in noncalcified cartilage, included the zone of calcified cartilage and subchondral bone and ended in the region of trabecular bone in a bone cavity (see Figure 7.12). As seen from comparison of Figure 7.12 and 7.13 in the zone of noncalcified cartilage no significant characteristic X-ray intensities of the elements considered (Ca, Zn, Sr, Pb) were detected. In the transition zone to calcified cartilage a strong increase of the Zn and Pb intensities is observed which decays rapidly in the region of calcified cartilage (after 100 μ m), whereas Ca and Sr are almost constant over the whole region of cortical bone. A matching of the intensity maxima of Zn and Pb with the transition zone formed between noncalcified- and calcified cartilage can be seen. Comparing the Pb intensities in the transition zone and the subchondral bone a ratio of 10/1 is observed, whereas the ratio for Zn is 10/4. Additionally Zn shows a moderate increase at the border to the bone cavity. Further investigating the

distribution of Zn along the scanned line shows an increase of this element at the border to the bone cavity.

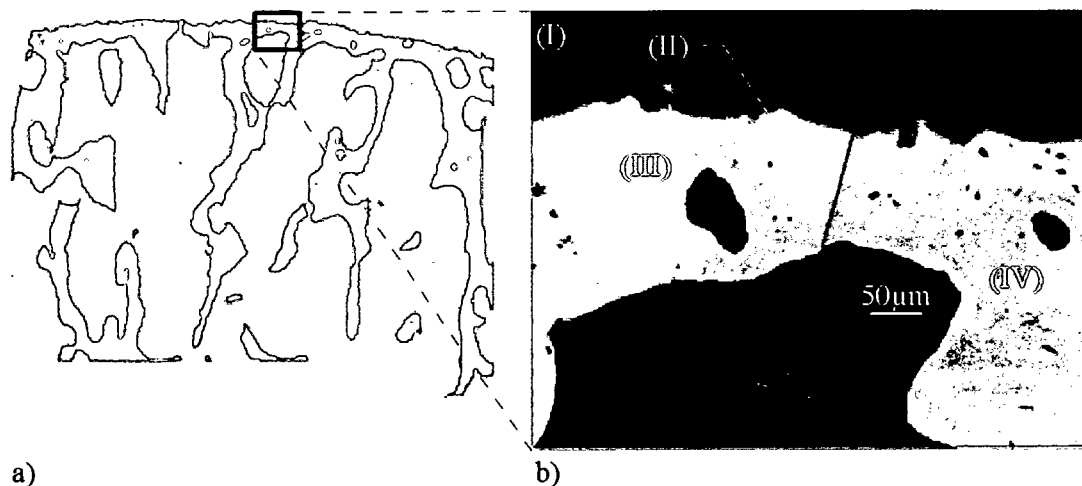


Figure 7.12: BEI of an analyzed femoral head at magnification 12 x (a) and 500 x (b). Non calcified cartilage (I), the tidemark (II), calcified cartilage (III), and subchondral bone (IV) can be seen. The position of the μ -XRF line scan is marked by the red bar in (b)

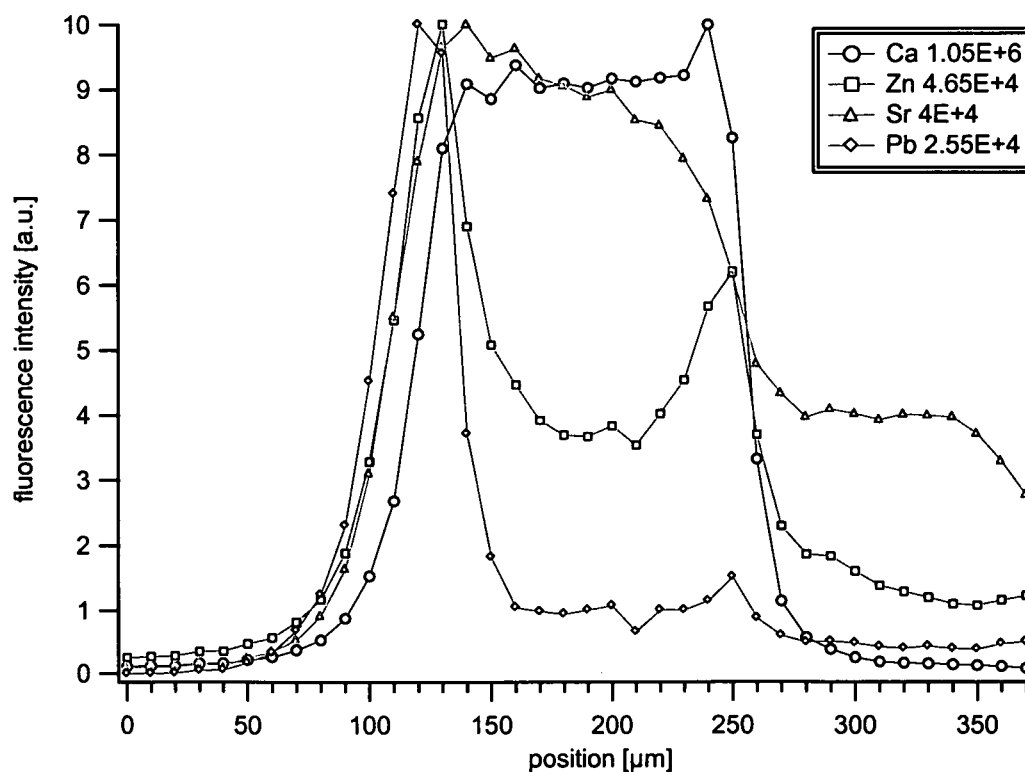


Figure 7.13: μ -XRF scan across cortical bone of a 200 μ m slice from femoral head. Data normalized to 100mA ring current and 100 s measuring time. Scan step width: $d=10\mu$ m. For displaying the individual intensity maxima for each element are normalized to 10. Absolute values for the maximum peak counts are given in the legend

A more or less comparable elemental distribution can be observed for a line scan in human patella (Figure 7.14, 7.15). Although the scan was not performed over the whole area of cortical bone (due to the large extension of this compartment in the patella) the scanned zones are similar to that of the scan in femoral head, including again noncalcified cartilage, calcified cartilage and subchondral bone (Figure 7.14). As shown in Figure 7.15 the distribution of Ca and Sr is comparable to that already seen in femoral head, having an intensity plateau across the region of calcified tissue. Also for Zn and Pb increased intensities are detected at the transition zone between noncalcified and calcified cartilage. In contradiction to the measurement in femoral head two local intensity maxima can be seen, which can either be explained by the presence of two Pb and Zn accumulating zones or by geometry effects due to the irregular structure of the sample and therefore by contributions of underlying bone structures (not seen by the optical microscope or by backscattered electron imaging) to the fluorescence spectra.

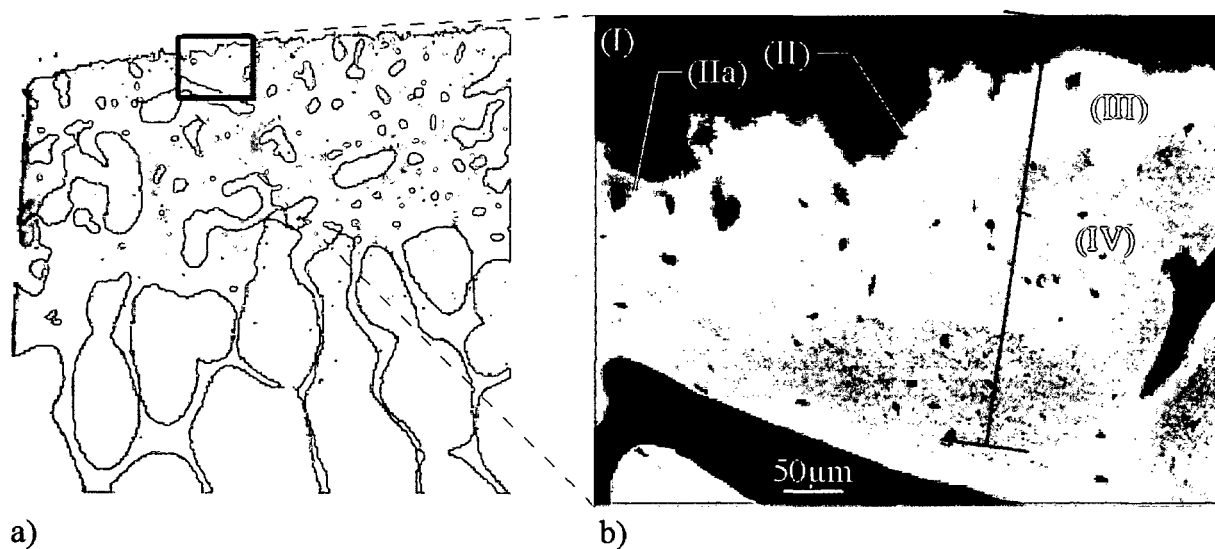


Figure 7.14: BEI of an analyzed patella sample at magnification 12 x (a) and 500 x (b). Non calcified cartilage (I), the tidemark (II), a double tidemark (IIa), calcified cartilage (III), and subchondral bone (IV) can be seen. The position of the μ -XRF line scan is marked by the red bar in (b)

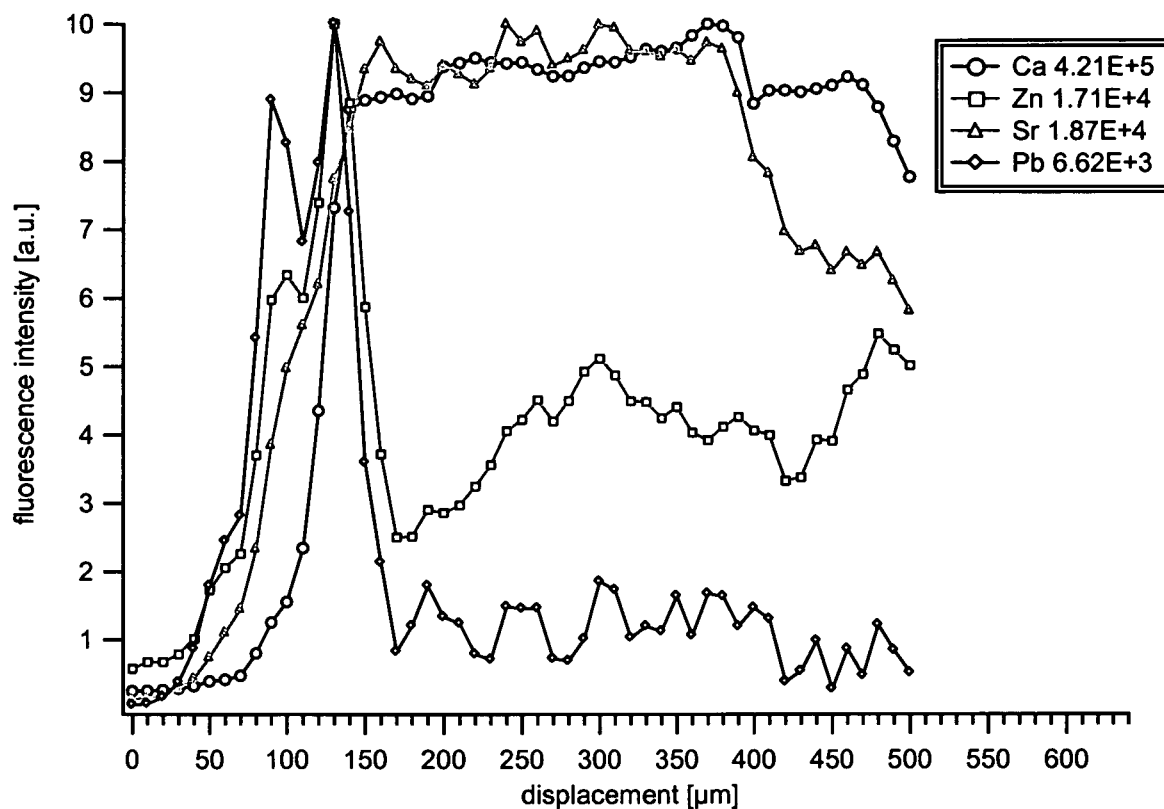


Figure 7.15: μ -XRF scan across cortical bone of a 200 μ m slice from patella. Data normalized to 100mA ring current and 100 s measuring time. Scan step width: $d=10\mu\text{m}$. For displaying the individual intensity maxima for each element are normalized to 10. Absolute values for the maximum peak counts are given in the legend

In order to define a measure for the extension of the Zn and Pb accumulating zones gaussian fitting of the peaks in the element distribution for each scan has been performed and the FWHM has been determined. If double intensity maxima were detected (Figure 7.15) each intensity peak was individually fitted. The results are summarized in table 7.1. From these calculations the mean FWHMs were determined to be $42.08 \pm 18.16\mu\text{m}$ for Zn and $37.38 \pm 12.02\mu\text{m}$ for Pb.

Sample, XRF scan	FWHM (Zn) [μm]	FWHM (Pb) [μm]
FH1,a [*]	34.21	24.96
FH2,a ^{**}	38.79	28.63
FH2,b ^{**}	50.93	46.17
FH3,a	38.18	32.79
FH3,b	35.52	28.75
FH4,a ^d	47.07	55
FH4,a ^d	79.13	48.41
P1,a ^{*,d}	24.09	37.19
P1,a ^{*,d}	31.82	26.88
P1,b [*]	26.01	37.97
P2,a ^{**,d'}	36.18	43.5
P2,a ^{**,d'}	69	
P2,b ^{**,d}	32.83	32.09
P2,b ^{**,d}	77.85	65.22
P3,a ^d	25.9	25.84
P3,a ^d	25.84	27.32
Mean width	42.08 ± 18.16	37.38 ± 12.02

Table 7.1: Gaussian fitted widths for Zn and Pb intensity peaks from scans on femoral head (FH) and patella (P). paired autopsies are marked with * and ** respectively, scans with double peaks in the Zn and Pb distribution are marked with ^d, scans with double peaks only in the Zn distribution are labelled ^{d'}

7.3.5 Conclusions

The preparation of 200 μm thick bone slices results in a significant reduction of the geometric effects and facilitates the analysis and interpretation of the measured data. Using the Ni/C multilayer monochromator instead of the Si(111) crystal provides sufficient photon flux to compensate the loss in sample mass, and therefore allows to perform $\mu\text{-XRF}$ in reasonable measuring time (10-100s per point). Interpreting data from XRF scanning on 7 bone slices from femoral head and patella with respect to BEI images of the analyzed regions it can be concluded that Zn and Pb are very inhomogeneously distributed in bones from human joints. It could be shown that Zn and Pb accumulate mostly at or around the interface between noncalcified and calcified cartilage in a zone of about 40 μm . Intensities for both elements coincide at this interface and decay rapidly within calcified cartilage to a base level in cortical bone. Since these results were observed for all samples, the data indicates a general phenomenon of Pb and Zn accumulation in the transition zone inter- and intra-individually. Although reduced, the local shift between the increase of the Ca signal and the intensities of Zn, Pb and Sr show that the geometric effects due to X-ray absorption phenomena in the

sample are still limiting factors in the interpretation of the results and complicate the correlation of fluorescence intensities to local bone regions. One way to overcome these difficulties would be the preparation of sample slices with a thickness in the range of the diameter of the beam ($15\mu\text{m}$), which is, due to the porosity the bones, not accomplishable. Therefore XRF measurements with 3D capabilities have to be performed in order to correlate the distribution of the elements with the structural features of human bone.

7.4 Confocal micro XRF on bone slices

7.4.1 Experimental setup

A schematic view and photographs of the confocal setup which has been installed at HASYLAB beamline L are shown in Figure 7.16 and Figure 7.17 respectively. The setup is based on the existing μ -XRF instrument, described in detail in paragraph 7.2.2.

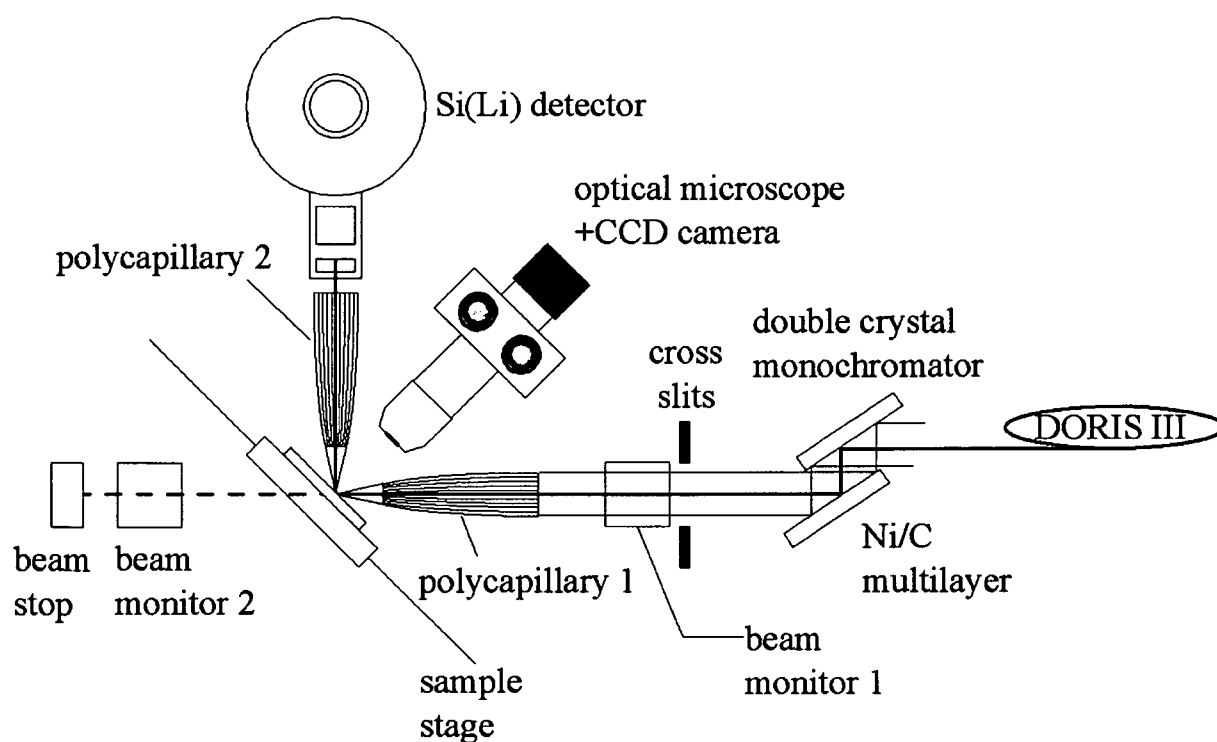


Figure 7.16: Scheme of the confocal setup at HASYLAB, beamline L

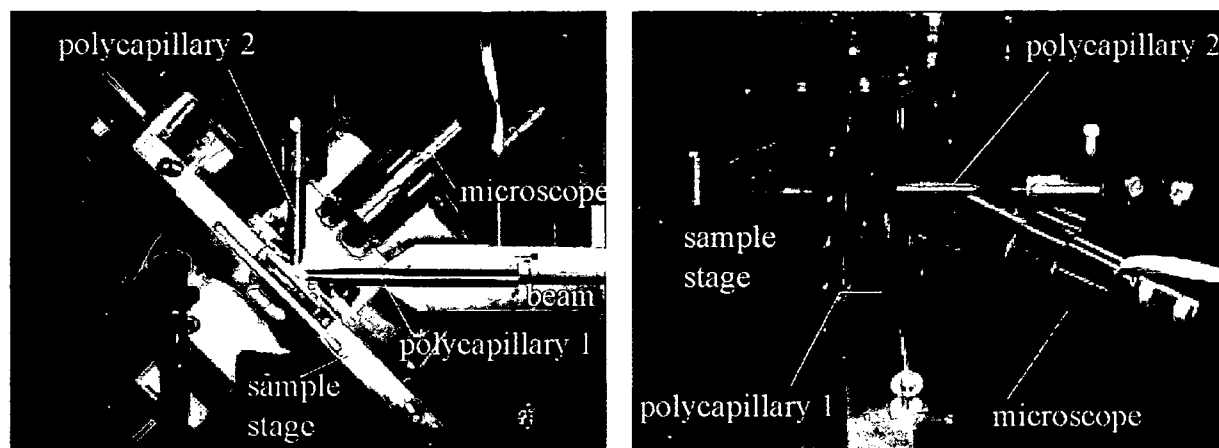


Figure 7.17: Photographs of the confocal setup at HASYLAB, beamline L.

The Ni/C multilayer was used to produce a monochromatic beam of 18keV. Two identical polycapillary half lenses (XOS, X-Ray Optical Systems, Albany, New York) arranged perpendicular to each other were used to realize the confocal setup (see paragraph 4.5). One was used to focus the primary beam, while the second optics was employed to restrict the detection volume inside the sample. The latter was directly attached to the detector snout by a plexiglass holder which was shielded by a Pb foil (see Figure 7.8). In order to be able to adjust the confocal geometry the Si(Li) detector was mounted on a motor driven XYZ table. The whole alignment procedure has been described in detail by Janssens et al. [63]. In short, after aligning the first polycapillary, the detector (with the attached capillary) was placed perpendicular to it, paying attention to distance between the sample plane and the capillary entrance. Since the two capillaries have identical dimensions and have to be aligned symmetrically to each other this first arrangement was relatively easily accomplished by manual inspection. After that, a thick sample producing sufficient fluorescence was mounted on the sample stage and moved slightly towards the microscope (~20-50 μm), to have the focus of the first capillary below the sample surface. The fluorescence signal, as recorded by the Si(Li) detector was used to find the most optimal confocal alignment. The detector was sequentially scanned for each coordinate of the table while the other two remained constant. This procedure was iteratively repeated for the three directions (XYZ) until a maximum in the inspected fluorescence line was reached.

By scanning a thin wire and a 4 μm Au foil the achieved volume was characterized to be 20 x 14 x 22 μm^3 (lateral x height x depth).

To check the energy dependence of the detection volume (see paragraph 4.5.1) the fluorescence intensities from a depth scan of a standard reference material (NIST SRM1833,

thin glass film on polycarbonate, thickness 55 μm) have been recorded and are displayed in Figure 7.18.

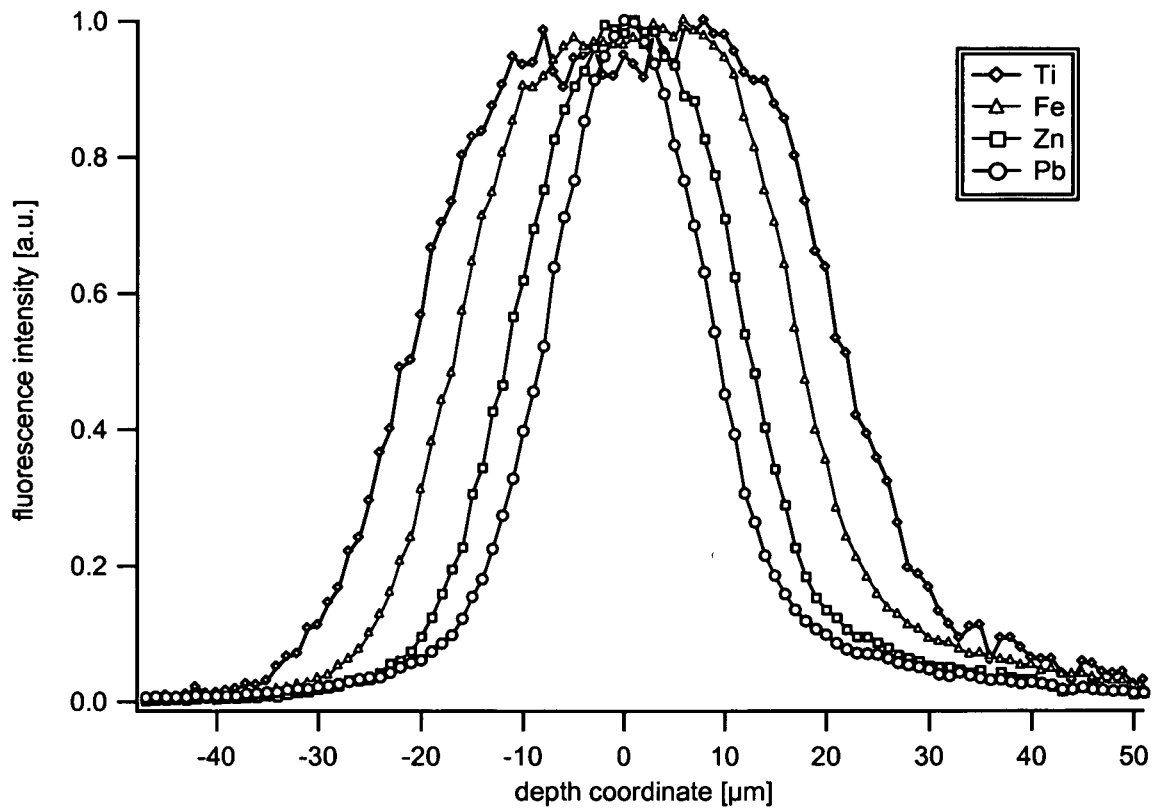


Figure 7.18: Results from a depth scan in a glass film on polycarbonate (SRM 1833). Fitted line intensities for each element are plotted against the position of the translation stage perpendicular to the focal plane of the optical microscope (depth)

Although not corrected for the thickness of the glass film, when gaussian fitting the intensity distribution for each individual element one can get an idea of the changing of the detection volume with the energy (Figure 7.19).

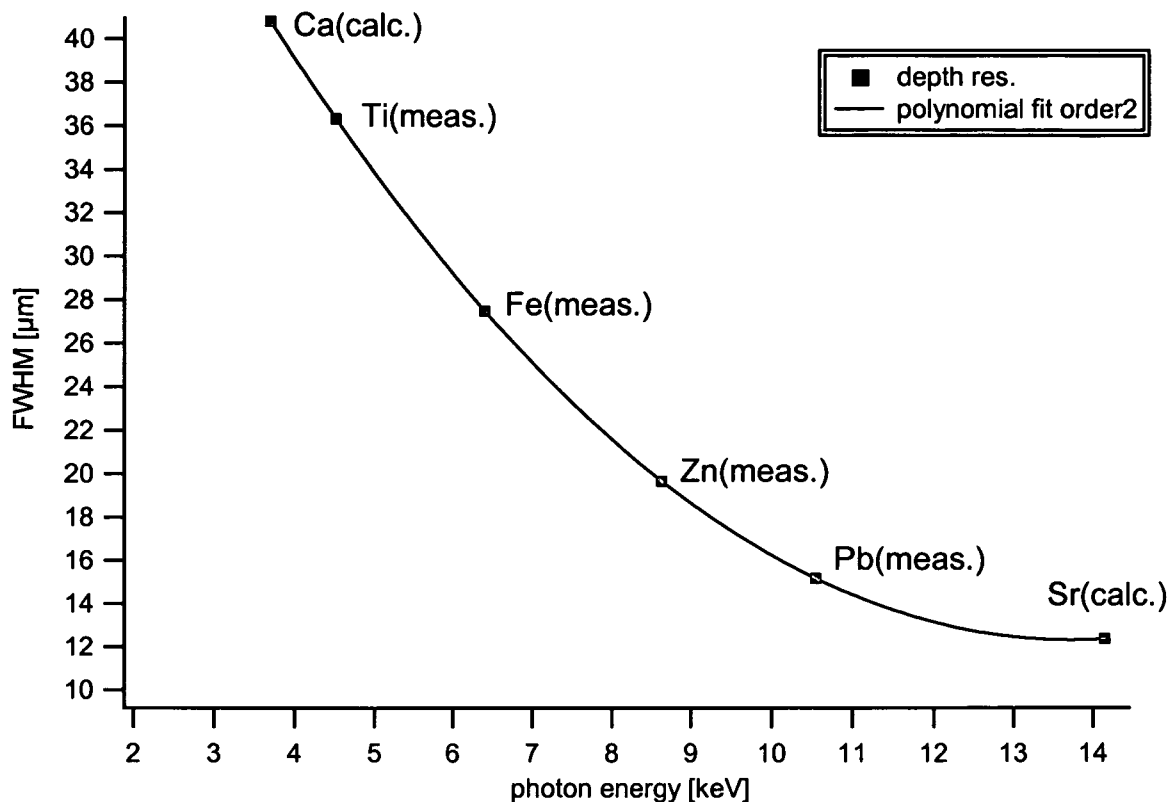


Figure 7.19: Energy dependence of the detection volume for the confocal setup at beamline L. FWHM of the gaussian fit for individual elements are plotted versus the energy of the characteristic radiation. FWHM for non measured elements have been extrapolated due to the parameters of a polynomial fit of order 2

As expected from the optical theory for X-rays (chapter 3) the analyzed volume (\sim depth resolution) shows an energy dependence, being larger for lower energies and smaller for higher energies.

7.4.2 Results and discussion

Surface near scans

Area scans in the confocal geometry have been performed on $200\mu\text{m}$ slices of femoral head and patella prior analyzed by conventional $\mu\text{-XRF}$ (see paragraph 7.3). In order to minimize self-absorption effects in the sample and to be able to correlate the information from XRF scans with the backscattered electron images, measurements have been performed at the frontal surface of the sample slices. According to the dimension of the detection volume the lateral step size was set to $10\mu\text{m}$ for each direction and typically areas of about $500 \times 500\mu\text{m}^2$ have been analyzed. Measuring time per pixel was 5s.

Results from an area scan in human patella are shown in Figure 7.20. As seen from BEI the scanned region comprised noncalcified cartilage (I), tidemark (II), calcified cartilage (III), subchondral bone (IV), cement lines(V), and a small part of trabecular bone (not seen in BEI). Comparing the intensity maps with the BEI one can see that Ca is equally distributed over the whole bone structure, showing slightly increased intensities in calcified cartilage. A similar fluorescence image is observed for Sr, but with decreased intensities in the zone of younger bone (dark gray levels in BEI, (a)), which might be a hint for a time difference between the deposition of Ca and Sr in bone tissue. In contradiction to the more or less homogeneous distribution of Ca and Sr, Zn and Pb are very inhomogeneously distributed in the bone. Comparing the results from the two imaging techniques (BEI and μ -XRF) it can be seen that Zn is mostly accumulated at demarcation lines within the bone tissue. Higher intensities are detected at the tidemark, at cement lines and at the border to bone cavities. Similar results were found for Pb. The intensity map exhibits a strong accumulation of Pb at the tidemark. In comparison to Zn, which shows almost equal fluorescence intensities at the local maxima (at the tidemark and at the cement lines), the Pb intensities at the cement lines are much less compared to the signal detected at the tidemark.

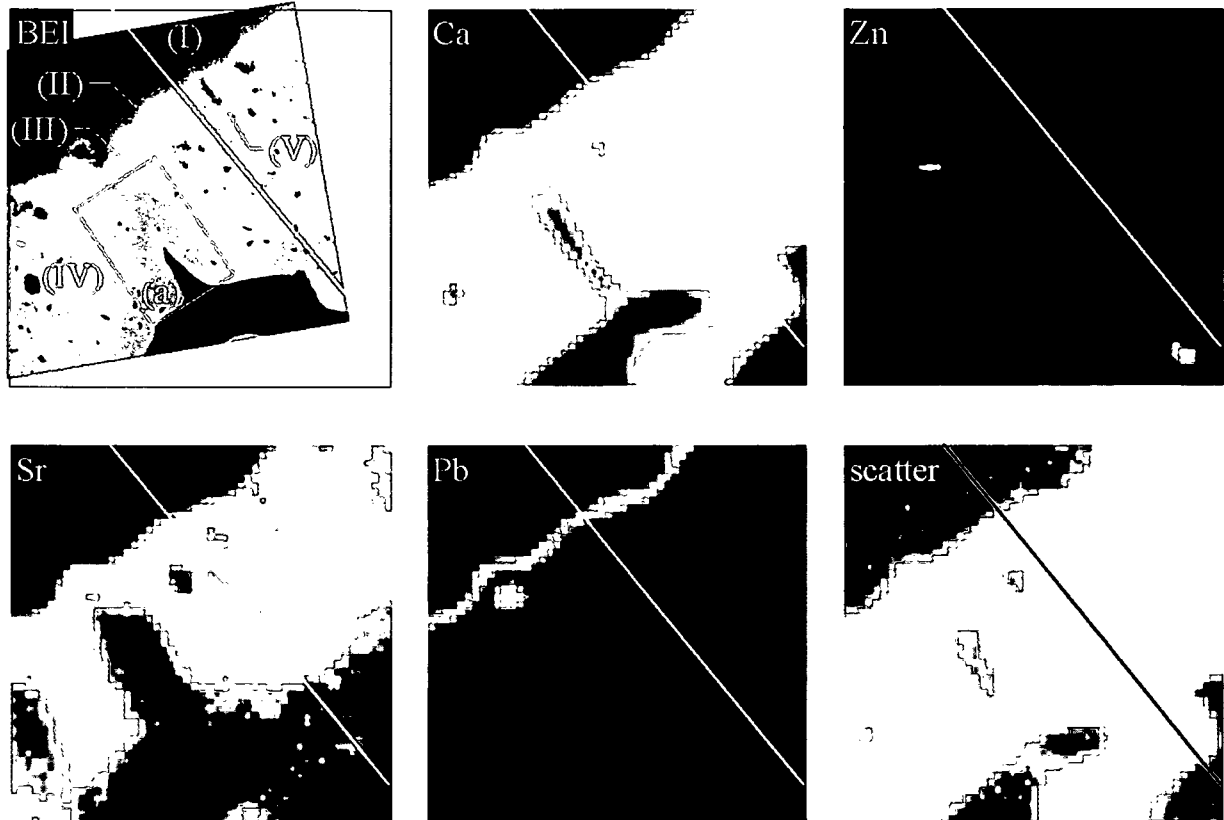


Figure 7.20: BEI and elemental maps for a slice of human patella. An area of $500 \times 500 \mu\text{m}^2$ (51×51 px) has been analyzed by confocal μ -XRF. Lateral step size was $10 \mu\text{m}$ and measuring time 5s/px . Data normalized to 100mA ring current. The scanned area (see BEI) comprised noncalcified cartilage (I), tidemark (II), calcified cartilage (III), subchondral bone (IV), and cement lines (V). A zone of young bone is (dark gray) is marked by (a). Line scan data (see Figure 7.21) has been extracted from the intensity maps by slicing the intensity array along the marked line

In order to have more precise information on the changing of the fluorescence intensity with the measurement position a line scan (Figure 7.21) has been extracted from the 3D data set (elements \times lateral position). As already seen in Figure 7.20 the intensities of Ca and Sr are slightly increased in the zone of calcified cartilage, but remain –aside from the Sr decrease at the border to the bone cavity (around position 400-500)– constant over the cortical bone. From the concurrent increase of Ca- and Sr intensities at the interface between noncalcified- and calcified tissue (position 100-150) one can see that geometric effects (due to different information depths) can be excluded, and measured differences in intensities are due to the real spatial distribution of the elements in the sample. Therefore one could definitely assign the maximum Zn and Pb intensities to the tidemark of the bone, the borderline between noncalcified- and calcified cartilage. Additionally a coincidence of the intensity maxima of Pb and Zn at the tidemark is observed. Whereas at the cement lines and at the border to bone

cavity about 80-90% of the maximum counts have been detected for Zn, for Pb this intensity ratio is much lower (about 10% at the cement line) or was not measured at all (at the cavity).

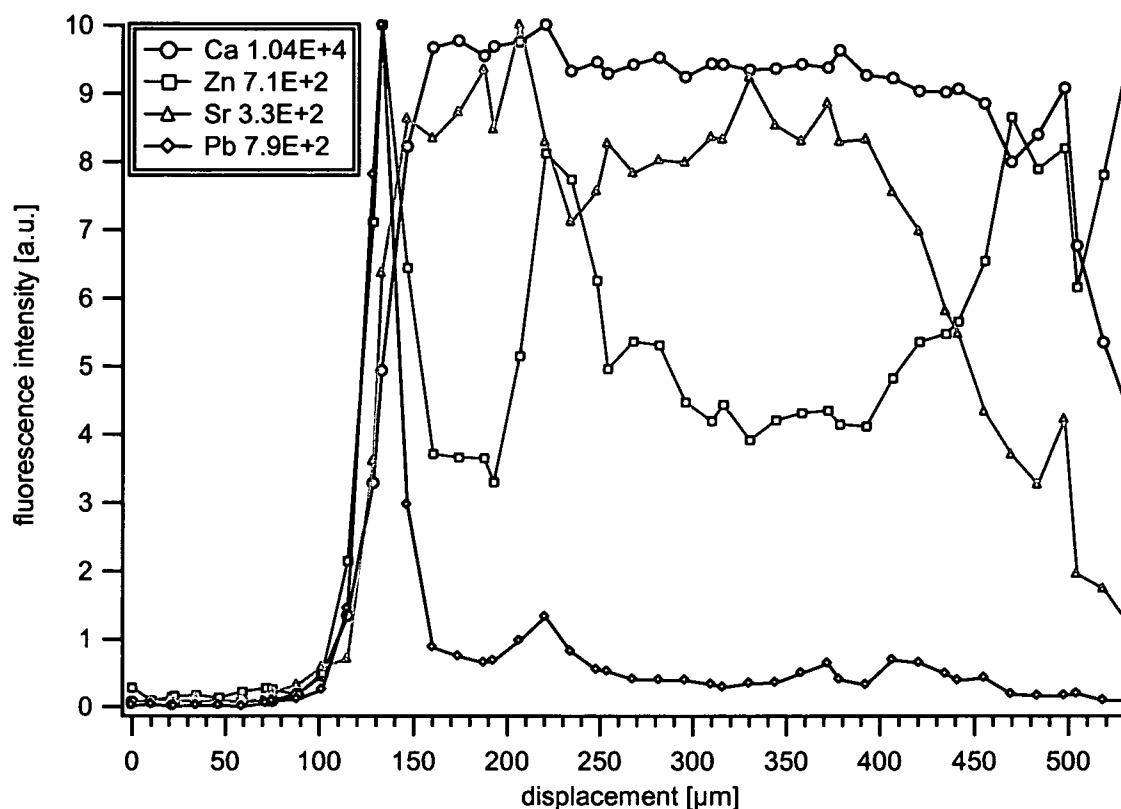


Figure 7.21: Line scan extracted from the data of an area scan in patella. For displaying the individual intensity maxima for each element are normalized to 10. Absolute values for the maximum peak counts are given in the legend

Figure 7.22 shows a comparison of a sum spectrum calculated from the whole area scan (2601 spectra) and a single spectrum at the maximum of Pb obtained in 5s measuring time. One can see the outstanding features of the confocal μ -XRF system, resulting in excellent background conditions in the fluorescence spectra. Although seen in the sum spectrum Fe was statistically distributed over the scanned area and was therefore not chosen for display. It is very likely due to residue of blood in the bone tissue.

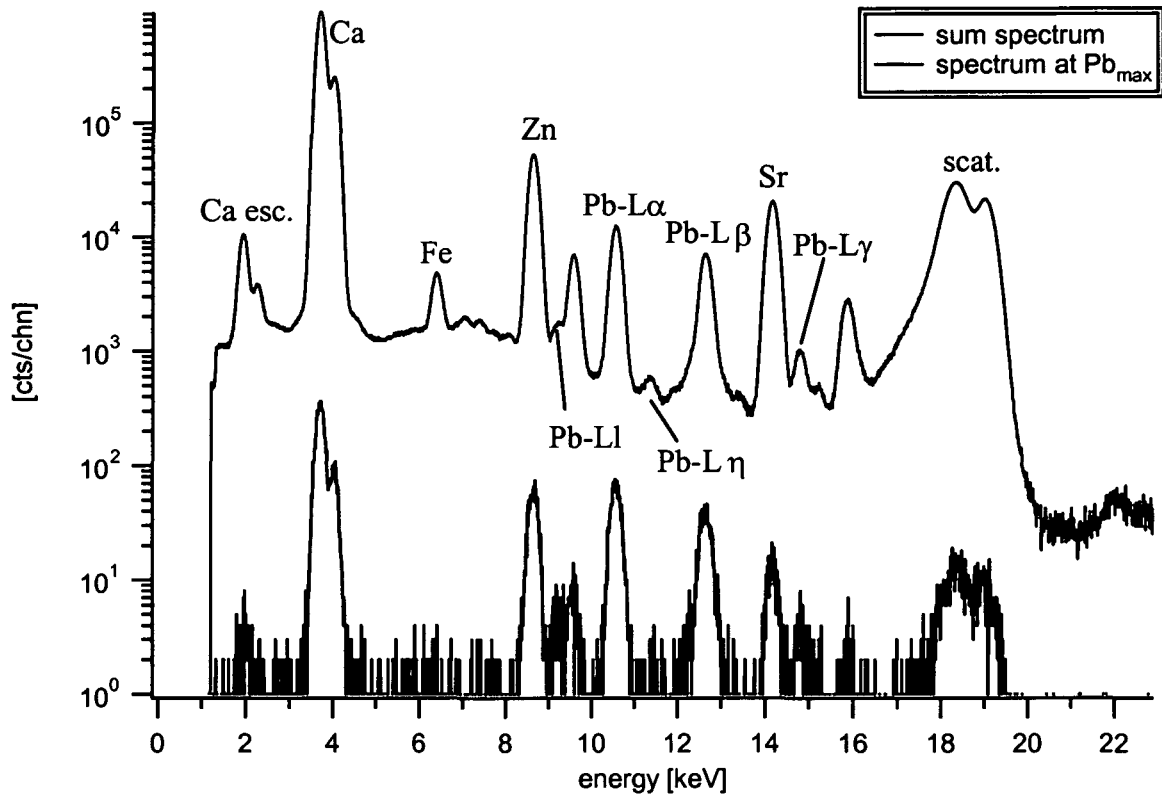


Figure 7.22: Summation of all (2601) fluorescence spectra from the area scan (red) compared with the single spectrum at the maximum of Pb (black), obtained in 5s measuring time.

Results from an area scan in femoral head and the extracted data along the line, marked in the images, are shown in Figure 7.23 and Figure 7.24 respectively. Again the region of noncalcified cartilage, calcified cartilage and subchondral bone has been analyzed. In comparison to the patella sample (Figure 7.20), the femoral head showed a double tidemark within the scanned region. Both tidemarks –the first and the second one- are labeled (IIa) and (II) in the BEI. Although low in contrast in the gray-scale image, the first tidemark (IIa) appears as a sharp line in the middle of calcified cartilage (III), while the second tidemark (II) is clearly presented as a frayed interface between noncalcified and calcified tissue. Since the backscattered electron images provide information about the degree of calcification, one can see that the first tidemark (IIa) was fully developed at the time of extracting the sample, while the second was still under construction when the calcification was abandoned due to death of the subject. Therefore, according to the time of formation, the tidemarks are from now on denoted older (IIa) and younger (II) tidemark.

While Ca and Sr (compare with Figure 7.20 and 7.21) are again almost homogeneously distributed in calcified tissue, a different behavior can be seen for Zn and Pb. From the results obtained from the scan in patella one would expect increased intensities for both

elements at the older- as well as at the younger tidemark. However such a distribution is found for Zn, this is not the case for Pb. Pb shows a strong accumulation at the older tidemark, while it is not present at the younger tidemark. These results are either to be explained by a time difference in the accumulation of Zn and Pb at the calcification front (tidemark) or by a reduced Pb content in the organism when the younger tidemark was formed.

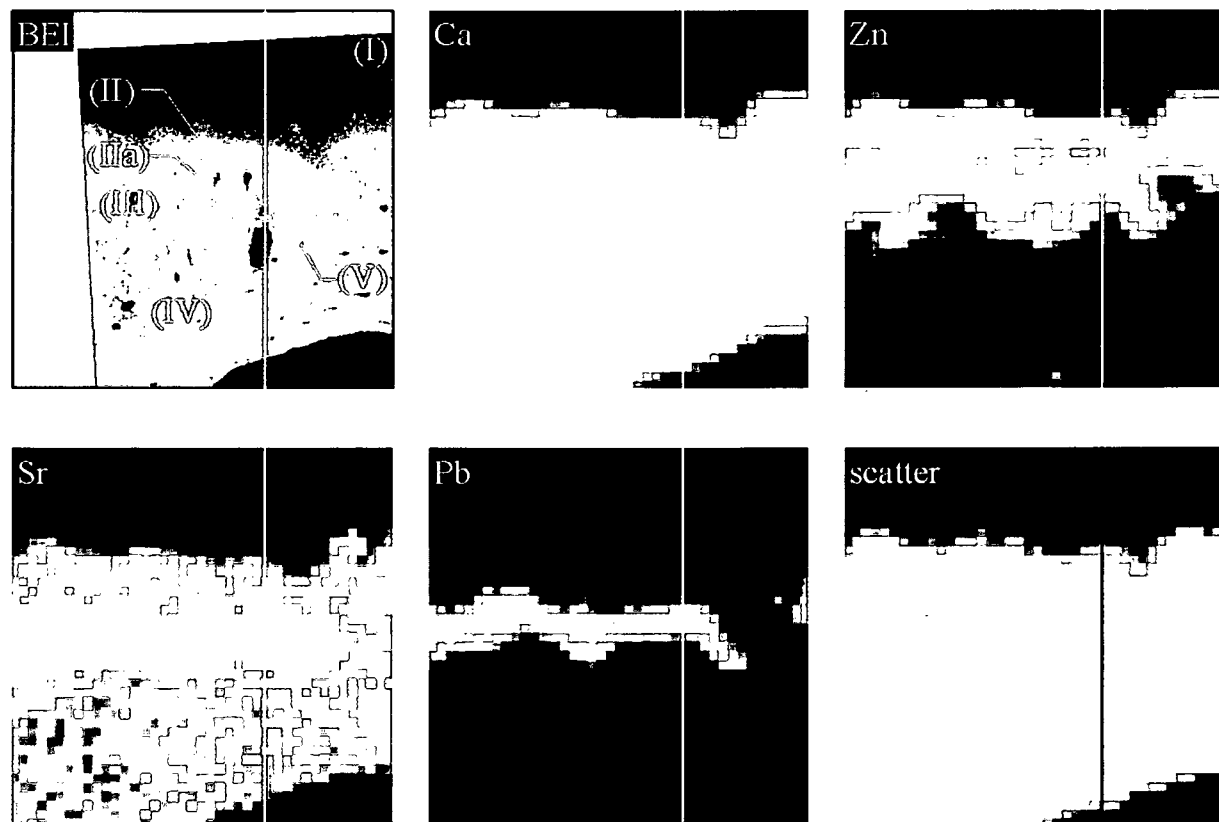


Figure 7.23: BEI and elemental maps for a slice of femoral head. An area of $500 \times 500 \mu\text{m}^2$ (51×51 px) has been analyzed by confocal μ -XRF. Lateral step size was $10 \mu\text{m}$ and measuring time $5\text{s}/\text{px}$. Data normalized to 100mA ring current. The scanned area (see BEI) comprised noncalcified cartilage (I), a younger (II) and an older (IIa) tidemark, calcified cartilage (III), subchondral bone (IV), and cement lines (V). Line scan data (see Figure 7.16) has been extracted from the intensity maps by slicing the intensity array along the marked line

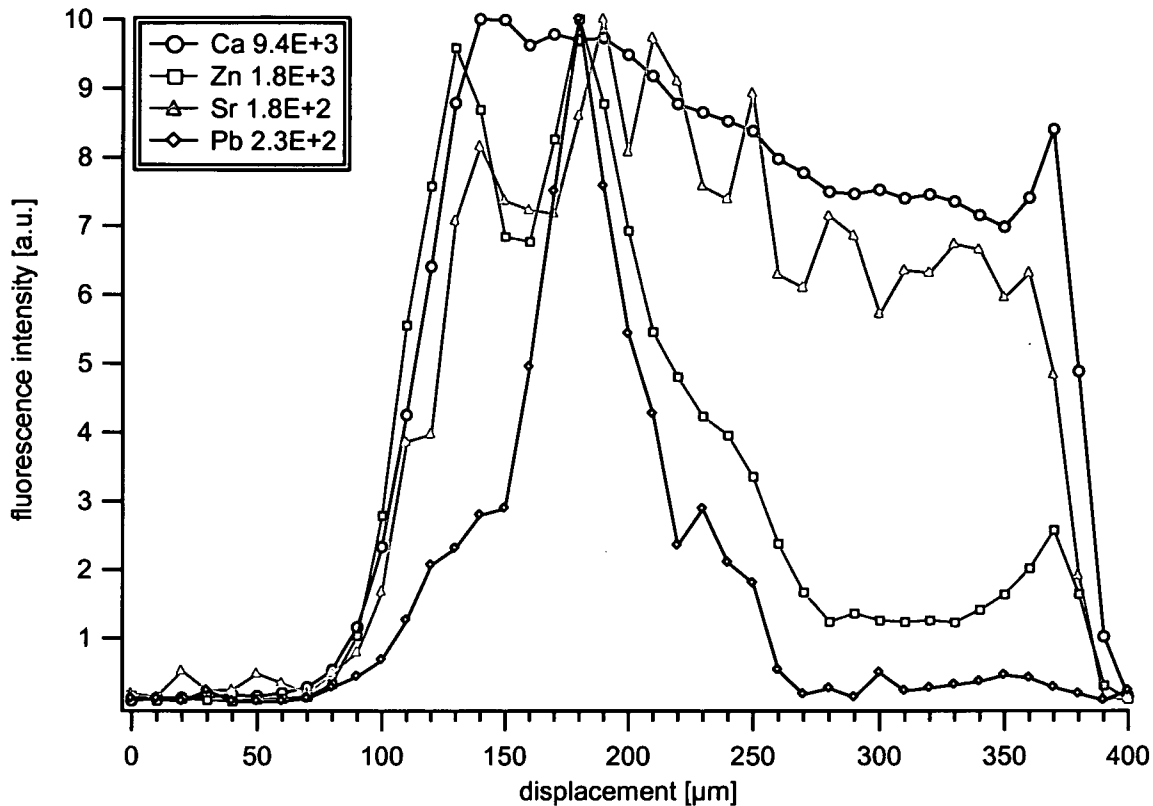


Figure 7.24: Line scan extracted from the data of an area scan in femoral head. Maximum intensities are normalized to 10 for each element. Absolute values of the maximum intensities are given in the legend

3D scan

To demonstrate the 3D capabilities of the applied confocal μ -XRF method the elemental distribution in a patella sample has been studied in a sample volume of $200 \times 200 \times 160 \mu\text{m}^3$ (left/right \times up/down \times depth). Step size for each direction to $10 \mu\text{m}$, and each voxel was measured for 5s. A optical microscope image of the frontal surface of the bone slice is shown in Figure 7.25. As for the surface near scans noncalcified cartilage (I), tidemark (II), calcified cartilage (III) and a small part of subchondral bone (IV) have been analyzed. The net intensities for each element have been determined from the 7497 ($21 \times 21 \times 17$) fluorescence spectra by automatic peak fitting (QXAS-AXIL, batch mode) and were converted to 8-bit grayscale images for each measured slice in depth. From these images element specific (different colors) 3D volumes have been rendered using a visualization software, designed for tomographic imaging (Figure 7.26). While the Ca signal decreases rapidly with depth (self absorption of the sample), Sr as well as the coherently scattered peak (18keV) exhibit nicely the irregular sample shape at the interface between noncalcified and calcified tissue. The results for Zn and Pb show the three-dimensional analogue for what was already seen from line- and area scanning. Maximum intensities at the tidemark, and to some extend a

correlation between Zn and Pb. With this 3D experiment it was possible to show that the accumulation of Zn and Pb is not a surface effect, which might have been introduced by sample preparation.

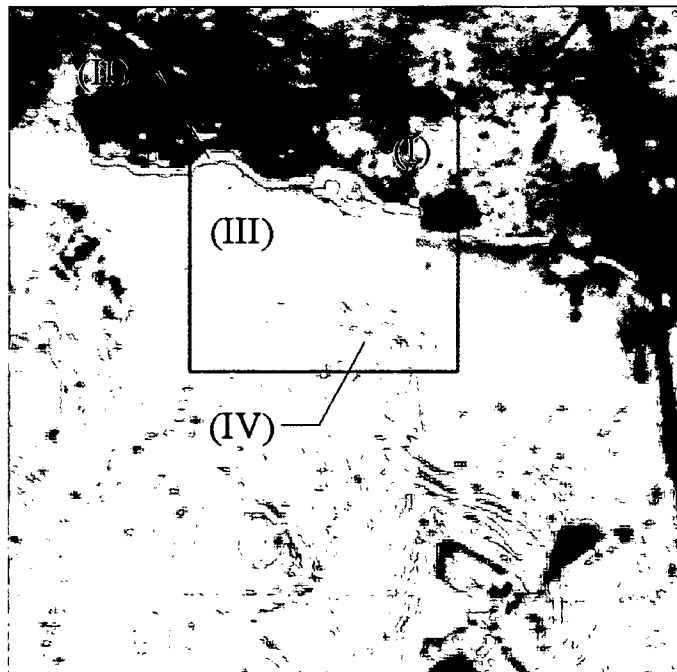


Figure 7.25: Optical microscope image of the frontal surface of the analyzed patella. The san area is marked by the red frame. Noncalcified cartilage (I), tidemark (II), calcified cartilage (III), and subchondral bone can be clearly distinguished. Scanned volume: $200 \times 200 \times 160 \mu\text{m}^3$, step size $10 \mu\text{m}$ each, measuring time 5s/point.

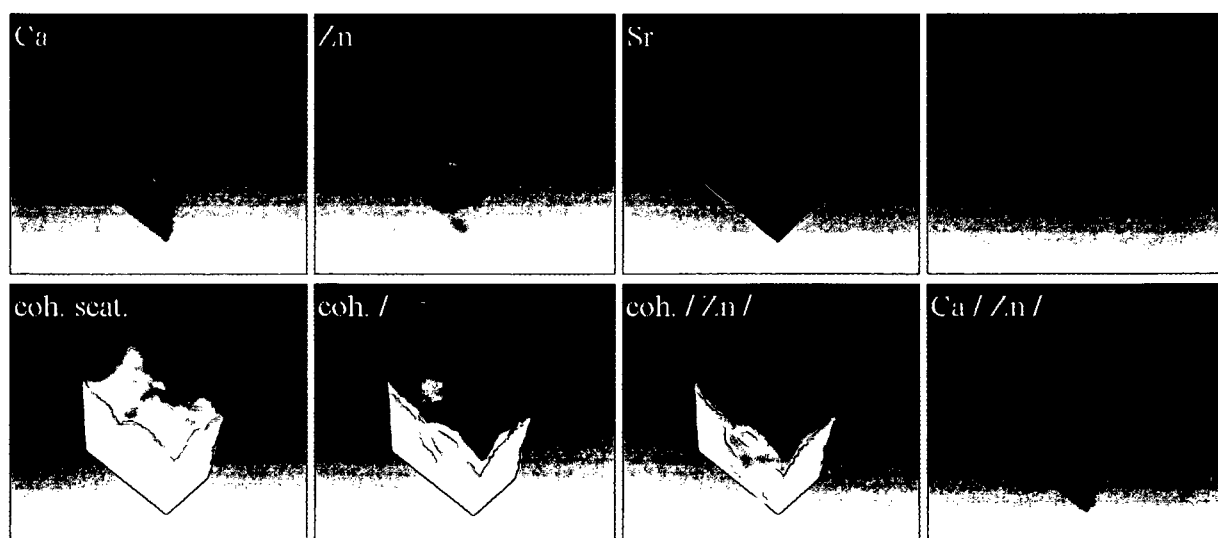


Figure 7.26: Three-dimensional element distribution in human patella

7.4.3 Conclusions

Since, due to porosity of the sample no sample slices thinner than 200 μm could be prepared, a measurement technique with 3D capabilities had to be applied to eliminate geometric effects caused by the sample thickness. This was accomplished by performing $\mu\text{-XRF}$ in the confocal mode, where a second capillary is used to restrict the field of view of the energy dispersive X-ray detector. It could be shown, that the combination of two focusing optics and high flux synchrotron radiation is perfectly suited to determine the distribution of trace elements (Pb) in human bone with sufficient spatial resolution. As a result it was found that Pb and Zn preferably accumulate at demarcation lines within bones from human joints. Especially the tidemark –the interface between noncalcified and calcified cartilage- seems to play an important role in the accumulation mechanisms. While for Zn the detected intensities were almost the same for cement lines and tidemarks, Pb intensities were about an order of magnitude higher at the tidemark compared to cement lines. In case of duplicated tidemarks two Zn intensity maxima (one at each tidemark) were found whereas high intensities of Pb were only detected at the older of both. This effect might be explained either by a time difference between the accumulation of Zn and Pb, or by a reduced Pb content in the organism when the younger tidemark was formed. By combining lateral and in depth scanning it was possible to obtain a three-dimensional elemental distribution in human bone, proofing that the accumulation of Zn and Pb is not a surface effect.

7.5 Absorption tomography of cortical bone

Besides confocal $\mu\text{-XRF}$, X-ray absorption tomography was exploited to examine the bone cartilage interface (tidemark). Although not element specific this method provides an insight on the structural changes of the calcified tissue within the sample depth, not seen under the microscope or with BEI. Furthermore it helps to gain an idea of the complexity of the tidemark, resulting in the geometric effects, described in the previous chapters.

7.5.1 Experimental setup

Measurements have been carried out at IAEA Seibersdorf Laboratories, Seibersdorf, Austria. A schematic view of the used scanning XRF micro-tomography spectrometer [89] is shown in Figure 7.27. The focused microbeam was produced by a high power X-ray tube (3kW, Mo anode, long fine focus) and a tapered single glass capillary with an exit diameter of about 10

μm . Since the divergence of the beam is much less than it would be after focusing with a polycapillary lens, the single capillary is perfectly suited for tomography measurements, where an almost parallel beam is required. The lens was attached to the X-ray tube by a gimbal mount, allowing all necessary movements for manual adjustment of the optics. The sample was mounted on a motorized XYZ/ θ translation/rotation stage with a compact XY stage (for manual wobbling correction) on top, allowing to perform lateral scans of the sample as well as sample rotation. The system was equipped with a Si(Li) semiconductor detector for recording the fluorescence radiation and a fast silicon drift detector (SDD) to collect the transmitted photons. For controlling the sample position a light optical microscope coupled to a CCD camera was attached to the spectrometer. As seen from Figures 7.27 and 7.28, the fluorescence detector was mounted perpendicular to the incident beam and the microscope along the bisecting line of the angle between beam and detector. To correct for the tube take-off angle, the tube (with attached capillary), the sample stage and the SDD were mounted on optical rail inclined by 6° (see Figure 7.28 (a)). The data acquisition system consisted of 2 multichannel analyzers for collecting transmitted-, fluorescence photons and a dedicated software package (SPECTOR-LOCATOR [90]).

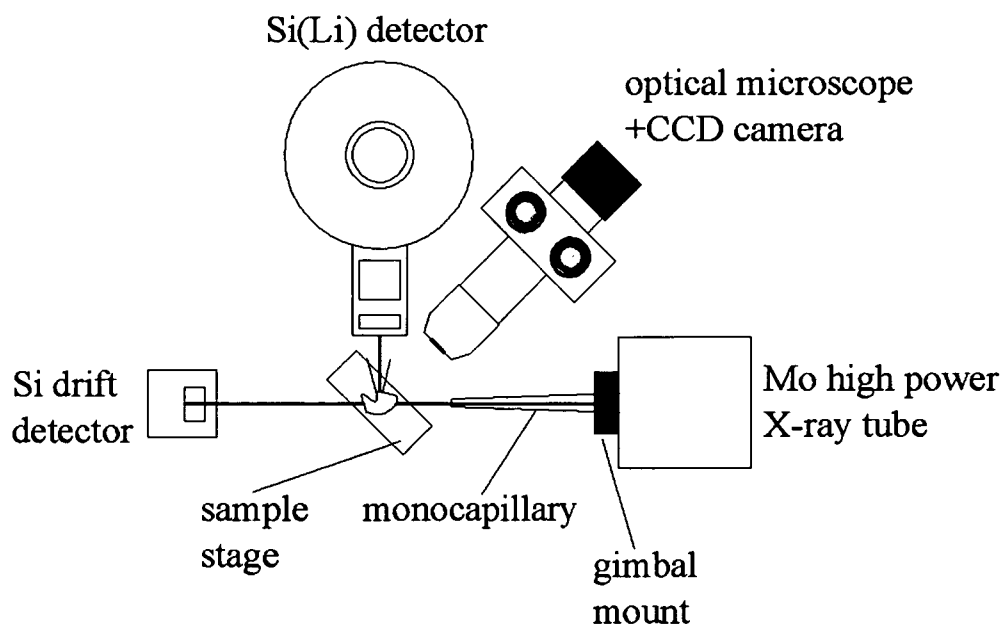


Figure 7.27: Schematic view of the micro-tomography setup at IAEA Seibersdorf Laboratories, Seibersdorf, Austria

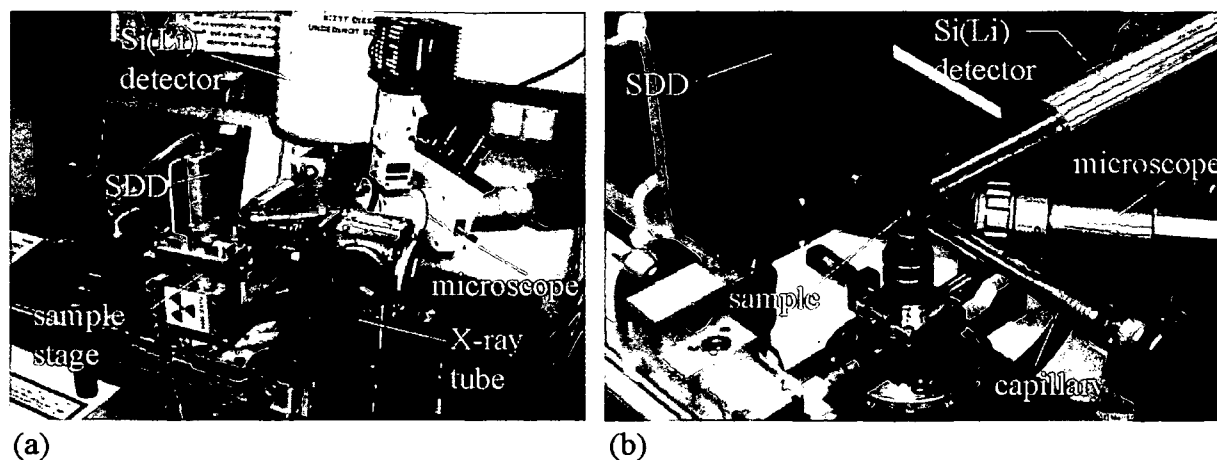


Figure 7.28: Overall view (a) of the used system and close up of the sample stage (b) showing the capillary tip, the snout of the Si(Li) detector, the SDD and the sample stage with the manual XY stage for wobbling control on top

7.5.2 Samples / sample preparation

A sample suitable for tomography (quadratic cross-section) was produced from a 200 μm slice of prior embedded (see paragraph 7.3.2) human patella. A piece containing noncalcified- and calcified cartilage, tidemark as well as subchondral bone has been extracted. By low speed diamond saw cutting the size of the rather large sample ($\sim 1.5\text{cm} \times 1.5\text{cm} \times 200\mu\text{m}$) has been reduced to dimensions of about 2mm x 4mm x 200 μm . After that the remaining piece was clamped between two panels of plexiglass and grinded to a size of 300 $\mu\text{m} \times 4\text{mm} \times 200\mu\text{m}$ (Figure 7.29). Before gluing the specimen to a thin graphite tip, the sample was rinsed with pure alcohol. Sample preparation has been done by E. China-Cano, IAEA Seibersdorf Laboratories, XRF Group, Instrumentation Unit.

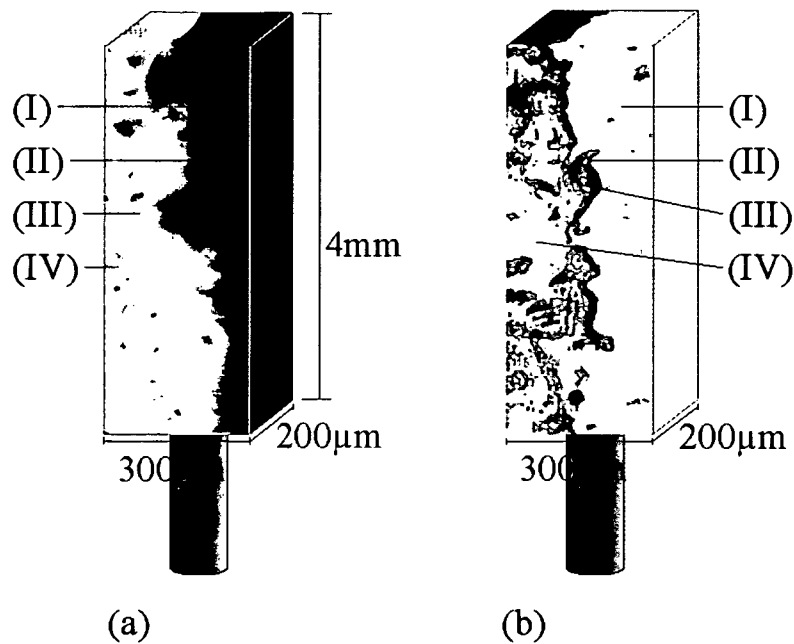


Figure 7.29: Sample preparation for tomography. BEI (a) and light optical microscope image (b). The patella sample contained noncalcified cartilage (I), tidemark (II), calcified cartilage (III) and subchondral bone (IV).

7.5.3 Results

X-ray absorption data for the patella sample has been measured using the above described micro-tomography system at Agency's Laboratories Seibersdorf, Austria. Sinograms for 31 object slices have been recorded at 128 lateral positions and 128 different angles from 0 to 180°. The distance between the slices was chosen to be 23 μm , the horizontal step width was set to 10 μm and the angle increment was 1.4°. Measurement time for each of the 507904 (128 x 128 x 31) pixels has been set to 0.1s resulting in a total measuring time of about 2.5 days (including deadtime and time for motor movement).

The sinograms for each slice have been exported with the SPECTOR-LOCATOR software and the reconstruction has been done by a self programmed software (Figure 7.30), developed under the Lab VIEW 6.1 environment. After reconstruction the data (8-bit gray-scale images) was used to create a three-dimensional absorption image of the scanned sample volume.

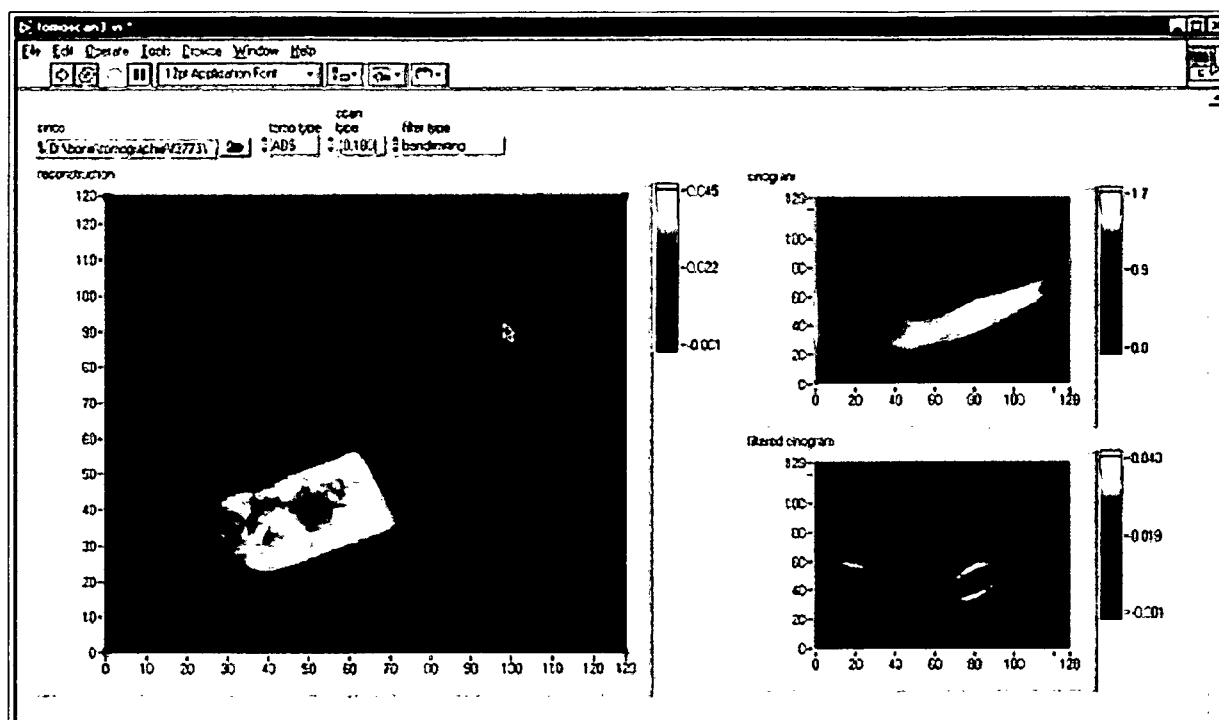


Figure 7.30: Screenshot of the backprojection software for tomographic imaging. The reconstruction as well as the unfiltered and filtered sinogram can be seen.

Figure 7.31 shows the results from the absorption tomography scan. As seen from the reconstruction of a single object slice (Figure 7.31 (b)) it is not possible to distinguish between calcified cartilage and subchondral bone, indicating that the linear absorption coefficient is equal and the Ca content is comparable for both compartments. Since there was no increased absorption detected at the interface between noncalcified and calcified tissue confirms the assumption that the Pb content in the tidemark is on the trace element level, very likely not detectable with standard XRF spectrometers, using X-ray tube spectra (Bremsstrahlung and characteristic radiation) for excitation. From the reconstructed sample volume (Figure 7.31 (a)) one sees the complex, three-dimensional structure of the tidemark which makes the establishment of a correction model for quantification almost impossible.

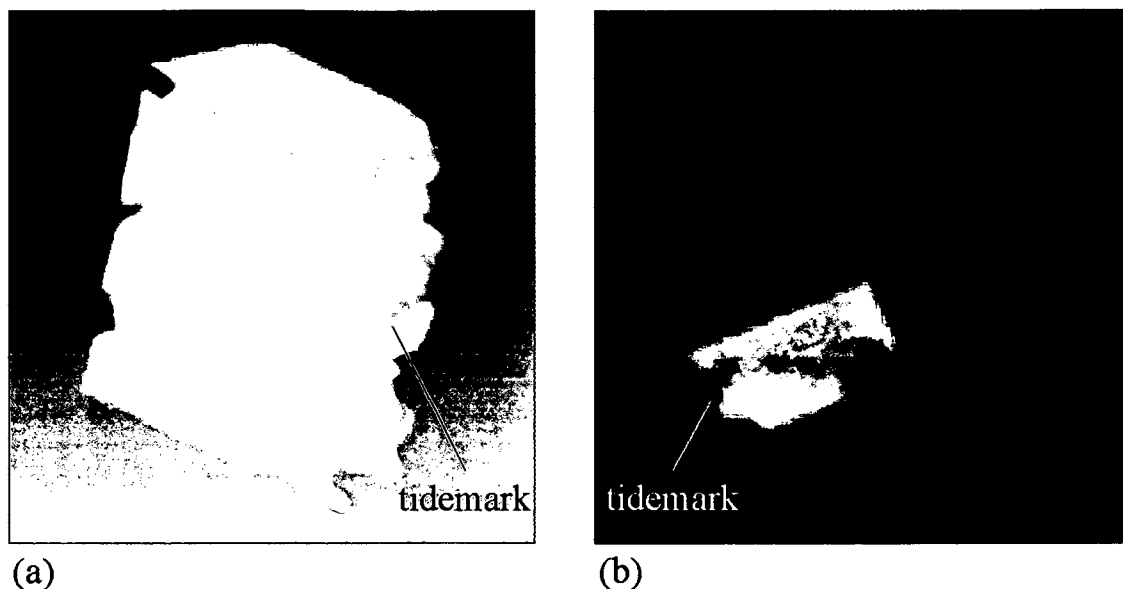


Figure 7.31: Reconstructed sample shape from absorption measurements in tomographic mode. The fully reconstructed 3D volume (a) and one object slice (b) are shown

7.6 Combined fluorescence-absorption tomography of cortical bone

In order to gain information on the elemental distribution in depth of a bone sample, a single object slice from the patella, previously measured in absorption tomographic mode (paragraph 7.5) has been analyzed by fluorescence tomography. Direct results, as well as intensity distributions corrected for self absorption in the sample will be presented in this paragraph.

7.6.1 Experimental setup

Measurements have been carried out in cooperation with D. Wegrzynek and E. Chinea-Cano, IAEA Seibersdorf Laboratories, XRF Group, Instrumentation Unit at the Fluo-Topo beamline at ANKA, Karlsruhe, Germany. The micro-tomography system (see paragraph 7.5.1) has been set up at the Topo hutch of the beamline (Figure 7.32). A W/B₄C multilayer monochromator was used to provide a monochromatic synchrotron X-ray beam at 16.5 keV. Focusing of the beam (beamsize about 5 μm) was performed by means of a compound refractive lens, offering the required pencil-beam geometry for x-ray fluorescence μ-tomography. A fast silicon drift detector (SDD) allowing acquisition at high count rates was placed behind the sample to collect photons from the transmitted beam. In order to make optimal use of the polarization of the synchrotron beam a Si(Li) semiconductor detector for recording the fluorescence photons was mounted in the orbital plane perpendicular to the incoming beam. The samples were

mounted on a XYZ θ translation/rotation stage, allowing to perform lateral scans of the sample as well as a sample rotation by 360° necessary for fluorescence tomography. The data acquisition system consisted of 3 multichannel analyzers for collecting transmitted photons, fluorescence photons and monitoring the incident beam (ionization chamber).

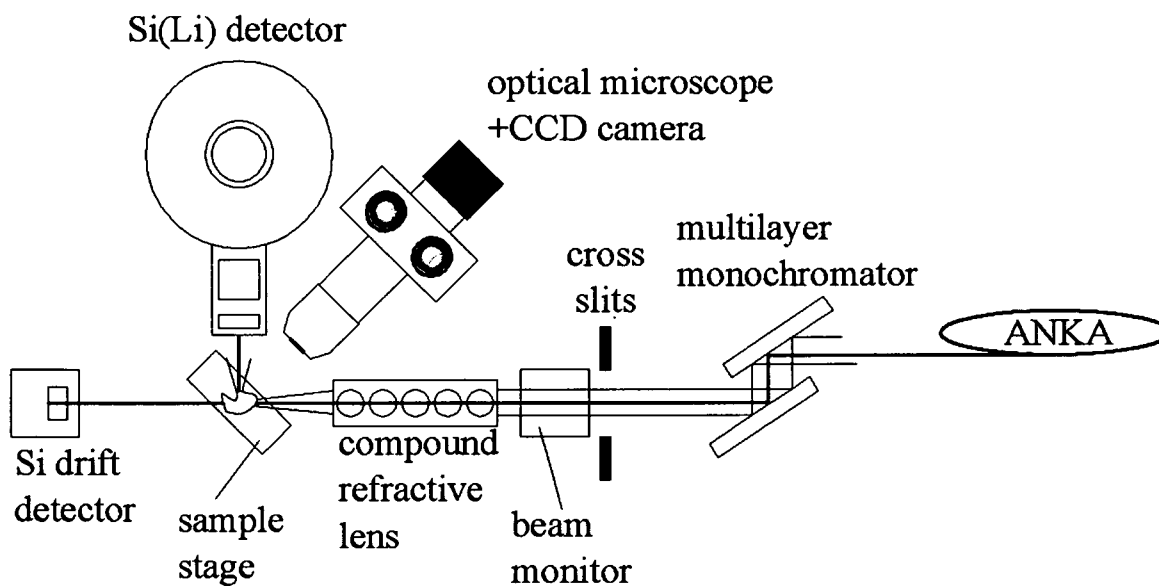


Figure 7.32: Schematic view of the μ -tomography setup at ANKA.

7.6.2 Results

X-ray fluorescence and X-ray absorption sinograms for a slice of the patella sample have been simultaneously recorded measuring equidistant (step size = 15.2 μ m) lateral points at 64 angles between 0° and 360° (angle increment = 5.6°). While the measuring time for the fluorescence detector was set to 5s per pixel the acquisition time for the transmission detector and the beam monitor was chosen to be 3s. From the fluorescence intensities, obtained by automatically fitting the 4096 spectra (Figure 7.33), flux normalized sinograms have been created for each element by an adopted version of the software already used for absorption tomography.

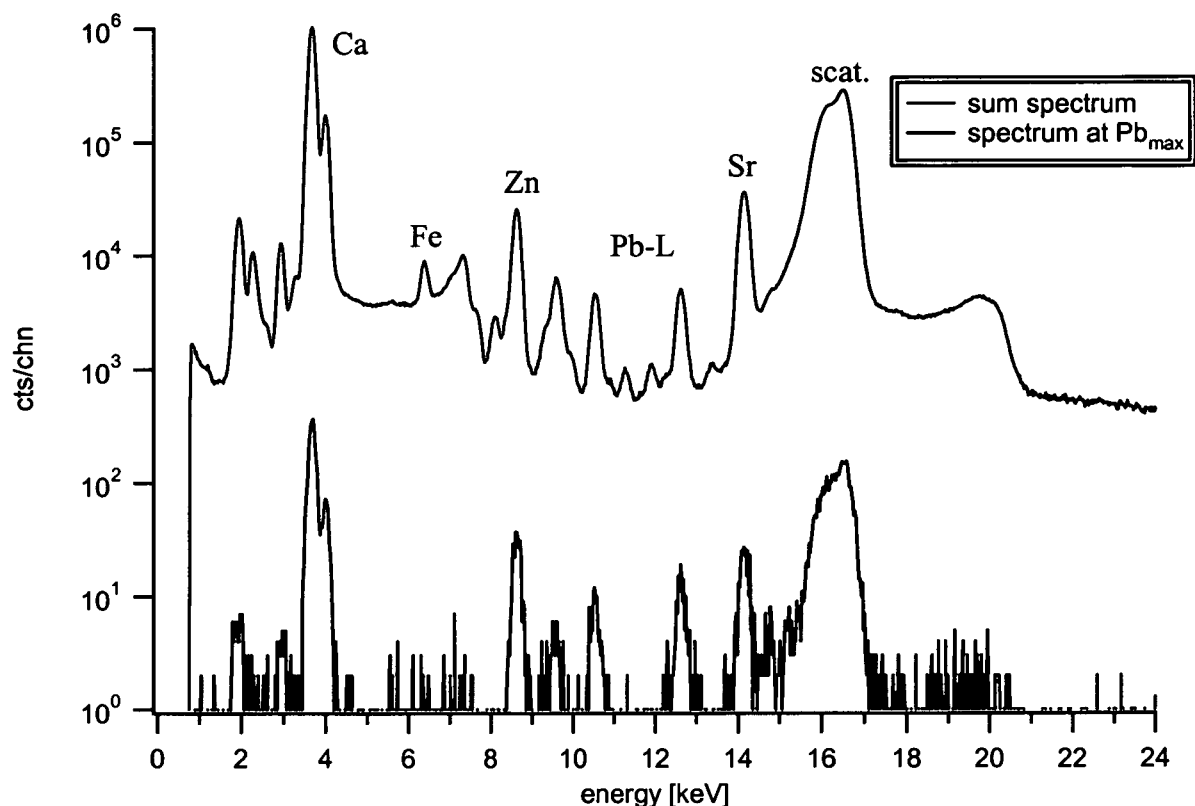


Figure 7.33: Sum spectrum (red) and spectrum at the position of maximal Pb intensities (black) as recorded by the fluorescence detector during a tomographic scan.

The reconstructed, element specific images of the analyzed object slice are shown in Figure 7.34. The sample shape can be nicely determined from the image gained from data for Sr, scattered radiation and transmission data. As one can see, the Ca photons originating in the inner part of the specimen are heavily absorbed by the sample itself and therefore represent only the edges of the analyzed bone. Increased intensities for Zn and Pb are restricted to small zones of the bone, which is in good agreement with the results obtained with confocal μ -XRF. Since, for these type of measurements the comparison with data from other imaging techniques, such as backscattered electron imaging, can not be done, it is not possible to directly assign the regions of Zn and Pb accumulation to the tidemark of the bone.

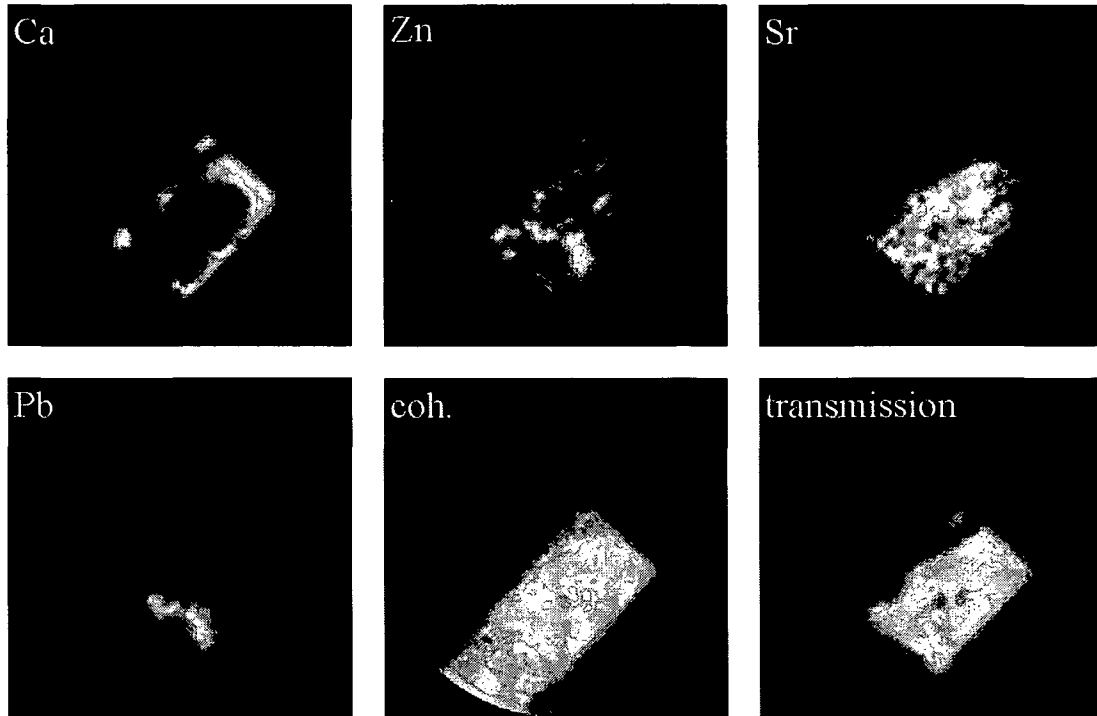


Figure 7.34: Reconstructed, element specific images from a fluorescence tomography scan. Within the reconstruction circle some artifacts are seen due to the discrete number of measured points per angle

Absorption correction

To make first attempts to get fluorescence images corrected for self absorption in the sample a simplified absorption correction algorithm [91] has been applied, and explained with respect to Figure 7.35 (schematic view of the tomographic measurement).

A parallel micro beam of incident energy E_0 impinges on a sample which dimensions are suitable for combined absorption and fluorescence tomography. The size of the sample has to be chosen in a way, to have enough contrast for the absorption measurement and to be smaller than the diameter of the fluorescence detector. If this demand is fulfilled, it is guaranteed that sufficient data for the absorption correction can be recorded and all fluorescence photons generated along the path of beam interaction are measured.

Let N be the number of lateral measurement points and let us assume, that the beam impinges at the i^{th} position, with $0 \leq i \leq N$. Due to the sample size and the distance between sample and detector the fluorescence radiation might be considered as rays parallel to the detector axis and the absorption in air might be neglected. If the microbeam propagates through the sample at any position $i \neq N$ a fluorescence intensity I_f reduced due to self absorption on the path to the detector is measured. Therefore the corrected fluorescence intensity I_f^* can be written as

$$I_f^* = F * I_f \quad (7.1)$$

where F is the self absorption correction factor. Since the sample is very small (200-300 μ m) in size, F can be expressed from the approximation for intermediate thick samples as

$$F = \frac{(\mu\rho d)^*}{1 - \exp(-(\mu\rho d)^*)} = F_1 + F_2 \quad (7.2)$$

where $(\mu\rho d)^*$ describes the absorption of the primary beam (F_1) as well as the absorption of the fluorescence radiation (F_2) on the way to the detector. For measurement of the sample at a given angle θ and a position i the absorption of the primary beam is directly recorded by the absorption detector and can be written as

$$F_{1,i} = \ln\left(\frac{I_0}{I_i}\right)_{Abs,\theta} \quad (7.3)$$

The term for the direction perpendicular to the incident beam (to the fluorescence detector) is calculated from the absorption data recorded at the angle $\theta + 90$ by

$$F_{2,i} = \left(\frac{N-i}{N}\right) * \frac{\sum_{k=1}^N \ln\left(\frac{I_0}{I_k}\right)_{Abs,\theta+90^\circ}}{N} \quad (7.4)$$

As seen in equation (7.4) an average absorption for the sample is calculated from the projection data and is weighted by the number of measurement points between the actual measurement position and the sample edge. Combining equations (7.3) and (7.4) one gets

$$F_i = F_{1,i} + F_{2,i} = \ln\left(\frac{I_0}{I_i}\right)_{Abs,\theta} + \left(\frac{N-i}{N}\right) * \frac{\sum_{k=1}^N \ln\left(\frac{I_0}{I_k}\right)_{Abs,\theta+90^\circ}}{N} \quad (7.5)$$

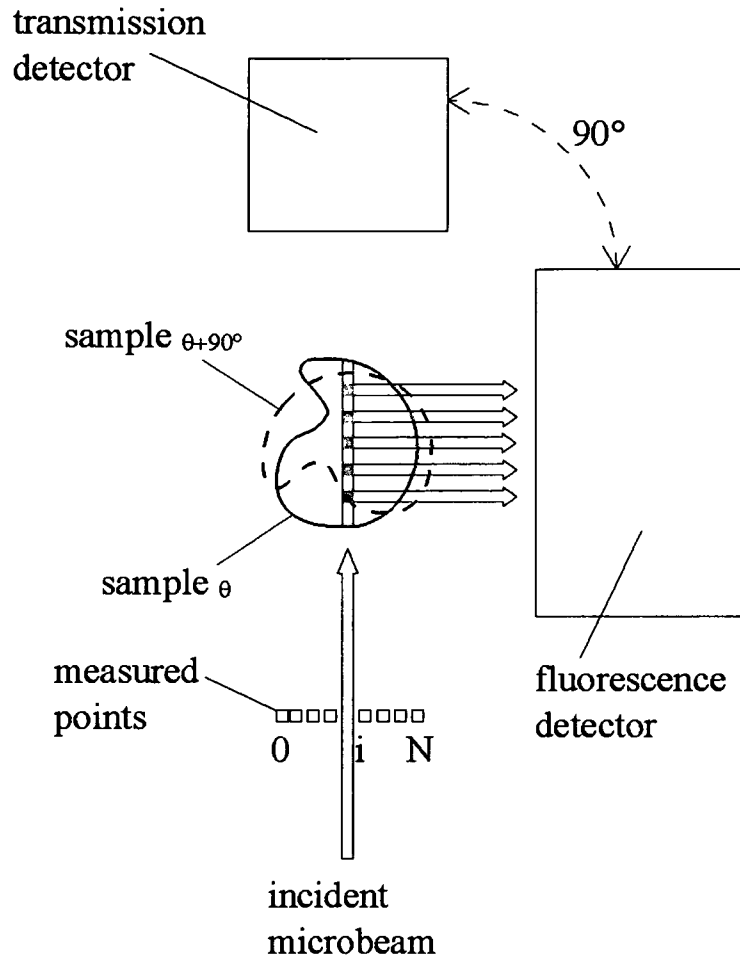


Figure 7.35: Typical setup for combined absorption and fluorescence tomography

From equation (7.5) an self absorption coefficient F can be calculated only for the energy E_0 of the incident photons. While this could be used to correct the reconstruction from the scattered radiation, in case of the fluorescence images an energy correction has to be applied. Calculating the absorption coefficient for the standard reference material of cortical bone [ICRU] for different concentrations of the main constituent Ca (Figure 7.36) one can see that although the absolute μ/ρ values change, the slope of the curves remain constant. In a first approximation this effect is used to scale F_2 in equation (7.5) from E_0 to the energy E_i of the interested fluorescence photons, leading to an $E^{-2.8}$ correction according to Bragg-Pierce law.

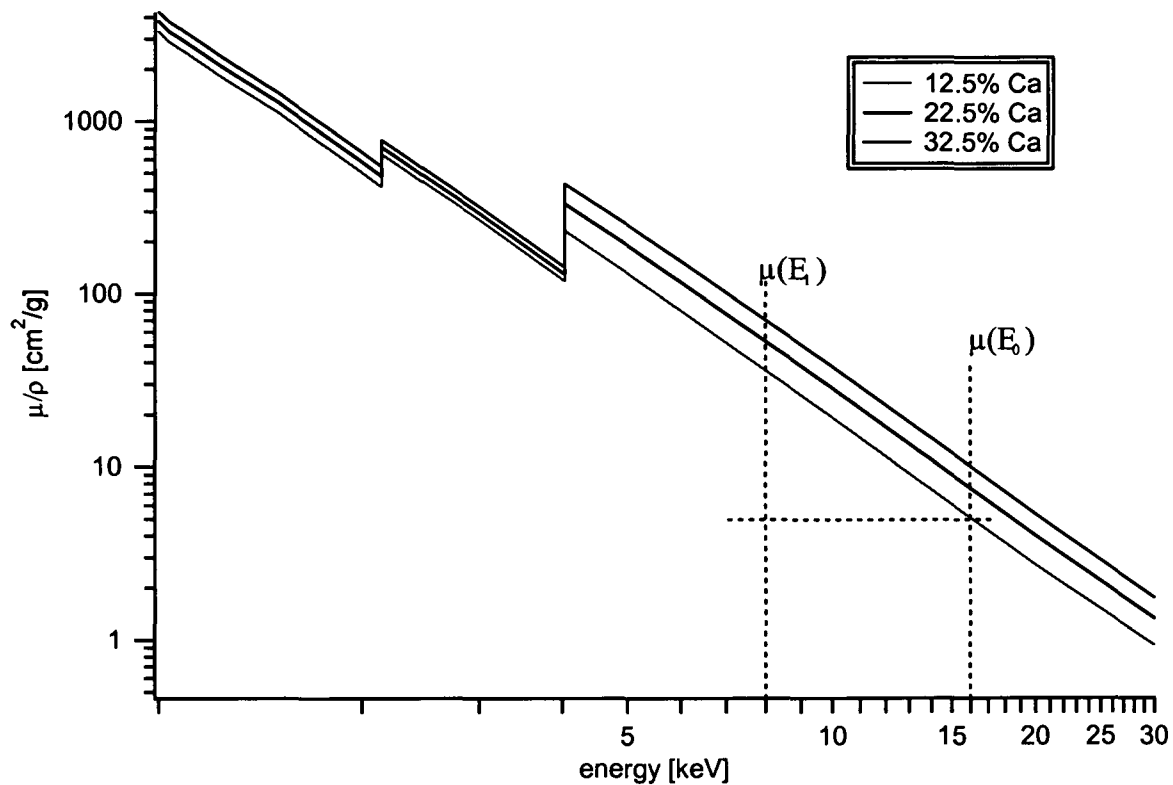


Figure 7.36: Absorption coefficient calculated for the standard reference material cortical bone for different concentrations of Ca

Implementing the absorption correction described above in the reconstruction algorithm a (to some extent) corrected fluorescence image of the sample is obtained (Figure 7.37). As a result an improved image can be generated for Ca, exhibiting more details on the distribution in a broader zone at the sample edge compared to the uncorrected image. Whereas for the innermost part of the sample, from where no fluorescence photons are detected, no improvements could be reached. In case of Zn and Pb the absorption correction led to no difference in the distribution maps, showing that for these elements conclusions on the distribution can be drawn also without correction.

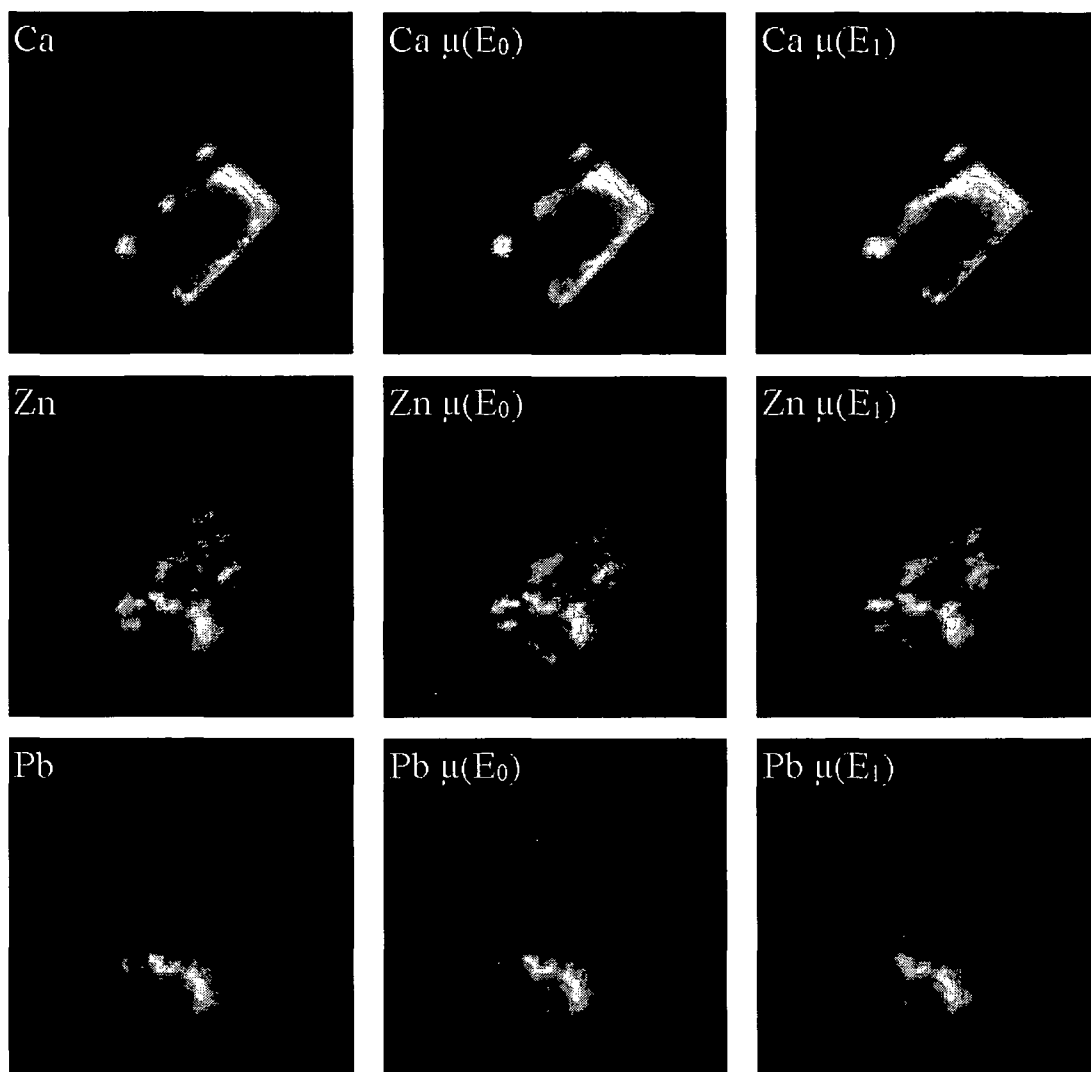


Figure 7.37: Comparison of uncorrected and corrected distributions for various elements. The uncorrected results, the results corrected without and with energy scaling are shown from left to right.

7.6.3 Conclusions

The spectrometer, designed by IAEA Seibersdorf Laboratories, XRF Group, Instrumentation Unit, for combined absorption- and fluorescence tomography was successfully installed at the Fluo-Topo beamline at ANKA, Karlsruhe, Germany, and it could be shown that fluorescence tomography is well suited to determine the (trace) element distribution in human bone. Although, due to the lack of data from other imaging techniques (BEI), the accumulation of Zn and Pb could not be clearly assigned to the tidemark of the bone it could be shown that highest intensities for these elements are restricted to small zones. The application of the simplified absorption correction revealed an improved image for Ca and showed that no correction is necessary to make conclusions on the Zn and Pb distribution in the bone matrix.

The used algorithm has the advantage that it can be directly applied to the measured sinograms before reconstruction. Since it deals with a very special case (sample with no holes, almost equal distribution of the main absorbing elements) a more general approach as used by Golosio et.al. [66] might reveal better results.

8 Elemental distribution in human brain

Based on the fact that Pb showed a very inhomogeneous distribution in calcified tissue one could assume, that it is also not uniformly distributed in noncalcified tissue. To check this assumption SR μ -XRF measurements have been carried out on thin slices of various areas of human brain.

8.1 Introduction

Cognitive deficits are repeatedly described with exposure to Pb. Studies showed that Pb exposed subjects tested to assess concentration, motor skills, memory and mood performed significantly worse than controls [92]. Especially in infants and young children even low ($\sim 7\mu\text{g}/\text{dl}$) blood lead levels lead to impaired performance on tests of spatial working memory, spatial memory span and might reduce the I.Q. [93]. However, it is not known which regions of the human brain are mostly effected by Pb. Therefore first attempts were made to study whether there are brain areas accumulating more or less Pb than others.

8.2 Experimental setup

Measurements have been carried out at ID-22, ESRF, Grenoble, France. At this beamline (Figure 8.1), dedicated to Micro-Fluorescence, Imaging and Diffraction (μ -FID), a monochromatic beam from an undulator station, focused by Kirkpatrick-Baez X-ray optics is provided. Energy to excite Pb-L lines efficiently was set to 16 keV which additionally led to sufficient low background signals in the energy region of the Pb-L α line ($E = 10.5$ keV). The beam size achieved by Kirkpatrick-Baez focussing was $5\ \mu\text{m} \times 3.3\ \mu\text{m}$ (horizontal x vertical). For beam monitoring the incident beam a pinhole ionisation chamber is mounted directly after the X-ray optics, allowing to normalize the recorded fluorescence photons to the incoming flux. In order to make optimal use of the polarization of the synchrotron beam a Si(Li) semiconductor detector was placed perpendicular to the primary beam in the orbital plane of the storage ring. Angles between incident beam –specimen-detector was chosen to be 45° each. The sample was mounted on a motor driven 3-axial sample stage for automatic area scanning of the sample. The actual sample position was optically controlled by a videozoom microscope.

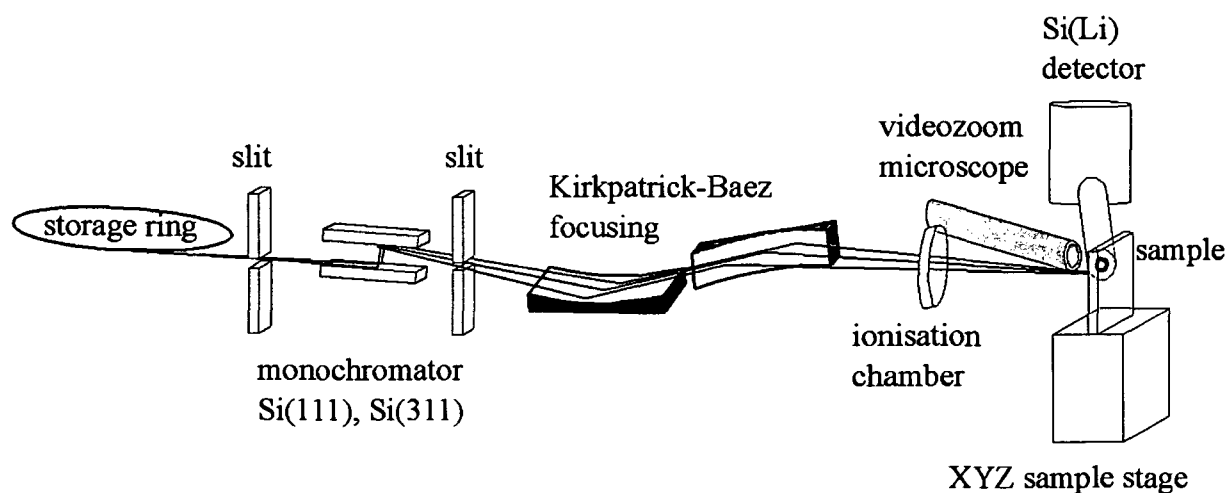


Figure 8.1: Experimental setup at ID-22 (μ -FID), ESRF, Grenoble, France

All recorded spectra have been automatically fitted with QXAS-AXIL, elemental maps were generated using the Sigma Plot software.

8.3 Samples / sample preparation

Brain slices from frontal cortex, thalamus and hippocampus (see Figure 8.2) have been prepared for analysis at the AKH, Vienna, Austria. By microtome cutting slices (20 μ m thickness) were produced from paraffin embedded brain tissue. All samples were mounted on capton foils, on slide frames.

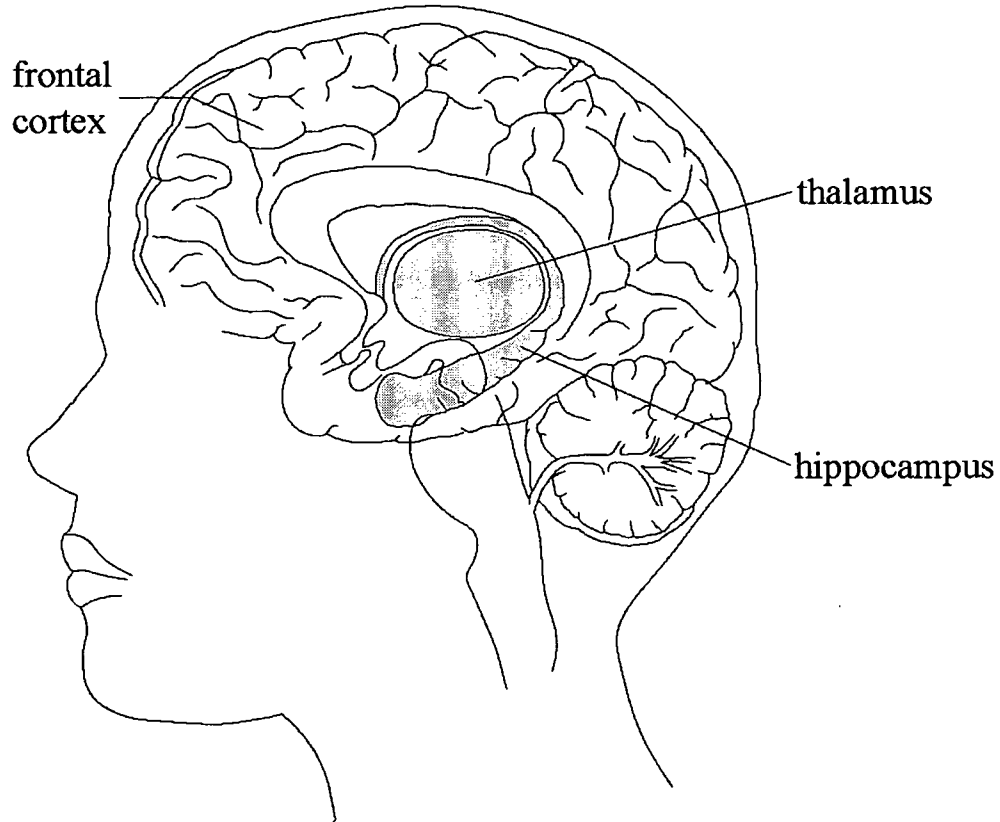


Figure 8.2: Illustration of human brain. Samples from frontal cortex, thalamus and hippocampus have been prepared for μ -XRF.

8.4 Results

Results of a fluorescence scan in plexus choroidea (in the thalamus region), a meshwork of vessels where the liquor cerebrospinalis (cerebrospinal fluid) is generated are shown in Figure 8.3. A strong correlation between the distribution of S, Ca, Fe, Cu, Zn and Br can be seen. However Pb can only be found at singular points of this meshwork. Moreover some Pb hot-spots, do not correlate with the structure and need further investigations of this structure in comparison with histological slices of 1 μm thickness from this areas. The overall investigated area was 390 x 600 μm^2 with step widths of 13 μm horizontal and 20 μm vertical. Measuring time per pixel was set to 5s.

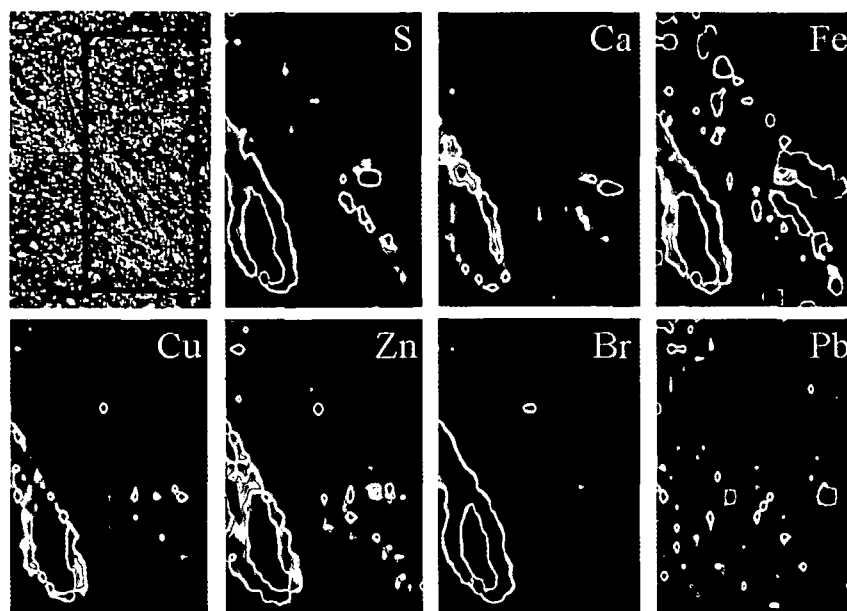


Figure 8.3: Area scan in plexus choroidea. The microscope image (top left) and the element maps of S, Ca, Fe, Cu, Zn, Br, and Pb are displayed. Scan parameters: 31 x 31 pixels, Step widths: $d_{\text{hor}} = 13\mu\text{m}$, $d_{\text{ver}} = 20\mu\text{m}$, measuring time: 5s/pixel

Figure 8.4 shows the microscope image (left side) and the element maps of an investigated area in hippocampus. The detection of highest Fe intensities on the inside of the structure as well as the shape of structure show that the scanned region was a blood vessel. Again and in comparison with Figure 8.3 S, Cu and Br (with three hot spots) seem to correlate with the vessel wall. Again isolated points of increased Pb intensities were found partially at the vessel wall but also within surrounding brain tissue. Up till now it is not clear whether they represent artefacts introduced by sample preparation or special regions of Pb enrichment. Small step size scans (Figure 8.5) across one of these hot spots revealed a correlation of Pb with Ca, Fe, Cu and Zn. From this scan one can roughly estimate the size of the hot spot, which is about 10-20 μm .

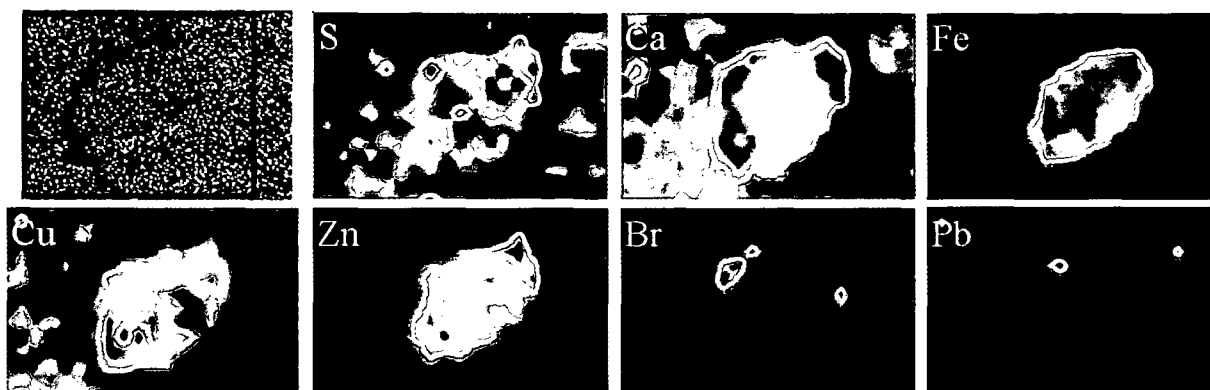


Figure 8.4: Scan across a blood vessel in the hippocampus region: The microscope image (top left) and the element maps of S, Ca, Fe, Cu, Zn, Br, and Pb are displayed. Scan parameters: 21 x 14 pixels, step widths: $d_{\text{hor}} = 20\mu\text{m}$, $d_{\text{ver}} = 20\mu\text{m}$, measuring time: 5s/pixel

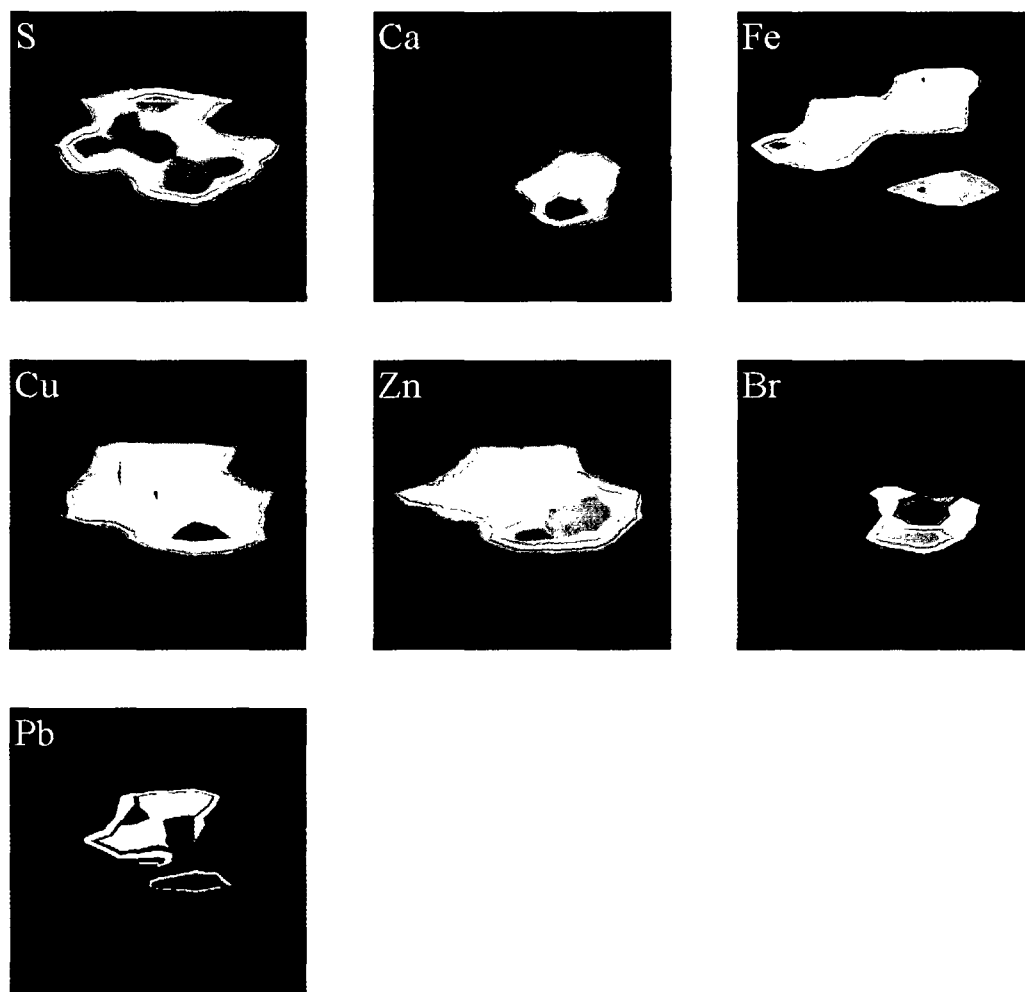


Figure 8.5: Scan across a Pb hot spot. The element maps of S, Ca, Fe, Cu, Zn, Br, and Pb are displayed. Scan parameters: 9 x 14 pixels $40 \times 39 \mu\text{m}^2$, step widths: $d_{\text{hor}} = 5\mu\text{m}$, $d_{\text{ver}} = 3\mu\text{m}$, measuring time: 10s/pixel

The fluorescence spectrum at the point of maximal Pb intensities in the detailed scan (Figure 8.5) is displayed in Figure 8.6, indicating the excellent spectral conditions at ESRF.

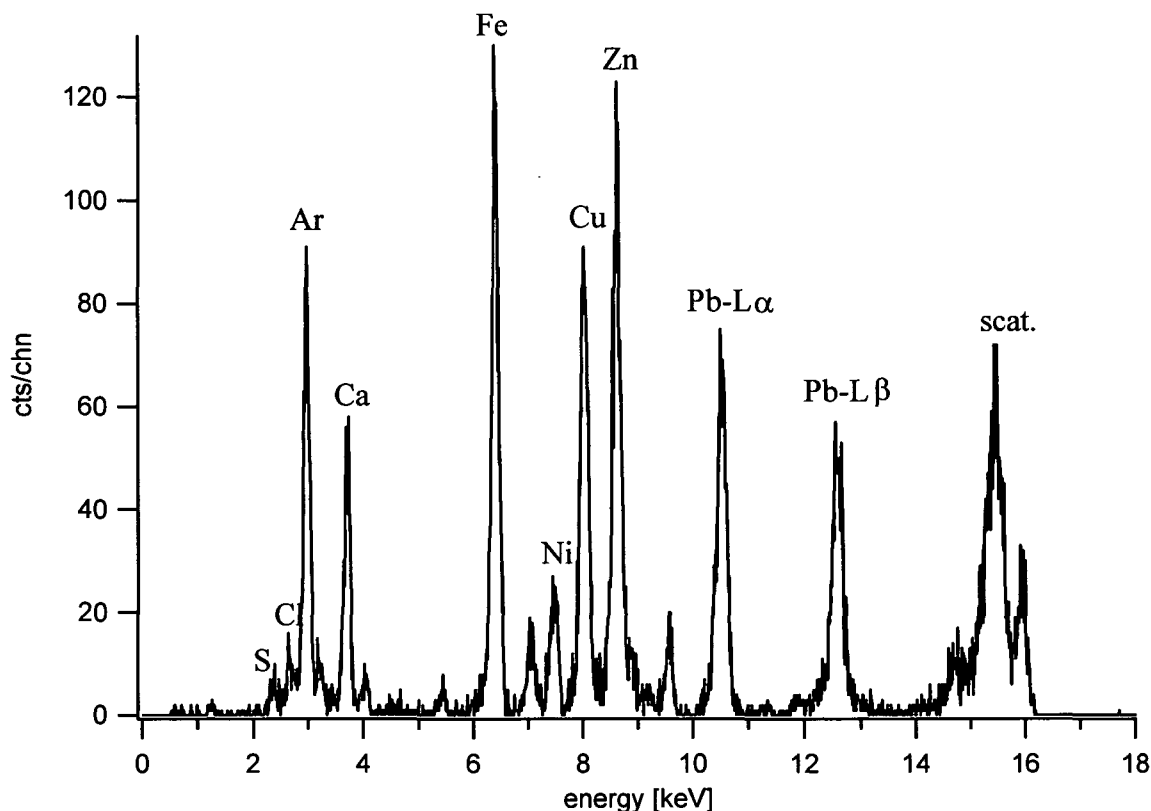


Figure 8.6: Fluorescence spectrum at maximal Pb intensities from a scan in human brain tissue. Spectrum obtained in 10s.

8.5 Conclusions

Pb could be detected in all investigated brain areas: frontal cortex, thalamus and hippocampus. In each of the brain regions Pb was inhomogeneously distributed. Moreover singular hot spots correlated individually with various elements. Up until now it is not cleared whether inhomogeneities in the Pb distribution are due to preparation and slicing technique, or represent Pb enrichment in these areas.

9 Concluding remarks

Synchrotron micro XRF in various modes has been exploited to study the elemental distribution in human bones and brain. Among the variety of the elements present in the tissue samples special interest was put on the determination of Pb, which is, due to its toxicity of great medical importance. Making use of the outstanding features of monochromatic synchrotron radiation it was possible to obtain results at the different synchrotron radiation facilities, HASYLAB, Hamburg, ANKA, Karlsruhe, ESRF, Grenoble, within reasonable measuring time.

In a first measurement series, carried out at HASYLAB, beamline L in collaboration with the Unversitätsklinik für Innere Medizin IV, Abteilung Arbeitsmedizin, AKH-Wien 4mm thick samples have been analyzed. Increased Pb intensities were found in cortical bone, but due to the irregular shape of the samples it was impossible to conclude whether this was due to geometric effects or due to Pb enrichment in this area.

The preparation of 200 μ m thick bone slices, done by the group from the Ludwig Boltzmann-Institute of Osteology, Hanusch-Krankenhaus der WGKK und Unfallkrankenhaus Meidling der AUVA, led to a significant reduction in the geometric effects and facilitated the analysis and interpretation of the results. Comparing the results from several XRF line scans on bone slices from different individuals with backscattered electron images (BEI) it could be shown, that Pb and Zn are inhomogeneously distributed even within the region of cortical bone showing highest fluorescence intensities in calcified cartilage. Since the samples were randomly chosen from a number of bones with no evidence of metabolic bone diseases in the medical record this finding indicated a general phenomenon of Pb and Zn accumulation inter- and intra-individually.

Performing high resolution μ -XRF measurements in the confocal geometry it was possible to reach a further reduction of the remaining geometric effects due to the sample thickness and to obtain precise elemental maps of the constituents of the sample. As a result it was possible to assign the distribution of the various elements to the structural features of the bone slices as seen from BEI. The zones of high accumulation of Zn and Pb could be restricted to the tidemark, and to cement lines between bone packets of different age. While Zn accumulates more or less equal at all border lines, intensities of Pb were about 10 times higher at the tidemark compared to cement lines.

In order to obtain better statistics and therefore medical relevant data future investigations of a large set of samples are suggested based on the developed technique of confocal μ -XRF on calcified tissue. Bones from subjects, exposed or non-exposed to Pb, should be analyzed with respect to their medical record. From such measurements possible links between Pb and bone- or cartilage diseases could be established. Since such series of measurements, where a large number of bone slices has to be analyzed are relatively time consuming they can not be performed at synchrotron facilities, where beamtime is very limited. Therefore laboratory μ -XRF systems have to be developed capable of measuring the distribution of the elements (especially Pb) in calcified biological matrix by automated scanning. As seen from the spectra presented in this thesis and under the knowledge that Pb is on the trace element level in human bone this can only be accomplished by special optics producing a monochromatic, focused X-ray beam. First experiments, using a double curved crystal optics attached to a low power tube, have already been performed in cooperation with X-Ray Optical Systems; Albany, New York, where it was possible to obtain elemental maps of Pb from a slice of femoral head.

Since cartilage (including the tidemark) and subchondral bone (with the cement lines) differ in their chemical composition the next step would be to determine the chemical speciation of Pb in the two different compartments of articular bones. Due to the high amount of S present in the cartilage one would expect lead sulfur compounds in the tidemark, whereas it is believed that in subchondral bone Pb is bound to carbonated hydroxyapatite (a calcium phosphate). To gain insight on the chemical speciation of Pb in the different calcified tissue XANES (X-ray absorption near edge structure) experiments on spots of high Pb content in subchondral bone as well as in calcified cartilage should be performed. These absorption spectroscopy experiments (XANES), where the energy of the primary beam is incrementally (eV steps) changed over the energy of the absorption edge of Pb, can be performed at the micro-focus end-station at HASYLAB beamline L without sample changing. Therefore a future experiments will be to obtain first an X-ray image of the sample followed by XANES measurements on selected points of the sample.

Similar results have been found performing combined X-ray absorption and fluorescence tomography measurements on bone samples. The experiments have been carried out in cooperation with the group from IAEA Seibersdorf Laboratories, XRF Group, Instrumentation Unit at the Fluo-Topo beamline at ANKA, Karlsruhe, Germany. With the application of this special technique the results from confocal μ -XRF could be proofed.

Elemental mapping has been performed on various slices from different areas of human brain at ESRF, ID-22. Whereas the assignment of the maps to different structures of the brain is much more difficult than it is for bone tissue, an inhomogeneous distribution of Pb was found in all analyzed samples from frontal cortex, hippocampus and thalamus.

The combination of synchrotron radiation with the excellent performance of the applied X-ray optics as well as the application of novel X-ray imaging techniques, such as confocal micro XRF and combined fluorescence and absorption tomography, allowed to study the elemental distribution in organic matrices with the highest possible spatial resolution.

Bibliography

- [1] Adler I., Axelrod J., Branco J.J.R., *Adv. X-Ray Anal.* **5**, 2 (1962)
- [2] Rose H.J., Christian R.P., Lindsay J.R., Larson R.R., *Geol. Surv. Proj. Pap. (US)* **650-B**, 8128 (1969)
- [3] Rindby A., *Nucl. Instr. Meth. A* **249**, 536 (1986)
- [4] Carpenter D.A., Taylor M.A., Holcombe C.E., *Adv. X-Ray Anal.* **32**, 115 (1989)
- [5] Attaelmanan A., Larsson S., Rindby A., Voglis P., Kucsumov S., *Rev. Sci. Instrum.* **65**, 7 (1994)
- [6] Hosokawa Y., Ozawa S., Nakazawa H., Nakayama T., *X-Ray Spectrom.* **26**, 380 (1997)
- [7] Vekemans B., Janssens K., Vittiglio G., Adams F., Andong L., Yiming Y., *Adv. X-Ray Anal.* **41**, 278 (1998)
- [8] Kumakhov M.A., *Adv. X-Ray Anal.* **43**, 214 (1998)
- [9] Ding X., He J., Wei F., Xie J., Wong P., Li Y., Chen B., Chen J., Yan Y., *Adv. X-Ray Anal.* **41**, 243 (1996)
- [10] Gao N., Ponomarev I., Xiao Q.F., Gibson W.M., Carpenter D.A., *Appl. Phys. Lett.* **71**(21), 3441 (1998)
- [11] Janssens K., Vincze L., Vekemens B., Adams F., Haller M., Knöchel A., *J. Anal. Atom. Spectrom.* **13**, 339 (1998)
- [12] Gatti E., Rehak P., *Nucl. Instr. Meth. Phys. Res.* **225**, 608 (1984)
- [13] IAEA Laboratories, Seibersdorf (Austria), QXAS, version 3.5 edition, 1996
- [14] Pepponi G., *doctoral thesis*, Vienna University of Technology, 2002
- [15] Kirkpatrick P., Baez A.V., *J. Opt. Soc. Am.* **38**, 766 (1948)
- [16] Nozaki H., Nakazawa Y., *J. Appl. Cryst.* **19**, 453 (1986)
- [17] Carpenter D., Haney L., Lawson R., *J. Trace Microprobe Techn.* **13**(2), 141 (1987)
- [18] Yamamoto N., Hosokawa H., *Jap. J. Appl. Phys.* **27**(11), 2203 (1988)
- [19] Kumakhov M.A., Komarov F.F., *Phys. Rev.* **191**(5), 289 (1990)
- [20] Engström P., Larsson S., *Adv. X-Ray Anal.* **35**, 1019 (1992)
- [21] Hoffman D., Bilderback D., Thiel D., *Nucl. Instr. Meth. A* **347**, 384 (1994)
- [22] Snigirev A., Kohn V., Snigireva I., Lengeler B., *Nature* **384**, 49 (1996)
- [23] Snigirev A., Filseth B., Elleaume P., Klocke Th., Kohn V., Lengeler B., Snigireva I., Souvorov A., Tummler J., *SPIE Proc.* **3151**, 164 (1997)

- [24] Lengeler B., Tummler J., Snigirev A., Snigireva I., Raven C., *J. Appl. Phys.* **84**,5855 (1998)
- [25] Baron A.Q.R., Kohmura Y., Krishnamurty V.V., Shvydko Yu.V., Ishikawa T., *J. Synchr. Rad.* **6**, 953 (1999)
- [26] Schroer C.G., Lengeler B., Benner B., Kuhlmann M., Gunzler T.F., Tummler J., Rau C., Weitkamp T., Snigirev A., Snigireva I., *SPIE Proc.* **4145**, 274 (2001)
- [27] Aristov V., Grigoriev M., Kuznetsov S., Shabelnikov L., Yunkin V., Weitkamp T., Rau C., Snigireva I., Snigirev A., Hoffmann M., Voges E., *Appl. Phys. Lett.* **77**,4058 (2000)
- [28] Aristov V., Grigoriev M.V., Kuznetsov S.M., Shabelnikov L.G., Yunkin V.A., Hoffmann M., Voges E., *Opt. Commun.* **177**,33 (2000)
- [29] Aristov V., Grigoriev M., Kuznetsov S., Shabelnikov L., Yunkin V., Rau C., Snigirev A., Snigireva I., Weitkamp T., Hoffmann M., Voges E., *SPIE Proc.* **4145**,285 (2001)
- [30] Baron A.Q.R., Kohmura Y., Ohishi Y., Ishikawa T., *Appl. Phys. Lett.* **74**,1492 (1999)
- [31] Cremer J.T., Piestrup M.A., Beguiristain H.R., Gary C.K., Pantell R.H., Tatchyan R.H., *Rev. Sci. Instr.* **70**, 3545 (1999)
- [32] Piestrup M.A., Cremer J.T., Beguiristain H.R., Gary C.K., Pantell R.H., *Rev. Sci. Instr.* **71**, 4375 (2000)
- [33] Beguiristain H.R., Cremer J.T., Piestrup M.A., Pantell R.H., Gary C.K., Feinstein J., *SPIE Proc.* **4144**, 155 (2000)
- [34] Piestrup M.A., Beguiristain H.R., Gary C.K., Clemer J.T., Pantell R.H., Tatchyn R., *Nucl. Instr. Meth. B* **173**, 170 (2001)
- [35] Ohishi Y., Baron A.Q.R., Ishii M., Ishikawa T., Shimomura O., *Nucl. Instr. Meth. A* **467–468**, 962 (2001)
- [36] Nazmov V., Shabel'nikov L., Pantenburg F.J., Mohr J., Reznikova E., Snigirev A., Snigireva I., Kouznetsov S., DiMichiel M., *Nucl. Instr. Meth. B* **217**, 409 (2004)
- [37] Van Grieken R., Markowicz A., Eds., *Handbook of X-Ray Spectrometry*, Marcel Dekker Inc. 2002
- [38] Janssens K., Adams F., Rindby A., Eds., *Microscopic X-ray Fluorescence Analysis*, John Wiley & Sons Ltd. 2000
- [39] Sherman J., *Spectrochim. Acta* **7**, 283 (1955)
- [40] Sparks J.R., *Adv. X-Ray Anal.* **19**, 19 (1975)
- [41] Mantler M., *Adv. X-Ray Anal.* **30**, 97 (1987)

- [42] Mantler M., *Adv. X-Ray Anal.* **37**, 13 (1994)
- [43] Lankosz M., Pella P.A., *X-Ray Spectrom.* **26**, 347 (1997)
- [44] He T., Gardner R.P., Verghese K., *Adv. X-ray Anal.* **35B**, 727 (1992)
- [45] Vincze L., Janssens K., Adams F., *Spectrochim. Acta Part B* **48** 553 (1993)
- [46] Vincze L., Janssens K., Adams F., Jones K.W., *Spectrochim. Acta Part B* **50** ,1481 (1995)
- [47] Vincze L., Janssens K., Adams F., *Spectrochim. Acta Part B* **50**, 127 (1995)
- [48] Sanchez H., Satori R., *X-ray Spectrom.* **23**, 141 (1994)
- [49] Fernandez J.E., *X-ray Spectrom.* **21**,57 (1992)
- [50] Mantler M., *Adv. X-ray Anal.* **43**, 753 (1999)
- [51] Lankosz M., *X-ray Spectrom.* **21**, 11 (1992)
- [52] Lankosz M., *X-ray Spectrom.* **22**, 125 (1993) -131
- [53] Somogyi A., *Spectrochim. Acta Part B* **55**,75 (2000)
- [54] Kumakhov M.A., *X-Ray Spectrom.* **29**, 343 (2000)
- [55] Ding X., Gao N., Havrilla G., *SPIE Proc.* **4144**, 174 (2000)
- [56] Fiorini C., Longoni A., Bjeomikhov A., *IEEE Trans. Nucl. Sci.* **48**(3) 268 (2001)
- [57] Kanngießler B., Malzer W., Rodriguez A.F., Reiche I., *Spectrochim. Acta Part B* **60**, 41 (2005)
- [58] Proost K., Janssens K., Vincze L., Falkenberg G., Gao N., Bly P., HASYLAB Annual report 2002
http://www-hasylib.desy.de/science/annual_reports/2002_report/part1/contrib/49/7864.pdf
- [59] Kanngießler B., Malzer W., Reiche I., *Nucl. Instr. Meth. B* **211**, 259 (2003)
- [60] Smit Z., Janssens K., Proost K., Langus I., *Nucl. Instr. Meth. B* **219-220**, 35 (2004)
- [61] Vincze L., Vekemans B., Brenker F.E., Falkenberg G., Rickers K., Somogyi A., Kersten M., Adams F., *Anal. Chem.* **76**, 6786 (2004)
- [62] Worley C.G., Colletti L.P., Havrilla G.J., *Abstr. Pap.-Am. Chem. Soc.* **23** (2002) 042-NUCL Part2
- [63] Janssens K., Proost K., Falkenberg G., *Spectrochim. Acta Part B* **59**, 1637 (2004)
- [64] Kak A.C., Slaney M., *Principles of Computerized Tomographic Imaging*, IEEE Inc. (1999)
- [65] Gurker N., *Computerunterstützte Abbildungsverfahren*, Unterlagen zur Lehrveranstaltung, Vienna University of Technology (2003)
- [66] Golosio B., Simionovici A., Somogyi A., Lemelle L., Chukalina M., Brunetti A., *J. Appl. Phys.* **94**(1), 145 (2003)

- [67] *Handbook of Synchrotron Radiation Vol. 1-4*, North Holland 1991
- [68] Schwinger J., *Phys. Rev.* **70**, 798 (1946)
- [69] Schwinger J., *Phys. Rev.* **75**, 1912 (1949)
- [70] Balewski K., Brefeld W., Hahn U., Pflüger J., Rossmann R., An Undulator at PETRA II – a New Synchrotron Source at DESY, in *Proceedings of IEEE PAC '95*, p. 275, Dallas, Texas, 1995
- [71] *Toxicological Profile for Lead*, U.S. DEPARTMENT OF HEALTH AND HUMAN SERVICES, Public Health Service, Agency for Toxic Substances and Disease Registry, (1999)
- [72] Skerving S., Ahlgren L., Christofferson J.O., Hager-Aronsen B., Mattson S., Schütz A., *Arh. Hig. Toksikol.* **34**, 341 (1983).
- [73] Schütz A., Skerfving S., Ahlgren L., Ranstam J., Christofferson J.O., *Scand. J. Work Environ. Health* **13**, 221 (1987).
- [74] Todd A.C., Chettle D.R., *Environ. Health Persp.* **102** 172 (1994)
- [75] Gulson B.L., Jameson C.W., Mahaffey K.R., *J. Lab. Clin. Med.* **130**(1), 51 (1997)
- [76] Osterode W., Reining G., Männer G., Jäger J., Vierhapper H., *Thyroid.* **10**, 161 (2000)
- [77] Osterode W., Zettinig G., Potzi C., Männer G., *J. Toxicol. Environ. Health A* **65**, 649 (2002)
- [78] http://training.seer.cancer.gov/module_anatomy/unit3_4_bone_classification.html
- [79] Fratzl P., Gupta H. S., Paschalis E. P., Roschger P., *J. Mater. Chem.* **14**, 2115 (2004)
- [80] <http://www.bu.edu/histology/p/0310200a.htm>
- [81] Falkenberg G., Clauss O., Tschentscher T., HASYLAB Annual report 2001, http://www-hasyllab.desy.de/science/annual_reports/2001_report/part1/intern/5720.pdf
- [82] Falkenberg G., Rickers K., HASYLAB Annual Report 2002, http://www-hasyllab.desy.de/science/annualreports/2002_report/part1/intern/8522.pdf
- [83] Schidlovsky G., Jones K.W., Burger D.E., Milder F.L., Hu H., *Adv. In Vivo Body Comp.* 275 (1990)
- [84] Lindh U., Brune D., Nordberg G., *Sci. Total Environ.*; **10**, 31 (1978)
- [85] Jones K.W., Schidlovsky G., Burger D.E., Milder F.L., Hu H., *Adv. In Vivo Body Comp.* 281(1990)
- [86] ICRU *Report 44 of the International Commission on Radiation Units and Measurements*. ICRU: Bethesda, MD, (1989).
- [87] Zizak I., Roschger P., Paris O., Misof B.M., Berzlanovich A., Bernstorff S., Amenitsch H., Klaushofer K., Fratzl P., *J. Struct. Biol.* **141**, 208 (2003)

- [88] Gupta H.S., Schratte S., Tesch W., Roschger P., Berzlanovich A., Schoeberl T., Klaushofer K., Fratzl P., *J. Struct. Biol.* 149(2),138 (2005)
- [89] Wegrzynek D., Markowicz A., Bamford S., China-Cano E., Bogovac M., *Nucl. Instr. Meth. B*, **231**, 176 (2005)
- [90] Data Acquisition for X-ray Microprobe, *Computer Manual Series No. 17*, IAEA, Vienna, 2002
- [91] Wegrzynek D., *Private Communication*
- [92] Fiedler N., Weisel C., Lynch R., Kelly-McNeil K., Wedeen R., Jones K., Udasin I., Ohman-Strickland P., Gochfeld M., *Am. J. Ind. Med.*, **44**(4), 413 (2003)
- [93] Canfield R.L., Gendle M.H., Cory-Slechta D.A., *Dev. Neuropsychol.* **26**(1), 513 (2004)

Curriculum Vitae

Personal details

Name	Norbert Zöger
Place of birth	Wiener Neustadt, Austria
Date of birth	16.09.1974
Address	Josef Bierenzgasse 8/49, 2700 Wiener Neustadt

Education

1980-1984	Primary school in Wiener Neustadt, Austria
1984-1992	Bundesrealgymnasium in Wiener Neustadt, Austria
1992-2001	Physics studies at the „Technische Universität Wien“ Diploma Thesis: „Orts- und Winkel aufgelöste Totalreflexionsröntgenfluoreszenzanalyse an Si-wafer Oberflächen“

Publications (refereed)

G. Pepponi, P. Wobrauschek, C. Strel, N. Zoeger, F. Hegedüs
Synchrotron radiation induced TXRF of reactor steel samples
X-ray Spectrometry 30 (4), 267-272, special issue Proceedings of EDXRS, Krakow 2000

G. Pepponi, P. Wobrauschek, F. Hegedüs, C. Strel, N. Zöger, C. Jokubonis, G. Falkenberg
*SR-TXRF and EDXRS on AP1 films applied to the analysis of trace elements in metal alloys
for the construction of nuclear reactor core components : a comparison*
Spectrochim. Acta 56B, 2063-2071 (2001) special issue of TXRF 2000 conference, Vienna

C. Strel, G. Pepponi, P. Wobrauschek, N. Zoeger, P. Pianetta, K. Baur, S. Pahlke, L. Fabry,
C. Mantler, B. Kanngiesser, W. Malzer
*Analysis of low Z elements on Si wafer surfaces with synchrotron radiation induced TXRF at
SSRL, Beamline 3-3: comparison of droplets with spin coated wafers*
Spectrochim. Acta 58B, 2105-2112 (2003)

C. Strelì, P. Wobrauschek, G. Pepponi, N. Zoeger
A new TXRF vacuum chamber with sample changer for chemical analysis
Spectrochimica Acta B 59, 1199- 1203 (2004), special issue of the TXRF conference 2003 in Osaka

G. Pepponi, C. Strelì, P. Wobrauschek, N. Zoeger, K. Luening, P. Pianetta, D. Giubertoni, M. Barozzi, M. Bersani
Non-destructive dose determination and depth profiling of As Ultra shallow junctions with TXRF compared to dynamic SIMS
Spectrochimica Acta B 59, 1243-1249 (2004), special issue of the TXRF conference 2003 in Osaka

N. Zoeger, P. Wobrauschek, C. Strelì, G. Pepponi, P. Roschger, G. Falkenberg, W. Osterode
Distribution of Pb and Zn in slices of human bone by SR- μ XRF
X-ray spectrometry, 34,140-143 (2005)

N. Zoeger, C. Strelì, P. Wobrauschek, C. Jokubonis, G. Pepponi, P. Roschger, S. Bohic, W. Osterode
Elemental mapping in slices of human brain by SR- μ XRF
Adv. In X-ray Anal., accepted

N. Zoeger, C. Strelì, P. Wobrauschek, C. Jokubonis, G. Pepponi, P. Roschger, S. Bohic, W. Osterode
Elemental mapping in slices of human brain by SR- μ XRF
Powder Diffr. 20, 2 (2005)

P. Wobrauschek, B. Frank, N. Zoeger, C. Strelì, N. Cernohlawek, C. Jokubonis, H. Hoefler,
Micro XRF of light elements using a polycapillary lens and a n UTW SDD detector inside a vacuum chamber
Adv. X-ray Anal. accepted

Publications (not refereed)

F. Hegedüs, P. Wobrauschek, C. Strelì, G. Pepponi, N. Zoeger
SR-TXRF trace element analysis of Nb and Rare Earth Elements in steel samples
Hasylab Annual Report 1999

G. Pepponi, C. Strelì, P. Wobrauschek, S. Zamini, N. Zoeger, G. Falkenberg
Comparison of SR-TXRF excitation- detection geometries
Hasylab Annual Report 2001

P. Wobrauschek, C. Strelì, G. Pepponi, S. Zamini, N. Zoeger, G. Falkenberg, W. Osterode
Micro-XRF investigation of human bone
Hasylab Annual Report 2001

C. Strelì, P. Wobrauschek, G. Pepponi, S. Zamini, N. Zoeger, G. Falkenberg
SR-TXRF ultra trace element analysis on Si-wafer surfaces with new multilayer monochromators at Beamline L
Hasylab Annual Report 2001

F. Hegedüs, P. Wobrauschek, C. Strel, G. Pepponi, S. Zamini, N. Zoeger, G. Falkenberg
Synchrotron radiation induced TXRF of reactor steel samples
Hasylab Annual Report 2001

P. Wobrauschek, N. Zoeger, G. Pepponi, C. Strel, G. Falkenberg, W. Osterode
Variations in Pb and Ca concentrations at bone transition zones determined by SR-XRF with a microbeam at BL L
Hasylab Annual Report 2002

P. Wobrauschek, N. Zoeger, C. Strel, G. Pepponi, C. Jokubonis, G. Falkenberg, P. Roschger, W. Osterode
Spatially resolved determination of Minor and Trace elements in 200µm thin slices of human bone by Micro SR-XRF at BL L
Hasylab Annual Report 2003

N. Zoeger, P. Wobrauschek, C. Strel, G. Falkenberg, P. Roschger,
Elemental Mapping of Human Bone by Confocal SR micro-XRF
Hasylab Annual Report 2004

N. Zoeger, C. Strel, P. Wobrauschek, D. Wegrzynek, E. Chinea-Cano, R. Simon, S. Staub
Combined fluorescence- absorption tomography on human bones
ANKA Annual Report 2004

D. Wegrzynek, E. Chinea-Cano, N. Zoeger, C. Strel, P. Wobrauschek, M. Eriksson, M. Betti, S. Török, R. Simon, S. Staub
Combined fluorescence- absorption tomography on U- and Pu-rich particles
ANKA Annual Report 2004

C. Strel, P. Wobrauschek, N. Zoeger, G. Pepponi
A new TXRF vacuum chamber with sample changer
XRF Newsletter 7, 2004

Oral presentations

N. Zoeger
Determination of Calcium and Lead Distribution in Human Bone by Synchrotron – Micro - XRF
13th European Students Conference, Charite, Berlin, Germany, 2002

N. Zoeger, P. Wobrauschek, C. Strel, G. Pepponi, G. Falkenberg, P. Roschger, W. Osterode
Synchrotron µ-XRF on Human Bone Slices- Determination of Trace Element Distribution
17th International Congress on X-ray Optics and Microanalysis, Chamonix, France, 2003

N. Zoeger, P. Wobrauschek, C. Strel, E. Chinea-Cano, D. Wegrzynek, P. Roschger, R. Simon, S. Staub, G. Falkenberg
3D Elemental Imaging in Human Bone by SR-µXRF
EXRS Conference, Alghero, Italy, 2004

N. Zoeger, P. Wobrauschek, C. Strel, E. Chinea-Cano, D. Wegrzynek, P. Roschger, R. Simon, S. Staub, G. Falkenberg
3D Synchrotron Micro RFA an Menschlichen Knochen
54. Jahrestagung der ÖPG, Linz, Austria, 2004

N. Zoeger, P. Wobrauschek, C. Strel
3D SR μ -XRF on Human Bone Samples
53rd Annual Denver X-ray Conference, Steamboat Springs, USA, 2004

N. Zoeger, P. Wobrauschek, C. Strel, G. Falkenberg, P. Roschger
Elemental Mapping of Human Bone by Confocal SR micro-XRF
HASYLAB User-meeting, Hamburg, Germany 2005